

University of St Andrews



Full metadata for this thesis is available in
St Andrews Research Repository
at:

<http://research-repository.st-andrews.ac.uk/>

This thesis is protected by original copyright

A HIGH PRESSURE NUCLEAR MAGNETIC
RESONANCE STUDY OF SODIUM TUNGSTEN
BRONZE Na_xWO_3

A Thesis
presented by
W. Ramage B.Sc.
to the
University of St Andrews
in application for the Degree of
Doctor of Philosophy



ABSTRACT

An investigation of the metal non-metal transition has been performed in cubic Sodium Tungsten Bronze, Na_xWO_3 , using the technique of pulsed Nuclear Magnetic Resonance. The Sodium resonance has been observed at low temperatures and at pressures up to 4 K Bar in a range of samples from Sodium concentrations $x = 0.22$, where the system is very close to the transition from a metal to an insulator, up to $x = 0.84$, where the system is a good metallic conductor. We have measured the Sodium spin-lattice relaxation rates at a 50 MHz frequency and at temperatures of 4.2 K and below. In addition, we have investigated the x dependence and the pressure dependence of the Sodium nuclear quadrupole coupling constant with a view to obtaining a model for the physical structure of Na_xWO_3 .

The relaxation rates and Knight shifts show that for $x \geq 0.35$, the conduction band consists of Tungsten 5d orbitals. Moreover, the density of states at the Fermi surface was found to be proportional to x , which agrees with the model of an exponential type of conduction band. For lower x values, there are enhancements in the Sodium relaxation rates which, as we have proposed, may arise from a Sodium type band being swept down into the conduction band. The exact nature of this band is not clear, but it does seem that the data can only be explained if about 50% Sodium 3d character is present at the Fermi surface. Our pressure results seem to indicate that this Sodium character may be caused by a reduction in screening as x decreases.

From the x dependence and pressure dependence of the quadrupole coupling constant, a model has been proposed for the structure of Na_xWO_3 involving displacements of the Oxygen atoms from their positions midway along the cube edges. The model assumes that both displacements and distortions of the Oxygen octahedra occur. This type of

ACKNOWLEDGEMENTS

The author wishes to express his sincere gratitude to Dr D.P. Tunstall for his patient guidance and encouragement throughout this research and for many stimulating discussions which greatly enhanced the author's understanding. He is also grateful to Professor D.F. Holcomb and Dr B.R. Weinberger at Cornell University for making available the samples, and for supplying the Tungsten data prior to publication. Thanks are due also to Dr D. Batchelder at Queen Mary College, London, and to Professor J.S. Dugdale at Leeds for many useful discussions on pressure techniques, and for the loan of some equipment which enabled the author to design the pressure cell. In this area, the author is also grateful to Mr R.H. Mitchell and Mr R. McCraw for help in designing and constructing the pressure system and the raising and lowering mechanism for the pressure cell. He is also grateful to Mr T. Marshall for his cooperation in supplying the copious quantities of liquid Helium and liquid Nitrogen which enabled the cryostat to be operated almost continuously for several months. Thanks are also due to Miss Linda McLean for the accurate typing of the manuscript. Finally the author would like to extend his thanks to Professor J.F. Allen and to the staff and research students of the department for the excellent facilities made available to him, and also for the friendship and good humour which made his research so enjoyable.

CAREER

I entered the University of St Andrews in October 1970 and studied Mathematics and Physics. I graduated in July 1974 with a first class honours degree in Physics. In October 1974, following the award of an SRC Research Studentship at the University of St Andrews, I was enrolled there as a research student reading for the degree of Ph.D. under the Resolution of the University Court, 1967, No.1.

DECLARATION

I hereby certify that this thesis has been composed by me, and is a record of work done by me, and has not previously been presented for a Higher Degree. The research was carried out in the Physical Sciences Laboratory of St Salvator's College, in the University of St Andrews, under the supervision of Dr D.P. Tunstall.

CERTIFICATE

I certify that William Ramage B.Sc. has spent nine terms research work in the laboratories of the School of Physical Sciences, University of St Andrews, under my direction, that he has fulfilled the conditions of the Resolution of the University Court, 1967, No.1, and that he is qualified to submit the accompanying thesis in application for the Degree of Doctor of Philosophy.

Research Supervisor

CONTENTS

		Page
Chapter 1	INTRODUCTION	1
Chapter 2	BASIC THEORY OF NMR	8
	2.1 Introduction	8
	2.2 Basic Theory of Nuclear Resonance	8
	2.3 The Nuclear Dipole Interaction	9
	2.4 The Electric Quadrupole Interaction	11
	2.5 The Nuclear-Electron Magnetic Interaction	14
	2.6 The Knight Shift	15
	2.7 Spin-Lattice Relaxation	17
	2.7.1 Magnetic Relaxation	17
	2.7.2 The Korringa Relation	19
	2.7.3 Other Relaxation Processes	20
	2.8 NMR Lineshapes	22
	2.8.1 Dipolar Broadening	22
	2.8.2 Quadrupolar Broadening	23
	2.8.3 The Exchange Interaction	24
	2.9 Pulsed NMR	25
Chapter 3	THE METAL NON-METAL TRANSITION	27
	3.1 Introduction	27
	3.2 The Mott Transition	27
	3.3 The Mott-Hubbard Model	28
	3.4 Disorder and Anderson Localisation	31
	3.5 The Different Conductivity Regions	32
	3.6 Percolation	35

		Page
Chapter 4	HIGH PRESSURES	36
	4.1 Introduction	36
	4.2 The Choice of Solid Helium as the Pressure Transmitter	36
	4.3 The Pressure Generating System	38
	4.4 The High Pressure NMR Cell	42
	4.5 Helium Solidification	46
	4.6 Safety Aspects	48
Chapter 5	REVIEW OF EXPERIMENTAL DATA ON THE BRONZES	51
	5.1 Introduction	51
	5.2 Crystal Structure	51
	5.3 The Conduction Band and Fermi surface	52
	5.4 Transport Data	54
	5.5 Electronic Specific Heat and Magnetic Susceptibility	55
	5.6 Thermal Properties	56
	5.7 Optical Properties	57
	5.8 Nuclear Magnetic Resonance Studies	58
	5.9 Other Bronzes and Related Compounds	66
	5.10 The Metal Non-metal Transition	68
Chapter 6	RESULTS	71
	6.1 Compressibility	71
	6.2 The Two Signals	71
	6.3 The Echo Width	73
	6.4 The Echo and FID T_2	74
	6.5 Pulsewidths	76
	6.6 Quadrupolar Echoes	77
	6.7 Spin-Lattice Relaxation Rates	78
	6.8 The Knight Shift	81
	6.9 Electrostatic Energies	83

		Page
Chapter 7	DISCUSSION	87
	7.1 Structural Properties derived from quadrupole spectra and linewidth data	87
	7.2 Spin-Lattice Relaxation and the Knight Shift	100
	7.2.1 The High x Region	100
	7.2.2 The Enhancement Region	103
	7.2.3 The $x = 0.22$ Sample	112
Chapter 8	CONCLUSION	118
Chapter 9	APPENDIX	126
	9.1 Samples	126
	9.2 NMR Apparatus	127
	9.2.1 50 MHz NMR Spectrometer	127
	9.2.2 The NMR Probe	128
	9.2.3 The Superconducting Solenoid	130
	9.2.4 Cryogenics	132
	9.3 Fourier Transform NMR	133
	9.3.1 The Fourier Transform	133
	9.3.2 Electronics	135
	9.4 Computer Requirements	138

TABLE OF FIGURES

FIG.		Preceding Page
2.1	Quadrupolar powder patterns	23
3.1	The Hubbard Bands	28
3.2	Potential wells for Anderson lattice	31
3.3	Extended and Localised Wavefunctions	31
3.4	Anderson localisation	31
4.1	Melting Curve of Helium	37
4.2	Pressure loss on cooling along isochores	37
4.3	The Pressure System	41
4.4	Harwood Intensifier	41
4.5	Modified Intensifier Top Seal	41
4.6	Stress-strain curve of cell	43
4.7	The High Pressure Cell	43
4.8	Helium Solidification table	48
4.9	Test of Helium Solidification	48
5.1	Structure of Na_xWO_3	51
5.2	Phase Diagram	51
5.3	Band Structure of NaWO_3	51
5.4	Fermi Surface	51
5.5	Resistivity	55
5.6	Temperature dependence of Resistivity	55
5.7	Hall data	55
5.8	Specific Heat	55
5.9	Magnetic Susceptibility	55
5.10	Transition Temperatures	57
5.11	Optical Absorption Spectra	57
5.12	Previous Intensity Data	62
5.13	Sodium T_1 data (Tunstall)	62

FIG.		Preceding Page
5.14	Tungsten T_1 data	65
5.15	Tungsten Knight shifts	65
5.16	Tungsten linewidths	65
5.17	Resistivity of alkali Tungsten bronzes	67
6.1	Intensity data	73
6.2	Echo width	73
6.3	Pressure dependence of echo width	73
6.4	Echo T_2	75
6.5	FID T_2	75
6.6	Decays after pulse	76
6.7	T_1 data	80
6.8	Correction to T_1 data	80
6.9	T_1 data table	80
6.10	Non exponentiality of T_1	80
6.11	Temperature dependence of T_1	80
6.12	Pressure dependence of T_1	80
6.13	Power Spectra	82
6.14	Knight Shifts	82
6.15	Korringa Products	82
6.16	Madelung Energies	85
7.1	Oxygen displacement models	92
7.2	Oxygen displacement models	92
7.3	Calculated field gradients	92
9.1	Table of Sample properties	126
9.2	NMR Spectrometer	130
9.3	NMR Probe	130
9.4	Paper Tapes	137
9.5	Punch Interface	137
9.6	Fourier Transform Computer Program	139

CHAPTER 1INTRODUCTION

The metal non-metal transition has been observed in a wide range of materials²⁴, and is manifested by a change from metallic to semi-conducting or insulating behaviour when some external agency such as pressure, temperature or composition is varied. One such system is non-stoichiometric Sodium meta-Tungstate, Na_xWO_3 , more commonly known as Sodium Tungsten Bronze, because of its resemblance to bronze at its most common composition. It belongs to the family of alkali Tungsten bronzes, MxWO_3 , where M is commonly Hydrogen, Lithium, Sodium and Potassium. For values of x between 0.2 and 0.9, Sodium Tungsten bronze has the cubic perovskite type structure, which entails Tungsten atoms at cube corners, Oxygens midway along the cube edges, and a fraction x of the body centred positions occupied by Sodium atoms. Conductivity measurements¹¹² show that for $x > 0.2$, the system is metallic, but with the conductivity decreasing as x decreases. At around $x = 0.2$, the system undergoes a transition to a semiconducting phase, but unfortunately this is accompanied by a structural transition. Hence although it is not possible to observe the transition itself in the same structural phase, we can observe the approach to it from the metallic side, so as to determine the mechanisms which may be driving the transition. In particular, we shall be interested in three basic proposals. Firstly, the random positioning of the Sodium atoms introduces enough disorder to localise the electrons by a mechanism first advanced by Anderson⁴². Secondly, Coulomb repulsion of a carrier by an electron already on a particular site may split the conduction band into two Hubbard bands^{29,30}, with conduction ceasing when these two bands cease to overlap. Finally, local fluctuations in potential could cause conduction to occur in metallic channels^{52,86}, resulting in a percolation type model in which the transition occurs

when these channels no longer stretch unbroken across the sample.

In this work, we have used the pulsed Nuclear Magnetic Resonance technique to study the Sodium resonance in Na_xWO_3 in the cubic phase at temperatures of 4.2K and below. Although the primary object of this study was to derive information about the transition, much has also been discovered about the structural properties as well. Indeed, NMR in Na_xWO_3 contains so many surprises that this work is the eighth NMR investigation of this system, and will probably not be the last. A similar investigation to ours, but on the Tungsten resonance has been carried out by Weinberger¹²⁸ at Cornell University. We have carried out our measurements on his samples, and hence have confidence in comparing our data with his. Moreover, we shall also try to consider as well, all the available transport, NMR, magnetic, thermal and optical data etc., so as to present a comprehensive picture of Na_xWO_3 . For the rest of this chapter, we shall discuss the particular aims of this work, and briefly detail the data which was available at its commencement.

The early NMR data¹²²⁻¹²⁵ was beset by problems of sample purity and homogeneity, much as had occurred in the transport data. However the work had established that for $x > 0.35$, the conduction band was derived from Tungsten 5d orbitals, which were occupied by electrons donated by the Sodium. For this reason, the Tungsten Knight shift was negative and large, and spin-lattice relaxation was efficient, whereas the Sodium Knight shift was negative and small, and relaxation was not so efficient. However the existence of paramagnetic contributions to the relaxation rates meant that the actual values of the shifts and relaxation rates were questioned. The Sodium resonance was later measured by Tunstall⁹⁵, with purer samples, and with a sample range down to $x = 0.22$ which enabled the approach to the transition to be studied for the first time. He found that at high x ,

the density of states at the Fermi surface derived from relaxation rates was proportional to x , but at low x , large enhancements were in evidence, accompanied by a reduction in the Knight shift. This was interpreted as being due to partial admixture of Sodium 3s character at the Fermi surface, caused by a 3s band being swept down into the conduction band by the decrease in lattice constant which accompanies a decrease in x . However the Sodium Knight shift data lacked accuracy, since they were very small, and problems were encountered as to a suitable reference. Hence in this work it was decided to remeasure the shifts at a higher magnetic field so as to improve the accuracy. For this, a superconducting solenoid capable of producing fields of reasonable homogeneity up to 5T was purchased.

The main aim of this work however, was to study the pressure dependence of the NMR data. The decrease in lattice constant as x decreases⁸⁷ makes it difficult to determine whether effects are due to the reduction in electron density, or the reduction in lattice constant. With the application of pressure, it should be possible to separate these two effects. It was calculated from the compressibility, that 4 KBar hydrostatic pressure should produce the same reduction in lattice constant as would have been achieved by a reduction of x by about 0.05. Since at low x , the samples are separated by about this value, 4 KBar should effectively span the gap between samples as far as the lattice constant is concerned. Hence a pressure generating system was constructed capable of achieving 7 KBar hydrostatic pressure, since it is desirable to test all the components at about $1\frac{1}{2}$ times their working pressure. The NMR sample was contained in a Be - Cu pressure cell, since this alloy is non-magnetic and hence will not degrade the homogeneity of the superconducting solenoid. Since the measurements were to be at low temperature, solid Helium was chosen as the pressure transmitting fluid. This involves

compression of Helium gas with the inherent danger from its large stored energy should the system fail. Hence consideration was given to safety aspects such as safe working procedures and the construction of barriers.

The first area of interest for the pressure work was the Sodium spin-lattice relaxation rate enhancement at low x . If the reduction in lattice constant with decreasing x was responsible for driving down a Sodium type band, then application of pressure should also cause enhancement over the rate at atmospheric pressure. If no such pressure dependence was found however, it might indicate that the enhancements were due to the reduction in x , rather than the reduction in lattice constant. For a similar reason, the pressure dependence of the Sodium Knight shift would also be of interest in this region.

The second area of interest is the pressure dependence of the NMR parameters of the samples close to the metal non-metal transition. As has been mentioned, this transition is accompanied by a structural transition. If the change in structure is caused by lattice contraction, then by applying pressure, we may be able to force the system into a different structure. However if the structural transition is caused by the electronic transition, then the behaviour of the system under pressure will be determined by the pressure dependence of the electronic properties. Hence the pressure dependences of the NMR data for the two lowest x samples may provide some information on the mechanisms responsible for the transitions.

The final area is the pressure dependence of the quadrupolar spectrum of the Sodium resonance. Fromhold and Narath¹²⁴ first discovered two separate types of Sodium site in Na_xWO_3 . One type is characterised by a free induction decay with a time constant of the same order as the dipolar time constant and arises from Sodium nuclei in a predominantly cubic environment. The second type is characterised

by a much faster decay, and indeed the signal may be refocused by a second pulse to form a spin Echo. This latter signal is assumed to arise from nuclei in a non-cubic environment, and is surprising in view of the fact that although Sodium has a nuclear spin of $3/2$, the Sodium nuclei sit in cubic positions in the crystal. There have been two basic proposals to explain these two types of site. Firstly, the random positioning of the Sodium nuclei means that any Sodium atom may be surrounded by nearest neighbour vacancies, which produce electric field gradients large enough to cause the Echo signal. The longer free induction decay would originate from nuclei with nearest neighbour Sodium sites completely filled or completely empty. As x decreases, the number of such nuclei should become very small if all Sodium nuclei are positioned randomly. However in order to explain the fact that measurements show that the number of those nuclei remains roughly constant with x , it has been assumed the clustering of the Sodium nuclei into local $x = 1$ regions occurs¹²⁴. This model has been criticised⁹⁴ in that if screening is considered, the field gradients produced by the vacancies are not large enough to give rise to the Echo signal. Instead a second model has been advanced^{94,95}, in which the field gradients are assumed to originate from slight displacements of the Oxygen atoms from their regular positions. There is evidence that this does occur in many compounds of similar structure⁸⁸, and even in other bronzes⁹¹. Such displacements may be sensitive to the lattice spacing, and hence the pressure dependence of the Echo width may indicate which of these two mechanisms is responsible for the Echo, and may also provide more information on the crystal structure.

In addition to the pressure work, there were some NMR measurements at atmospheric pressure which would profit from repetition. We have already mentioned the need for more accurate Knight shifts. The Sodium spin-lattice relaxation rates at high x had been measured by Tunstall⁹⁵,

but had relied somewhat on other samples to establish their x^2 dependence. We have added more samples in this region. The Echo width had not been measured accurately at low temperatures. This was mainly due to a lack of sufficient RF power to excite all the nuclei, or to difficulty in measuring the narrow Echoes. In this study, the larger magnetic field of 5T has meant that the quadrupolar broadening of the central line is smaller and hence all nuclei may be excited by moderate RF power, and it has also meant that the Echoes are wider and easier to measure. Finally the field dependence of NMR parameters close to the metal non-metal transition has on other systems yielded information on the nature of the transition. By comparing our high field measurements with the others at lower fields, we may determine whether such dependences exist in Na_xWO_3 .

Having briefly described the aims of this work, we shall end this chapter by mentioning the layout of this thesis. Chapter 2 introduces the basic principles of NMR, and we have tried only to detail the aspects of the subject which we consider to be important for later discussion. In Chapter 3 we describe briefly the various mechanisms which may occur around the metal non-metal transition. Once again attention is focussed on those which may be important in Na_xWO_3 . Chapter 4 describes the high pressure system, and details points of interest concerning its design, construction and operation. In Chapter 5, we have tried to collect together all the information which exists on Na_xWO_3 up to this point in time, so as to present some sort of cohesive picture of what is a very remarkable and complex system. Also included in this chapter are comparisons with other bronzes and similar compounds, and also a discussion of current ideas on the metal non-metal transition in the bronzes. In Chapter 6, we present our data on the Sodium resonance in Na_xWO_3 and also add some calculations we have performed on electrostatic energies for the clustered and

dispersed models. In Chapter 7 we discuss these results, trying to draw together all the various pieces of data from our own work, and also from all the other measurements on the system. The conclusions which are reached are summarised in Chapter 8. Finally, but of no less importance, are details of the samples and experimental apparatus and techniques, which we have chosen to place in an appendix, so as to maintain the continuity of the arguments in the preceding chapters.

CHAPTER 2

BASIC THEORY OF NMR2.1 Introduction

In this chapter we shall summarise the various nuclear-nuclear and nuclear-electron magnetic and electric interactions which lead to the application of NMR as a probe into the properties of solids. The summary will concentrate on those aspects which will be important for later discussion. For a wider and more detailed treatment, reference is made to five books on nuclear magnetism¹⁻⁵.

2.2 The Basic Theory of Nuclear Resonance

The majority of nuclei possess angular momentum \underline{J} and a magnetic dipole moment $\underline{\mu}$. These two vectors are collinear and are related by

$$\underline{\mu} = \gamma \underline{J} = \gamma \hbar \underline{I} \quad (2.1)$$

where γ is the nuclear gyromagnetic ratio and I is the nuclear spin. The interaction of the nuclear dipole moment with an applied magnetic field \underline{B}_0 is described by the nuclear Zeeman Hamiltonian

$$H = - \underline{\mu} \cdot \underline{B}_0 \quad (2.2)$$

If \underline{B}_0 is taken to lie along the z axis then

$$H = - \gamma \hbar I_z B_0 \quad (2.3)$$

The allowed energies of the system are

$$E_m = - \gamma \hbar B_0 m \quad (2.4)$$

where m can assume any of the $2I+1$ values $m = I, I-1, \dots -I$.

Transitions between adjacent levels may be induced by an oscillating

magnetic field of frequency ω_0 (the nuclear Larmor frequency) applied perpendicular to B_0 if

$$\hbar\omega_0 = \gamma B_0 \quad (2.5)$$

Consider a system of spins in a magnetic field B_0 , isolated from their surroundings but with some nuclear-nuclear interaction. In equilibrium, the populations of two adjacent levels follow a Boltzmann distribution

$$\frac{N_{m+1}}{N_m} = \exp\left(\frac{\gamma \hbar B_0}{kT_S}\right) \quad (2.6)$$

where T_S is a spin temperature characterising the distribution. If equilibrium is disturbed in one part of the system then the nuclear-nuclear interaction will restore the whole system to a common spin temperature with a relaxation time T_2 called the spin-spin relaxation time. If the spin system is now placed in contact with a lattice at temperature T_L , then at equilibrium $T_S = T_L$. If the spin populations are altered such that T_S is no longer equal to T_L , then spin-lattice interaction will restore equilibrium with a characteristic relaxation time T_1 called the spin-lattice relaxation time.

In solids, $T_1 \gg T_2$ and hence the spin-spin interaction maintains a uniform spin temperature throughout the solid during the spin-lattice relaxation process.

2.3 - The Nuclear Dipole Interaction

In solids, the dominant nuclear-nuclear interaction is the nuclear magnetic dipole interaction. For a system of nuclear spins in a magnetic field B_0 , each spin is subject to the static field B_0 , and also to a varying local field produced by its neighbours. The variation in local fields throughout the sample leads to a broadening

of the resonance line.

For N spins, the nuclear dipolar Hamiltonian is

$$H_d = \frac{\mu_o}{4\pi} \sum_{j < k}^N \frac{\underline{\mu}_j \cdot \underline{\mu}_k}{r_{jk}^3} - \frac{3(\underline{\mu}_j \cdot \underline{r}_{jk})(\underline{\mu}_k \cdot \underline{r}_{jk})}{r_{jk}^5} \quad (2.7)$$

Rewriting in spherical polars and using raising and lowering operators

$$\begin{aligned} I^+ &= I_x + i I_y \\ I^- &= I_x - i I_y \end{aligned}$$

the transformed Hamiltonian becomes

$$H_d = \frac{\mu_o}{4\pi} \sum_{j < k} \frac{\gamma_1 \gamma_2 \hbar^2}{r_{jk}^3} (A + B + C + D + E + F) \quad (2.8)$$

where

$$A = I_{jz} I_{kz} (1 - 3 \cos^2 \theta_{jk})$$

$$B = -\frac{1}{4}(I_j^+ I_k^- + I_j^- I_k^+) (1 - 3 \cos^2 \theta_{jk})$$

$$C = -3/2(I_j^+ I_{kz} + I_{jz} I_k^+) \sin \theta_{jk} \cos \theta_{jk} \exp(-i\theta_{jk})$$

$$D = -3/2(I_j^- I_{kz} + I_{jz} I_k^-) \sin \theta_{jk} \cos \theta_{jk} \exp(i\theta_{jk})$$

$$E = -\frac{3}{4} I_j^+ I_k^+ \sin^2 \theta_{jk} \exp(-2i\theta_{jk})$$

$$F = -\frac{3}{4} I_j^- I_k^- \sin^2 \theta_{jk} \exp(2i\theta_{jk})$$

Term A represents the classical interaction between two dipoles whilst term B induces mutual spin flips between dipoles. This "flip-flop" term is an efficient method for diffusion of spin energy throughout the spin system. The C and D terms flip one spin only and the E and F terms flip both spins in the same direction. The

C, D, E, F terms produce absorption lines at frequencies 0 and $2\omega_0$ which are so weak as to be negligible. A truncated dipolar Hamiltonian is therefore formed, containing only the A and B terms which commute with the Zeeman Hamiltonian and hence the truncated dipolar and the Zeeman Hamiltonians are effectively decoupled.

2.4 The Electric Quadrupolar Interaction

Deviations from the interval rule in hyperfine atomic spectra show that in addition to a magnetic moment, the nucleus may also possess an electric quadrupole moment caused by a non-spherical distribution of nuclear charge. The interaction energy of a nuclear charge distribution $\rho(r)$ with an external electric potential $V(r)$ is⁶

$$E = \int \rho(r) V(r) d\tau \quad (2.9)$$

Since the $2I+1$ Zeeman substates each correspond to a different orientation relative to B_0 , and if the electric interaction also depends on orientation, then each substate may be perturbed differently by the electric interaction. Hence we shall focus on that part of the above interaction which depends on the nuclear spin orientation.

Expanding $V(r)$ in a Taylor series about the origin gives

$$\begin{aligned} E = & V_0 \int \rho d\tau + \sum_{\alpha} V_{\alpha}(0) \int \alpha \rho d\tau \\ & + \frac{1}{2!} \sum_{\alpha \beta} V_{\alpha\beta}(0) \int \alpha\beta \rho d\tau + \dots \end{aligned} \quad (2.10)$$

where $\alpha, \beta = x, y, z$ and

$$V_{\alpha}(0) = \left(\frac{\partial V}{\partial \alpha} \right)_{r=0} \quad \text{and} \quad V_{\alpha\beta}(0) = \left(\frac{\partial^2 V}{\partial \alpha \partial \beta} \right)_{r=0}$$

The first term represents the electrostatic energy of a point charge

and being independent of nuclear orientation is of no interest. The second term represents the interaction of the electric dipole nuclear moment which can be shown to be zero since the nucleus has a well defined parity. The third term involves the interaction of the nuclear quadrupole moment with the electric field gradient at the nucleus and is orientation dependent. The next non-zero term involves the nuclear hexadecapole moment, but this and higher terms are usually negligible and so we shall consider only the quadrupole term.

A principal axes coordinate system may always be chosen such that $V_{\alpha\beta} = 0$ for $\alpha \neq \beta$ leaving V_{xx} , V_{yy} and V_{zz} as the only non-zero components. Also since Laplace's equation gives

$$\sum_{\alpha} V_{\alpha\alpha} = 0 \quad (2.11)$$

then the field gradients can be described by two parameters

$$\begin{aligned} \text{eq} &= V_{zz} \\ \eta &= \frac{V_{xx} - V_{yy}}{V_{zz}} \quad \text{the asymmetry parameter} \end{aligned} \quad (2.12)$$

We note that for axial symmetry of the field gradient, $V_{xx} = V_{yy}$ and $\eta = 0$. Also for nuclei in a cubic environment, $V_{xx} = V_{yy} = V_{zz}$ and the quadrupole interaction vanishes. For a spin 0 or spin $\frac{1}{2}$ nucleus there is no orientation dependence of the charge distribution. Hence we only observe quadrupolar effects for nuclei with $I > \frac{1}{2}$ in non-cubic environments.

The quadrupolar Hamiltonian may be written

$$H_Q = \frac{e^2 q Q}{4I(2I-1)} (3I_z^2 - I^2 + \frac{1}{2}\eta(I^{+2} + I^{-2})) \quad (2.13)$$

Q is the quadrupole moment of the nucleus defined by

$$Q = \frac{1}{e} \int \rho(r) (3z^2 - r^2) d\tau$$

If H_Q is small compared to the Zeeman Hamiltonian then it is sufficient to calculate the energy change of each substate m by first order perturbation theory giving

$$E_m^1 = \frac{e^2 q Q}{8I(2I-1)} (3m^2 - I(I+1))(3 \cos^2 \theta - 1) \quad (2.14)$$

where θ is the angle between B_0 and the principal z axis.

Introducing for brevity

$$\nu_Q = \frac{3e^2 q Q}{h 2I(2I-1)} \quad a = I(I+1)$$

$$\mu = \cos \theta \quad \nu_L = \frac{\gamma B_0}{2\pi}$$

then equation (2.14) reduces to

$$E_m^1 = 1/4 h \nu_Q (3\mu^2 - 1)(m^2 - 1/3a) \quad (2.15)$$

The result is that the $m = \pm \frac{1}{2}$ levels are shifted by the same amount so the central transition frequency remains at ω_0 . The remaining energy levels are no longer equally spaced and so produce a series of $2I-1$ lines symmetrically displaced around ω_0 .

If H_Q is of the same order as the Zeeman Hamiltonian then we must consider the second order perturbation. This gives

$$E_m^2 = -h \left(\frac{\nu_Q^2}{12\nu_L} \right) m (3/2 \mu^2 (1 - \mu^2)(8m^2 - 4a + 1) + 3/8 (1 - \mu^2)^2 (-2m^2 + 2a - 1)) \quad (2.16)$$

and leads to a shift in the central transition.

Finally we note that external charges can distort the core electrons so that the actual field gradient seen by the nucleus V_{zz} differs from that calculated neglecting distortion V_{zz}^0 such that

$$V_{zz} = V_{zz}^0 (1 + \gamma)$$

γ is known as the Sternheimer anti-shielding factor⁷.

2.5 The Nuclear-Electron Magnetic Interaction

In the absence of a magnetic field, the interaction between a nuclear moment $\underline{\mu}_I$ and an electron orbital moment $\underline{\mu}_L$ and spin moment $\underline{\mu}_S$ may be described by the Hamiltonian

$$H_{en} = -\frac{\mu_0}{4\pi} \left[\frac{2\underline{\mu}_I \cdot \underline{\mu}_L}{r^3} - \left(\frac{\underline{\mu}_S \cdot \underline{\mu}_I}{r^3} - \frac{3(\underline{\mu}_I \cdot \underline{r})(\underline{\mu}_S \cdot \underline{r})}{r^5} \right) + \frac{8\pi}{3} \underline{\mu}_I \cdot \underline{\mu}_S \delta(r) \right] \quad (2.18)$$

The first term represents the nuclear coupling to the magnetic field produced at the nucleus by the electron orbital momentum. In diamagnetic materials this term vanishes, whereas in paramagnetic materials, the electron orbital angular momentum is usually quenched by the crystalline field.

The term in round brackets is the nuclear coupling to the electron spin. In diamagnetic materials this term vanishes, whereas in paramagnetic materials, rapid electron spin flips much reduce the hyperfine field from that caused by a static spin.

The last term is the Fermi contact term which replaces the spin dipolar term when $r = 0$. The δ function ensures that only those electrons with a finite probability density at the nucleus contribute, and hence this term is restricted to electrons in S states.

The contact term also can take part indirectly in an important

interaction called core polarisation. An electron outside the filled shells of the atomic core can distort the core orbitals by an exchange interaction. In the absence of the outer electron, the core S electrons will be exactly paired and so no hyperfine field is present. However the exchange interaction of the outer electron polarises the spin up and spin down core S states which then interact with the nucleus via the contact process. The total hyperfine field is obtained by summing over all pairs of core S electrons whose exact spin-pairing is altered by the exchange.

2.6 The Knight Shift

In metals, the conduction electrons interact with the nuclei via the interactions of section 2.5, resulting in an extra field ΔB at the nucleus. The quantity

$$K = \Delta B/B_0 \quad (2.19)$$

is known as the Knight shift^{8,9}.

For the contact term, K is usually positive and temperature independent and may be written as

$$K(s) = \frac{8\pi}{3} \frac{\mu_0}{4\pi} \langle |\psi(0)|^2 \rangle_{E_F} \frac{\chi_s \Omega}{\mu_0} \quad (2.20)$$

where $\langle |\psi(0)|^2 \rangle_{E_F}$ is the S electron density at the nucleus averaged over the Fermi surface and normalised in an atomic volume Ω . χ_s is the Pauli magnetic spin susceptibility of the S electron per unit volume and can be expressed as

$$\chi_s = 2\beta^2 \mu_0 \rho(E_F) \quad (2.21)$$

where β is the Bohr magneton and $\rho(E_F)$ is the density of states at the Fermi surface per unit volume for one spin direction.

An effective hyperfine field may be defined as

$$B_{\text{hf}}(s) = \frac{8\pi}{3} \frac{\mu_0}{4\pi} \beta \langle |\psi(0)|^2 \rangle_{E_F} \quad (2.22)$$

and hence K may be written as

$$K(s) = \frac{1}{\beta} B_{\text{hf}}(s) \frac{\chi_s \Omega}{\mu_0} \quad (2.23)$$

For the core polarisation term^{10,11}

$$B_{\text{hf}}(\text{cp}) = \frac{8\pi}{3} \frac{\mu_0}{4\pi} \beta \langle |\psi_{\text{cp}}(0)|^2 \rangle \quad (2.24)$$

where the last term is obtained by summing over all pairs of core s electrons whose exact spin cancellation is altered by exchange with the outer electron. Similarly to equation (2.23)

$$K(\text{cp}) = \frac{1}{\beta} B_{\text{hf}}(\text{cp}) \frac{\chi \Omega}{\mu_0} \quad (2.26)$$

where χ is the spin susceptibility of the outer electron. K due to core polarisation may be either positive or negative and is usually smaller than that due to s contact.

The spin dipolar term gives no contribution to K in metals of cubic symmetry and in non cubic symmetry leads to anisotropic Knight shifts. The orbital term¹² does not contribute to the Knight shift in first order since in metals, the conduction electrons have no orbital angular momentum. However the applied B_0 field can mix in states above the Fermi level (provided the conduction band has some non-s character) to give a paramagnetic shift in second order, usually known as the Van Vleck shift K_{VV}

$$K_{\text{VV}} = \frac{1}{\beta} B_{\text{hf}}(\text{orb}) \frac{\chi_{\text{VV}} \Omega}{\mu_0} \quad (2.27)$$

where χ_{VV} is the Van Vleck susceptibility which is usually much less than χ_{S}

$$B_{\text{hf}}(\text{orb}) = 2\beta \langle 1/r^3 \rangle \quad (2.28)$$

where $\langle 1/r^3 \rangle$ is the averaged value over the conduction electron wavefunction.

2.7 Spin-Lattice Relaxation

2.7.1 Magnetic Relaxation

The fluctuating magnetic fields due to the motion of the conduction electrons can provide an efficient mechanism for spin-lattice relaxation in metals.

The contact term usually dominates the relaxation process if the Fermi surface has s character. The contact part of H_{en} may be written as

$$H_{\text{c}} = -\frac{8\pi}{3} \frac{\mu_{\text{O}}}{4\pi} \gamma_{\text{e}} \gamma_{\text{n}} \hbar^2 \delta(r) (I_{\text{z}} S_{\text{z}} + \frac{1}{2}(I^{+} S^{-} + I^{-} S^{+})) \quad (2.29)$$

Only the first term in the brackets was considered in evaluating K, but the other terms involve mutual spin flips of the nucleus and the electron (analogous to the flip-flop dipolar term of section 2.3) and so provide an efficient mechanism for nuclear relaxation.

An approximate treatment considers the fluctuating hyperfine field as a random perturbation with a correlation time τ giving a power spectrum of $|H_{\text{c}}|_{\text{av}}^2 \tau$ at ω_{O} , where $|H_{\text{c}}|_{\text{av}}$ is the average value of the perturbation, and τ may be estimated from the Heisenberg uncertainty principle

$$\tau \approx \hbar/E_{\text{F}} \quad (2.30)$$

Since the process involves electron spin flips into vacant states above E_{F} , then the fraction of electrons which can take part is

$k_B T/E_F$ where k_B is Boltzmann's constant. Hence the spin lattice relaxation rate may be written

$$\frac{1}{T_1} = |H_c|_{av}^2 \frac{k_B T}{E_F} \tau \quad (2.31)$$

A full quantum mechanical treatment gives

$$\frac{1}{T_1} (s) = \left(\frac{\mu_0}{4\pi}\right)^2 \frac{64\pi^3}{9} \gamma_e^2 \gamma_n^2 \bar{n}^3 \langle |\psi(0)|^2 \rangle_{E_F} \Omega^2 \rho(E_F)^2 k_B T \quad (2.32)$$

which reduces to

$$\frac{1}{T_1} (s) = 4\pi n (\gamma_n B_{hf}(s) \Omega \rho(E_F))^2 k_B T \quad (2.33)$$

For core polarisation¹³ there is a similar relation

$$\frac{1}{T_1} (cp) = 4\pi n (\gamma_n B_{hf}(cp) \Omega \rho(E_F))^2 k_B T q \quad (2.34)$$

where q is a reduction factor arising from the fact that the degeneracy of the p or d wavefunctions produces cancellations in the off-diagonal matrix elements in the Hamiltonian. There is no cancellation in K since that arises from diagonal elements. q is the reciprocal of the degeneracy of the electron wavefunctions. Hence for p orbitals, $q = 1/3$. For d orbitals

$$q = 1/3f^2 + \frac{1}{2}(1-f)^2 \quad (2.35)$$

where f is the fraction of t_{2g} orbitals at the Fermi surface.

The orbital term¹⁴ can be shown to produce a similar relaxation relation

$$\frac{1}{T_1} (orb) = 4\pi n (\gamma_n B_{hf}(orb) \Omega \rho(E_F))^2 k_B T p \quad (2.36)$$

where p is again a reduction factor involving degeneracy. For p electrons $p = 2/9$ and for d electrons

$$p = \frac{2}{3} f (2 - 5/3f) \quad (2.37)$$

We note that for $f = 0$ then $p = 0$, which is a consequence of the fact that the orbital angular momentum has no matrix elements in the e_g manifold.

The dipolar term¹⁴ is smaller than the orbital relaxation rate and is usually expressed as a fraction of the orbital rate. For p electrons, the ratio is $3/10$ whereas for d electrons, the ratio depends on the parameter p of equation (2.37) being of the order of $0.04/p$.

2.7.2 The Korringa Relation

Korringa¹⁵ showed that for the s contact interaction, a simple relation held between K and T_1

$$K(s)^2 T_1(s) T = \frac{\hbar}{4\pi k_B} \left(\frac{\gamma_e}{\gamma_n} \right)^2 \quad (2.38)$$

A similar relation can be shown to hold for the core polarisation interaction¹³

$$K(cp)^2 T_1(cp) T = \frac{\hbar}{4\pi k_B} \left(\frac{\gamma_e}{\gamma_n} \right)^2 \frac{1}{q} \quad (2.39)$$

A Korringa type relation cannot hold for the orbital interaction since K is derived from a second order effect since the diagonal matrix elements of the orbital angular momentum are quenched, whereas the relaxation rate involves off-diagonal elements which are not quenched.

The usefulness of the Korringa relation lies in its ability to indicate competing mechanisms. For example if contact, core polarisation and orbital interactions are important, as is the case

in many transition metals, then the relaxation rates from the three mechanisms will add to produce the total relaxation rate, whereas the shifts may lead to cancellations, since $K(\text{cp})$ will be negative and K_{VV} will usually be small. Hence for the measured relaxation rate, the measured K value may be less than that predicted by equation (2.38).

Deviations from the Korringa relation can also occur due to electron-electron interactions in the conduction electron gas. These interactions enhance the electronic susceptibility and hence the Knight shift¹⁶ by a factor $(1-\alpha)^{-1}$ where α can vary between 0 and 1. Moriya¹⁷ and Narath¹⁸ later showed that these interactions can also enhance the spin-lattice relaxation rate, resulting in a modified Korringa relation

$$K^2 T_1 T = \frac{\hbar}{4\pi k_B} \left(\frac{\gamma_e}{\gamma_n} \right)^2 [K(\alpha)]^{-1} \quad (2.40)$$

where the function $K(\alpha)$ is tabulated by Narath¹⁸. In the alkali metals, the Knight shift is enhanced more than the relaxation rate, so the result is a value of $K^2 T_1 T$ larger than the non-interacting electron value.

2.7.3 Other Relaxation Processes

In metals, the nuclear quadrupole moment can couple to the field gradients produced by lattice vibrations or by the motion of the electrons. Mitchell¹⁹ finds that for s and p wavefunctions that the relaxation rate is of the same order as the non-contact part of the magnetic relaxation. Obata²⁰ relates the quadrupolar relaxation to the magnetic dipolar by

$$\frac{\frac{1}{T_1} (\text{quad})}{\frac{1}{T_1} (\text{dip})} = \left(\frac{e^2 Q}{\gamma_e \gamma_n \hbar^2 I} \right)^2 \frac{3(2I+1)}{10(2I-1)} \quad (2.41)$$

He finds that in most transition metals that the ratio is less than 0.1 and since dipolar relaxation is small, quadrupolar relaxation may be neglected, except in nuclei with a large quadrupole moment and small magnetic moment such as Ta¹⁸¹.

In a metal where the conduction electrons are strongly scattered such that their mean free path is of the order of the lattice constant, standard metallic relaxation theories may not hold. Warren²¹ points out that the electrons produce a fluctuating hyperfine field which may be treated as a random perturbation with a correlation time τ_e , where τ_e is roughly the electron dwell time on a particular site. He obtains a relaxation rate

$$\frac{1}{T_1} \approx \frac{16k_B T}{h} K^2 \left(\frac{\gamma_n}{\gamma_e}\right)^2 \frac{\tau_e}{\hbar N(E_F)} \quad (2.42)$$

For free electrons, $\tau_e \approx \hbar N(E_F)$ and so this equation approximates to a standard Korringa type relation. However in the diffusive regime (which we discuss in chapter 3), Warren proposes that strong scattering causes the electron dwell time on a particular site to increase, hence enhancing the relaxation rate over that predicted by the Korringa relation of equation (2.38) by a factor η where

$$\eta = \frac{\frac{1}{T_1} \text{ measured}}{\frac{1}{T_1} \text{ Korringa}} \quad (2.43)$$

Warren supports his argument with results in three liquid semiconductors. In Ga₂Te₃ at 1400 K, measurement of the magnetic relaxation rates and Knight shifts of all the nuclear species gives $\eta \approx 2$. However close to the melting point at 1065 K, $\eta \approx 150$. Since the diffusive nature of the electron transport causes both a decrease in the conductivity and the enhancement η , Warren is able to show that the two are related by

$$\sigma\eta = \frac{e^2 d^2}{3\Omega\hbar} \quad (2.44)$$

where d is the electron jump distance. It can be shown that a log-log plot of the measured σ and η produces a reasonable straight line and predicts jump distances of the order of the lattice constant, which is what is expected in the diffusive regime. Similar enhancements are obtained for In_2Te_3 but not for Sb_2Te_3 where $\eta \approx 1$ above the melting point. However Sb_2Te_3 has a larger conductivity than the other two and probably cannot be described by diffusive type conduction. Hence it might be expected not to show any enhancements.

Finally, if a substance contains a small amount of paramagnetic impurities, the nuclei can relax via the large fluctuating magnetic fields produced by the localised electron. This relaxation proceeds either by mutual spin flips for those nuclei close to the impurity, or by a process known as spin diffusion for those nuclei further away.

2.8 NMR Lineshapes

2.8.1 Dipolar Broadening

The dipolar interaction of section 2.3 has already been stated to produce broadening of the resonance line. Abragam¹ treats this by the method of moments, defining the n 'th moment by

$$M_n = \int (\omega - \omega_0)^n f(\omega) d\omega \quad (2.45)$$

where $f(\omega)$ is a normalised shape function. For a Gaussian curve, the shape most frequently met in solids, a knowledge of the second moment M_2 can give an approximation to the linewidth at half maximum

ΔB_{dip}

$$\Delta B_{\text{dip}} = \frac{2.36 M_2^{\frac{1}{2}}}{\gamma_n} \quad (2.46)$$

The second moment can be shown to be

$$M_2 = \frac{3}{4} \left(\frac{\mu_0}{4\pi} \right)^2 \gamma^4 \hbar^2 I(I+1) \sum_k \frac{(1-3\cos^2\theta_{jk})^2}{r_{jk}^6} \quad (2.47)$$

where r_{jk} is the distance between the j 'th and k 'th nuclei and θ_{jk} is the angle between \underline{r}_{jk} and \underline{B}_0 . For a powdered sample the angular term is averaged over all directions giving

$$M_2 = \frac{3}{5} \left(\frac{\mu_0}{4\pi} \right)^2 \gamma^4 \hbar^2 I(I+1) \sum_k r_{jk}^{-6} \quad (2.48)$$

This has assumed that the nuclear spins are all "alike". If they are "unlike", the flip-flop term of the dipolar Hamiltonian is quenched and the line may be narrowed. This can also occur if quadrupolar interactions vary sufficiently from site to site to cause the nuclei to look "unlike".

Finally, if the spin system is diluted such that a fraction f of the lattice sites are occupied, then M_2 must be multiplied by f . Hence the linewidth is proportional to $f^{\frac{1}{2}}$. However for $f < 0.1$ the second moment no longer provides a good approximation to the linewidth. The fourth moment must be considered resulting in a linewidth less than that calculated from M_2 alone. The concentration dependence of M_4 produces a linewidth proportional to f for $f < 0.01$. So to summarise

$$\Delta B_{\text{dip}} \propto \begin{cases} f^{\frac{1}{2}} & \text{for } f > 0.1 \\ f & \text{for } f < 0.01 \end{cases} \quad (2.49)$$

2.8.2 Quadrupolar Broadening

First order quadrupolar interaction has already been shown to produce satellites at a distance from the central transition which depends on the orientation of the principal axes relative to B_0 . In powders the random orientation averages the angular term, producing

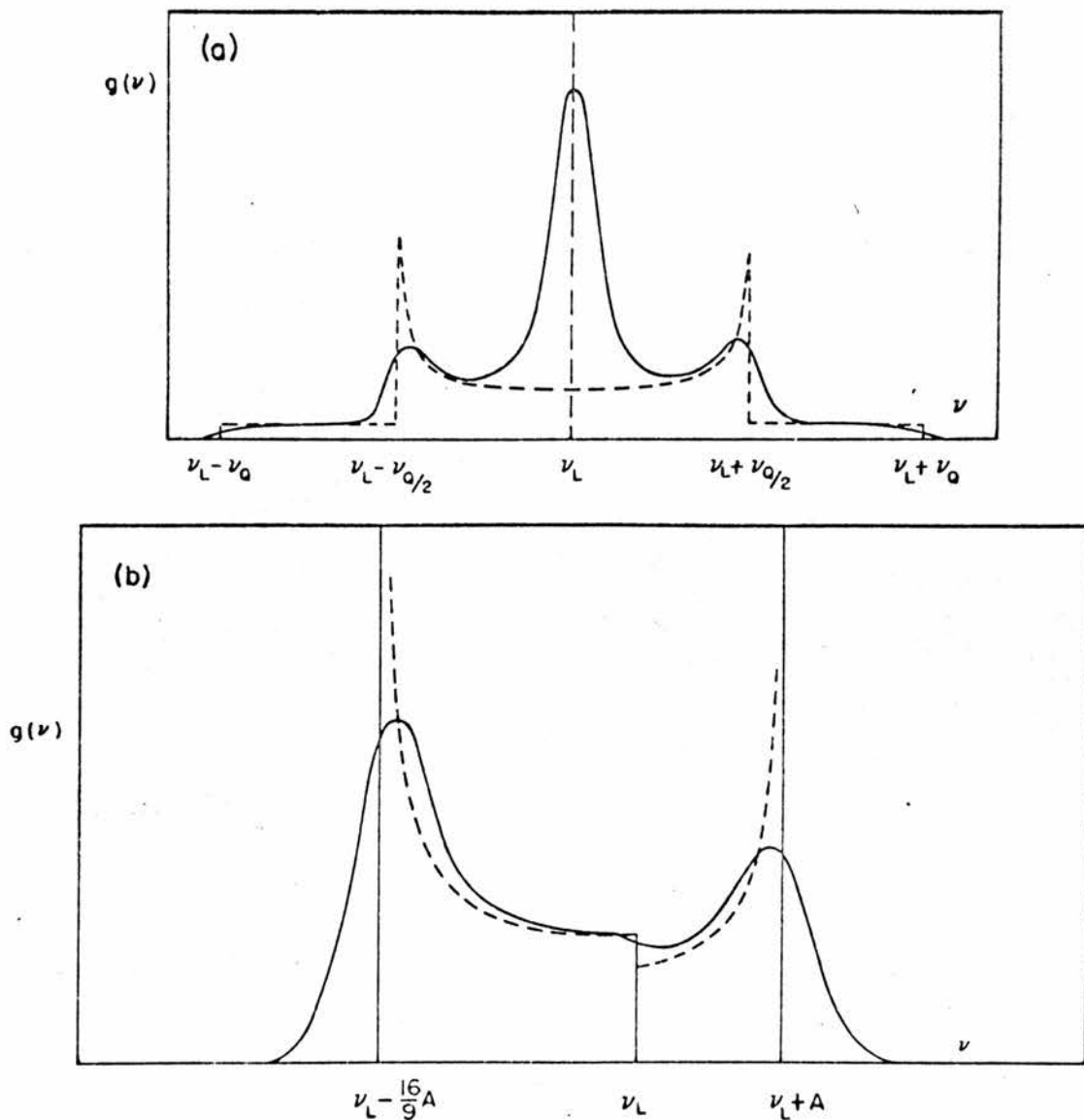


FIG.2.1 Powder patterns for symmetric field gradient.
 (a) First-order pattern for $I = \frac{3}{2}$, $\nu_0 = e^2qQ/2h$. Dashed curve is obtained from Eq.(2.15). With dipolar broadening superimposed, the solid curve results. (b) Second-order pattern, central component, $A = (a - \frac{3}{4})\nu_0^2/(16\nu_L)$. Dotted curve derives from Eq.(2.16). Solid curve includes dipolar broadening.

the lineshape shown in Fig. 2.1a by the dotted line⁶. Here $I = 3/2$ and the two satellites are displaced on either side of the central transition by $\nu_Q/2$. With dipolar broadening superimposed the full curve results.

The second order quadrupole interaction broadens the central transition. The lineshape for the $I = 3/2$ central transition in a powder is shown in Fig. 2.1b by the dotted line, with again the full line including dipolar broadening. For this case

$$A = (a - \frac{3}{4}) \nu_Q^2 / 16\nu_L \quad (2.50)$$

This provides a test for second order quadrupolar broadening, by predicting a linewidth inversely proportional to the resonant frequency.

2.8.3 The Exchange Interaction

An electron on one site tends to align its spin parallel to the nuclear spin on that site. The exchange interaction between electrons tends to make an electron on an adjacent site align its spin antiparallel to the first electron, and so produces a nuclear spin antiparallel to the first nuclear spin. If one nuclear spin changes direction, this indirect conduction electron coupling produces a reorientation of the second nuclear spin. For a system of spins, this may be expressed in terms of an effective exchange Hamiltonian

$$H_{\text{eff}} = \sum_{i,j} A_{ij}(r_{ij}) \underline{I}_i \cdot \underline{I}_j \quad (2.51)$$

In solids, the main effect of this interaction is on the resonance line²². If all the nuclei are alike, the linewidth is reduced. However, if the nuclei are unlike, the line is broadened.

2.9 Pulsed NMR

Although the technique of Pulsed NMR is covered in any basic text, we shall summarise those details required for this work.

The technique is probably best described by the semi-classical treatment of precessing vectors. If B_0 is taken to define the z axes and the coordinates xyz transformed into a frame $x'y'z$ rotating at frequency ω_0 , then an RF field B_1 tips the magnetisation vector \underline{M} out of the z direction by an angle which depends on the duration of B_1 , t_w . In particular, for a pulsewidth of

$$t_w = \frac{\pi}{2 \gamma B_1} \quad (2.52)$$

then M is tipped by $\pi/2$ into the $x'y'$ plane. The decay as the different spin isochromats fan out is measured as the Free Induction Decay (FID) and has the time constant T_2 , which for a Gaussian is related to the absorption linewidth ΔB by

$$\Delta B = 4\sqrt{\ln 2} / \gamma T_2 \quad (2.53)$$

If a second pulse is applied of length twice that of equation (2.52), the isochromats converge in the opposite direction, and a spin echo is formed.

Our first point is that B_1 should be larger than the spectral range under consideration. If large quadrupolar effects are present, the satellites may lie outside B_1 , and hence are apparent only in a reduction in the signal intensity, since only the central transition is observed. There is a reduction factor of 0.4 for spin 3/2. Also if the central transition is broadened in second order, B_1 must be larger than the linewidth, otherwise the intensity will be further reduced, and false information derived from the linewidth.

Secondly, Abragam¹ has shown that if a strong quadrupole interaction makes the $2I+1$ Zeeman levels non-equidistant so that the various transitions may be induced separately, then the pulsewidth necessary to produce the maximum signal is

$$t_w = \frac{\pi}{2\gamma B_1} \frac{1}{I+\frac{1}{2}} \quad (2.54)$$

Hence if the B_1 field is not sufficient for the satellites to contribute to the signal, then not only is the intensity reduced, but also the pulsewidth necessary to produce the maximum signal is reduced.

Finally we discuss Solomon's quadrupolar echo method²³ by which some quantitative information may be obtained on first order quadrupolar interactions. If a $\pi/2$ pulse is followed at a time less than T_2 by a second shorter pulse, a series of allowed and forbidden echoes is produced, due to the different $\Delta m = 1$ transitions. For spin $3/2$, only one echo is produced, and the width of the second pulse required to maximise this echo is $\pi/3$. If this pulse is applied at time t after the first pulse, the echo appears at time $2t$. For spin $5/2$, five echoes are produced, of which three are allowed, and the width of the second pulse is $\pi/5$. If $B_1 > \nu_Q$, the inverse echo width gives a measure of the shift of the satellites. However if $B_1 < \nu_Q$, the inverse echo width is simply equal to B_1 .

CHAPTER 3THE METAL NON-METAL TRANSITION3.1 Introduction

The idea that insulators could sometimes be made metallic, and vice-versa, by external agencies such as temperature or pressure, was first proposed by Mott in 1949. Since then, the subject has expanded so dramatically, that in this chapter we can only review the basic concepts. For a fuller discussion the reader is referred to Mott's recent book²⁴. However despite the vast amount of work in the field, there is much in this chapter which is still uncertain.

3.2 The Mott Transition

In 1949, Mott²⁵ pointed out that the one-electron band theory of Wilson²⁶ did not hold in all cases. As an example, he considered an expanded alkali metal, with the atoms far enough apart for the ionisation energy to preclude conduction. However since the electron wavefunction falls off exponentially with distance, overlap of the wavefunctions will always occur, and the conventional band theory predicts conduction to occur, albeit in a very narrow band. The discrepancy between this theory and experiment lies in the theory neglecting certain interactions important in narrow energy bands.

Contraction of the above system will however result at some point, in a transition to a metallic state. This type of transition is known as a Mott Transition, since Mott first described the formation of the free carriers²⁷. If a small number of free carriers is formed, the electron pairs with the hole left behind to form an exciton, and since the exciton has zero charge, conduction cannot occur. However as more excitons are formed, eventually screening inhibits their formation, and free carriers result. Hence the conductivity transition is accompanied by a discontinuous change in

the number of charge carriers N_c . N_c goes from zero to a value

$$N_c^{1/3} a_H \approx 0.4 \quad (3.1)$$

where a_H is the Bohr radius. This relationship holds quite well in a number of systems²⁸, but the discontinuity question has not been resolved, since experimentally any such transition is usually smeared out by other mechanisms.

3.3 The Mott-Hubbard Model

The Mott Transition of section 3.2 arose essentially from long range Coulomb interactions. Hubbard^{29,30} showed that a model which involves only the short range Coulomb interaction energy U of two electrons on the same site, can also lead to a transition. U is defined by

$$U = \iint \frac{e^2}{r_{12}} |\psi(r_1)|^2 |\psi(r_2)|^2 d\tau_1 d\tau_2 \quad (3.2)$$

An electron on a particular site will favour delocalisation since it gains an energy comparable to the bandwidth B

$$B = 2zI \quad (3.3)$$

where I is the overlap integral and z is the coordination number. However delocalisation involves the electron moving to another site where it must pay the energy U because of the repulsion from the electron already on that site. Hence a transition may occur when $B \approx U$. This is more commonly depicted in terms of the two bands of pseudoparticles shown in Fig. 3.1. The upper Hubbard Band consists of doubly occupied sites and is separated from the lower Hubbard band of singly occupied sites by U . If both bands are constructed from the atomic limit ($1/a = 0$) then they overlap when

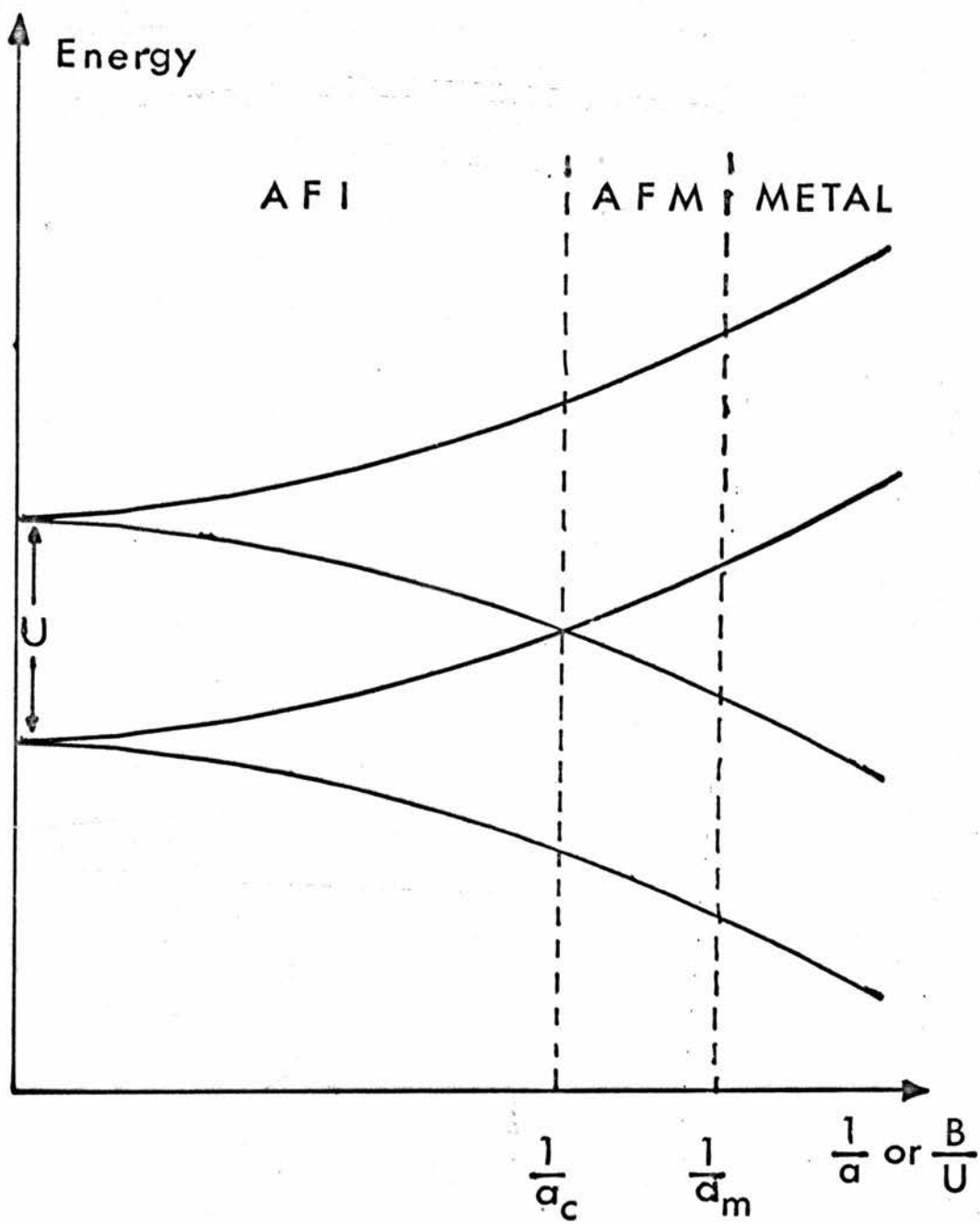


FIG.3.1 The Hubbard bands.

$$B = 1.15 U \quad (3.4)$$

At this point the system becomes metallic with no discontinuity in the number of carriers.

In the insulating region, there is still wavefunction overlap although conduction is prohibited by U . This overlap makes neighbouring spins antiparallel because of the Pauli Exclusion Principle, and hence the system is an antiferromagnetic insulator (AFI).

At a_0 the bands overlap and metallic conduction commences. Herring³¹ showed that Luttinger's theorem³² (that the k space volume enclosed by the Fermi surface is independent of the interaction) is violated unless the system remains antiferromagnetic through the transition. This has led others^{33,34,35} to propose an antiferromagnetic metallic region (AFM) above the transition, but with a second transition at a_m where the AFM region goes over to the Pauli paramagnetism of the metal. Although the AFM region has not been observed experimentally, Mott argues that the long range interactions of section 3.2 will introduce a discontinuity in the number of carriers, and wash out the AFM region.

At a_m the moments disappear, and the system is described as a "highly correlated electron gas". There are two descriptions of this region. One due to Mott³⁶ proposes that it may be energetically favourable for a carrier to align the surrounding spins either parallel or antiparallel to it, up to a distance R . The resultant ferromagnetic sphere, known as a spin polaron, enhances the electronic spin susceptibility, and also enhances the electronic specific heat due to the increase in the carrier mass. The second description is due to Brinkman and Rice³⁷, who show, by a variational method, that correlation can enhance the carrier effective mass. They find that

$$\frac{m^*}{m} = \left(1 - \left(\frac{U}{C}\right)^2\right)^{-1} \quad (3.5)$$

where $C \approx 1/6 B$ but depends on the band shape. They then show that both the specific heat and spin susceptibility are enhanced by the factor on the right hand side of (3.5). Mott has argued that the spin polaron model and the Brinkman - Rice model give essentially the same results.

In many transition metal compounds, the enhancement is of the order of 70, whereas Brinkman - Rice can only produce enhancements of about 10. Although this discrepancy might be explained in some cases, (e.g. VO_x ³⁸) by the formation of a dielectric polaron, Mott²⁴ proposes a refinement of the Brinkman - Rice model by considering correlations between the carrier and the surrounding spins. This can produce enhancements of about 50.

Calculation of U in transition metal compounds gives values of about 20eV, whereas the bandwidths are about 2eV. It is proposed³⁹ that screening reduces U to a value $U_{scr} \approx 2eV$ so the transition occurs when

$$B \approx U_{scr} \quad (3.6)$$

Screening will not be so effective when the number of vacant orbitals is small, which may explain why the oxides of Fe, Co and Ni are non-metallic.

We note at this point, that NMR may provide information on the highly correlated gas. As an example, we quote work on Si:P. As the P concentration N_c is increased, this substance undergoes a transition from a semiconductor to a metal around $N_c \approx 3 \times 10^{18} \text{ cm}^{-3}$. As the transition is approached from the metallic side, both the Silicon resonance⁴⁰ and the Phosphorous resonance⁴¹ show Korringa products greater than those predicted by the standard relation. This is interpreted⁴⁰ as being caused by the electron-electron interactions discussed in section 2.7.2.

3.4 Disorder and Anderson Localisation

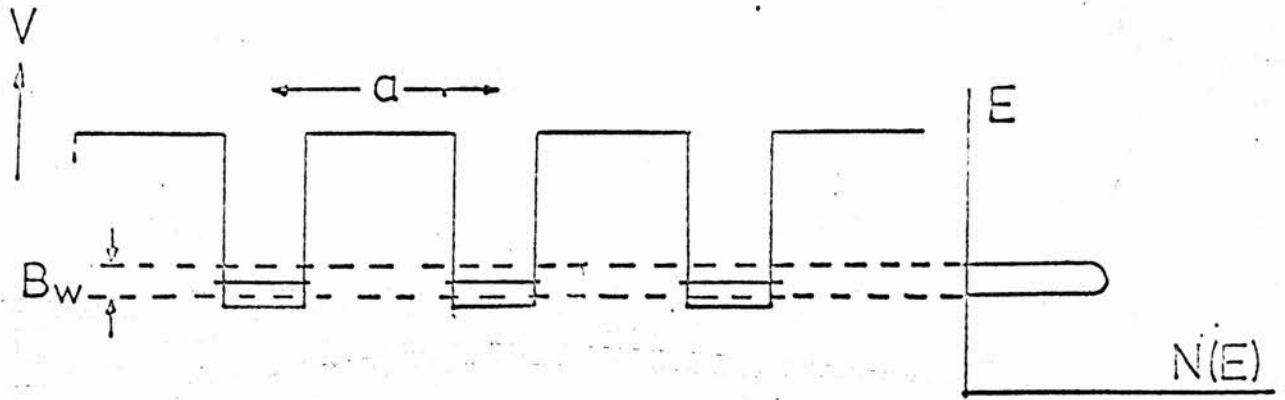
Anderson⁴² was the first to show that the random potential generated by disorder can localise the electron wavefunctions. Fig. 3.2a shows a regular array of potential wells with the resultant density of states. The wavefunction for such a system is shown in Fig. 3.3a and is described as "extended". If a random potential within the limits $\pm \frac{1}{2}V_0$ is added to each well as in Fig. 3.2b, then the density of states is broadened due to some states now having substantially more or less than the average energy. The corresponding wavefunction is shown in Fig. 3.3b and is tending towards localisation. Anderson proposed a critical value $(V_0/B)_{\text{crit}}$ above which all electron states are localised and the system is described as a "Fermi glass". Anderson originally found the critical ratio to be about 5, but more recent work⁴³ gives

$$\left(\frac{V_0}{B}\right)_{\text{crit}} \approx 2 \quad (3.7)$$

We have considered an example of vertical disorder, where a random potential is applied to each site. If the position of each site varies so that the overlap integral from site to site varies, then we get an example of lateral disorder. Kikuchi⁴⁴ and Mott⁴⁵ have treated pairs of sites as having a spread of energies V_0 and hence both types of disorder may be treated by the Anderson theory.

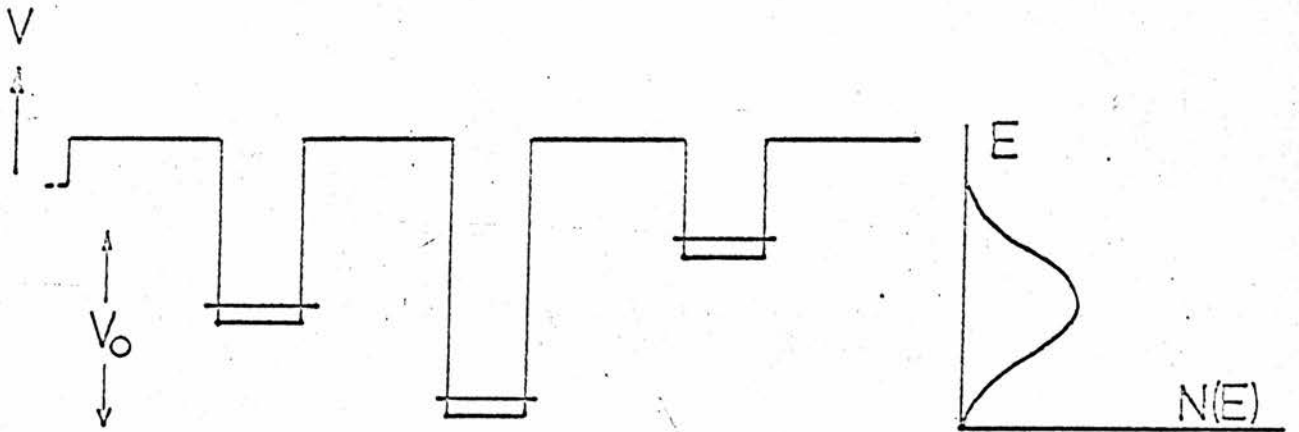
Mott⁴⁶ has argued that Anderson localisation may occur in band tails as in Fig. 3.4a since the band tails have states which experience more disorder. The localised states are separated from the extended states by the mobility edges E_c and E_c' . If by some external agency, such as pressure or doping, the Fermi level crosses E_c into the localised region, then at zero temperature, a discontinuous drop in the number of carriers, from a finite value to zero, will result. This type of metal-non metal transition is usually

FIG. 3.2a



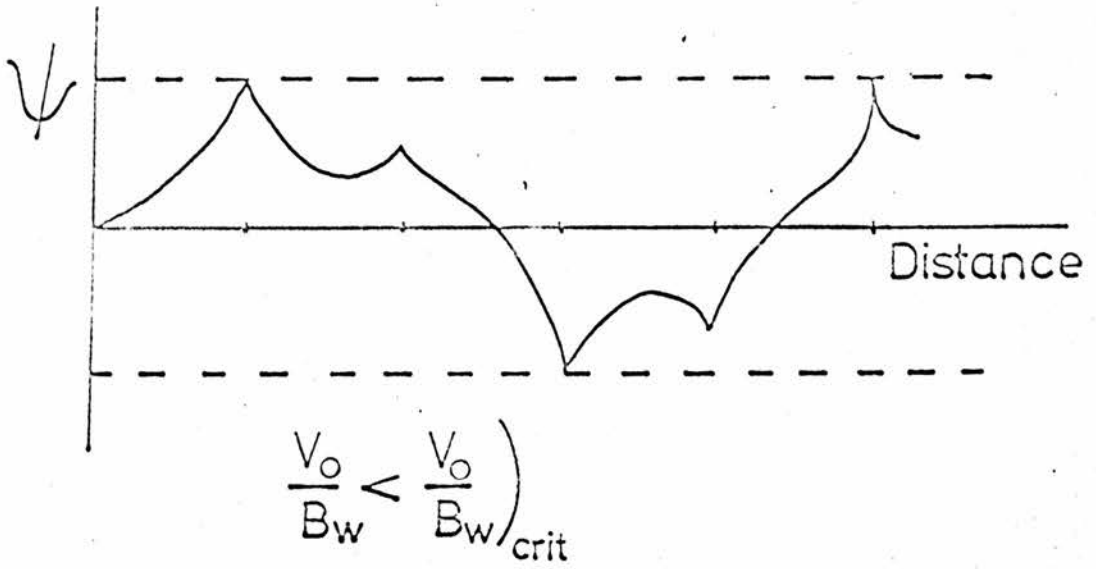
Potential wells for crystalline lattice.

FIG. 3.2b



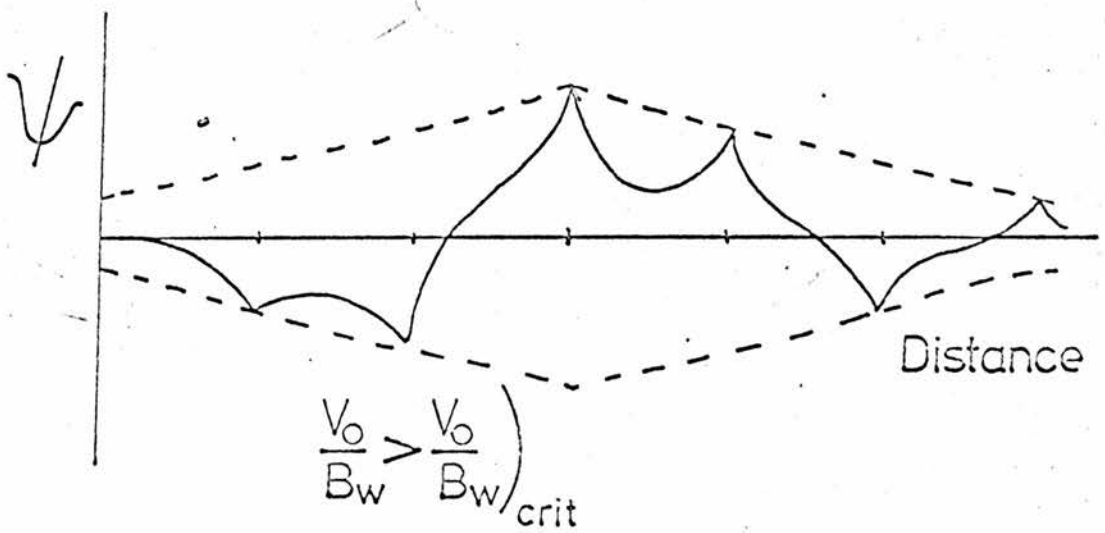
Potential wells for Anderson lattice.

FIG. 3.3a



Wave Function for L-a. Extended states.

FIG. 3.3b



Weakly localised states.

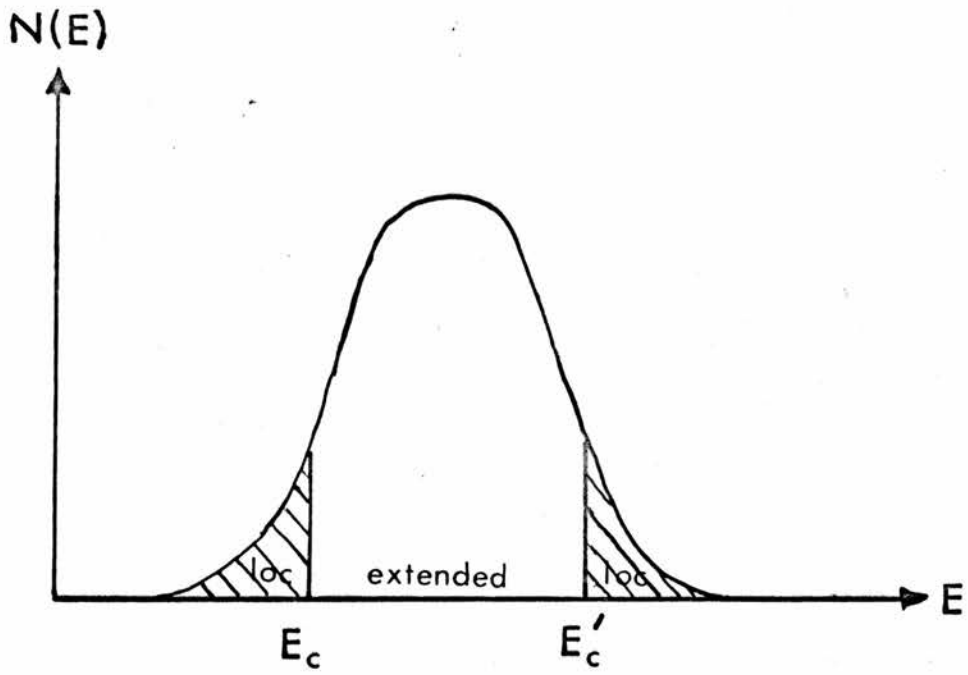


FIG. 3·4a

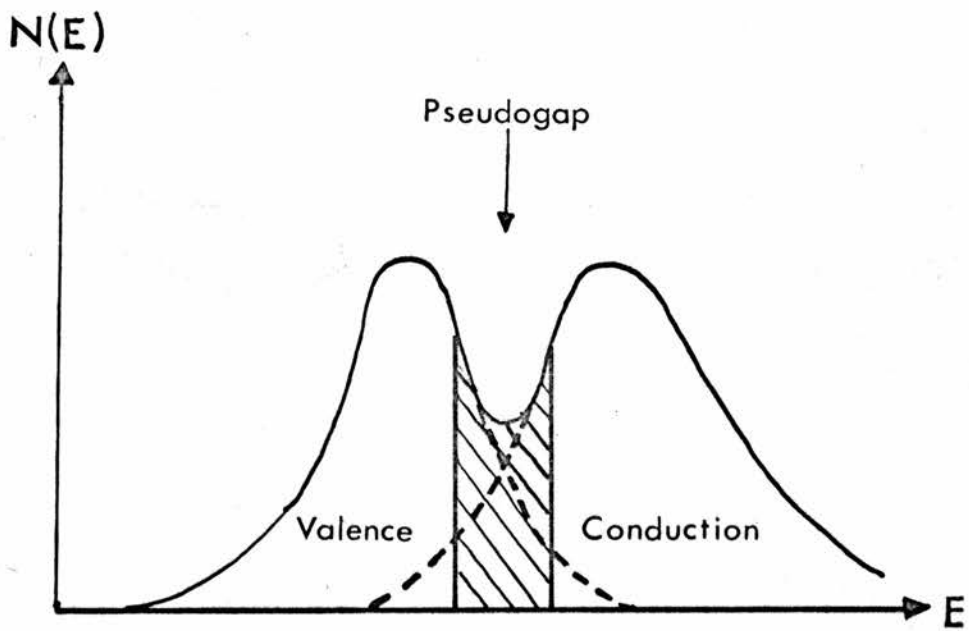


FIG. 3·4b

called an Anderson transition. A logical extension to the model occurs when two bands overlap, as in Fig. 3.4b, to form a pseudogap. If the tails of the two bands are localised, then the states in the pseudogap may also be localised. This situation may arise for both electronic bands and Hubbard bands.

3.5 The Different Conductivity Regions

We shall study the different mechanisms for conduction for different values of V_0/B .

A. The normal metal

When V_0/B is very small, the electron mean free path L is greater than the atomic spacing a . In this region, the wavevector k is a good quantum number, and the conductivity is described by the Boltzmann formulation

$$\sigma = \frac{S_F e^2 L}{12\pi^3 \hbar} \quad (3.8)$$

where S_F is the area of the Fermi surface.

B. The diffusive region

For values of V_0/B just less than $(V_0/B)_{\text{crit}}$, the scattering of the electrons has become so strong that $L \approx a$. Here k is no longer a good quantum number and the Boltzmann formulation fails. Although the conduction is still metallic in nature, the electron moves with a diffusive type of motion, being scattered from adjacent lattice sites. Conduction in this diffusive region is best described by the Kubo - Greenwood formulation, where the mean free path is treated as the length in which an electron loses all phase memory. The conductivity may be written as

$$\sigma = \frac{2\pi e^2 h^3}{m^2} |D_E|_{av}^2 (N(E_F))^2 \quad (3.9)$$

where $|D_E|_{av}$ is the average value of all the phase shifts. For a free electron density of states it can be shown⁴⁷ that (3.9) reduces to

$$\sigma = \frac{3}{16} \frac{S_F e^2 L}{\pi^3 h} \quad (3.10)$$

which agrees with the Boltzmann value except for a numerical factor.

If we assume that $L = a$ and put $S_F = 4\pi k_F^2$ with $k_F = \pi/a$, then we get some idea of the conductivity σ_d at which the diffusive regime starts

$$\sigma_d = 3000 \Omega^{-1} \text{cm}^{-1}$$

In the diffusive regime, the density of states at the Fermi surface is determined by the distribution of random energies so we may write

$$N(E_F) \approx \frac{1}{a^3 V_0} \quad (3.11)$$

and inserting in equation (3.9) gives

$$\sigma \approx \frac{\pi}{4z} \frac{e^2}{\hbar a} \left(\frac{B}{V_0}\right)^2 \quad (3.12)$$

Assuming $z = 6$ and that at the transition $B/V_0 = \frac{1}{2}$ then we get an estimate of the minimum metallic conductivity⁴⁸

$$\sigma_{\min} = 300 \Omega^{-1} \text{cm}^{-1}$$

Hence at zero temperature there is a discontinuous drop in conductivity from σ_{\min} to zero. We note that in d band materials, the d orbital lobes have definite directions hence reducing z and increasing

σ_{\min} . For example in VO_x , $\sigma_{\min} = 1000 \Omega^{-1} \text{cm}^{-1}$.

The transport properties in the diffusive regime may be described as follows⁴⁹. $N(E_F)$ drops below the free electron value $N(E_F)_{\text{FE}}$ either by formation of a pseudogap, or by a reduction in the density of states due to disorder. Defining

$$g = \frac{N(E_F)}{N(E_F)_{\text{FE}}} \quad (3.13)$$

the conductivity may be written as

$$\sigma = \frac{3}{16} \frac{S_F e^2 L}{\pi^3 \hbar} g^2 \quad (3.14)$$

According to Friedman⁵⁰, the Hall coefficient R_H should obey

$$R_H = \frac{0.7}{\text{neg}g} \quad (3.15)$$

Mott considers that localisation should occur when $g \approx 1/3$ so going through the diffusive region, σ should fall by a factor of 9 and R_H should increase threefold.

C. The Insulating region

For larger values of V_0/B , the Fermi level lies in the localised state region, and conduction arises either from excitation to a mobility edge, or by thermally activated hopping at the Fermi level. In the hopping process we consider a set of sites between which the electron can hop, provided the energy difference is less than $k_B T$. At high T , the electron hops to nearest neighbours⁵¹ since the transfer integral is largest for these sites. At low T , it is probable that the electron cannot find a nearest neighbour within $k_B T$, and so must hop to a distant site. This latter phenomenon is known as variable range hopping or $T^{\frac{1}{4}}$ hopping because of the temperature dependence of

the conductivity

$$\sigma = A \exp\left[-\left(\frac{Q}{kT}\right)^{\frac{1}{4}}\right] \quad (3.16)$$

where A and Q are constants.

3.6 Percolation

Cohen and Jortner⁵² have criticised Mott's proposal of the conductivity discontinuity at an Anderson transition, arguing that long range potential fluctuations will produce metallic clusters separated by insulating regions. The conductivity depends on connections between these clusters, enabling the system to be treated by percolation methods. This predicts a continuous drop to zero in the conductivity when it is no longer possible to connect the metallic clusters across the sample. However Mott has shown⁴⁸ that the wavefunctions in the metallic regions penetrate the insulating regions to such an extent that tunnelling can occur between metallic regions. This brings back a discontinuous transition, although possibly with a lower σ_{\min} .

Experimentally, most systems which show Anderson localisation have conductivities comparable with σ_{\min} . If clustering exists, then as the temperature is lowered, the contributions to σ from the non-connected clusters should freeze out, and hence σ should tend to a constant value much less than σ_{\min} . Experiments down to 50 mK in n type compensated Germanium did not show this⁵³. Webman, Cohen and Jortner⁵⁴ have recently proposed large 100 Å diameter metallic clusters to occur in the Alkali Tungsten Bronzes, but Tunstall⁵⁵ has pointed out that X-ray and NMR data do not support this.

It seems therefore that clustering probably does not occur in most disordered solids, although it probably does occur in liquids near critical points.

CHAPTER 4HIGH PRESSURES4.1 Introduction

Although the density stands on an equal footing with the temperature in the thermodynamical description of a solid, it is only comparatively recently that pressure has been used to vary the density. Undoubtedly, the reason for this is that whereas temperature variation is relatively simple, pressure requires large and frequently dangerous equipment. The pioneering work in the field was carried out in Harvard by P.W. Bridgman⁵⁶, who during fifty years and some one hundred papers, developed much of the theory and apparatus for pressures up to 30 KBar. The application of pressure to NMR is mainly due to Benedek^{57,58} and is reviewed in his book⁵⁹. Although much of the art of high pressure has been perpetrated by oral tradition, some reviews do exist⁶⁰⁻⁶⁴.

In this chapter we shall describe a system capable of producing static hydrostatic pressures up to 5 KBar at liquid helium temperatures, for use in NMR. Although in comparison to recent Russian attempts to produce metallic hydrogen at 2 MBar, the pressure here may only be described as "modest", it is still high enough to warrant a section on safety considerations.

4.2 The Choice of Solid Helium as the Pressure Transmitter

Hydrostatic pressure is usually applied to a solid by embedding it in some medium which is under pressure. The assumption is that the pressure transmitting medium pressurises the outer layers which then transmit the pressure inwards, resulting in hydrostatic pressure throughout the sample. The validity of this assumption may depend on sample geometry and compressibility, but it is usually taken as a reasonable approximation.

At room temperature, the use of a fluid transmitting medium is most convenient. Gases are seldom used because of the danger of their large stored energy, but liquids such as Propanol, pentane/methyl butane mixtures⁶⁵ and Kerosene/Oil mixtures⁶⁶ may be pressurised up to 30 K Bar before showing signs of solidification. At low temperatures, a soft solid must be used, since at 4.2 K and at pressure, all substances are solid. Helium is the last to go - at 4.2 K with 140 Bar. Typical solids used are solid Helium⁶⁷, Ice⁶⁸, Silver Chloride⁶⁹, Indium or frozen Kerosene/Oil mixtures⁶⁶.

For a pressure transmitter to produce truly hydrostatic pressure, it must be incapable of sustaining any permanent shear stress. This condition holds in fluids, but not in solids. Hence a solid pressure transmitter can only produce an approximation to hydrostatic pressure. We shall now try to justify our choice of solid Helium 4 as our pressure transmitter.

The early work on solid Helium⁶⁷ involved a constant volume freeze in which a chamber containing high pressure Helium gas was sealed off, and then cooled through the melting curve down to liquid Helium temperatures. This method suffered from a 25% loss in pressure accompanied by pressure gradients along the sample. Recent work almost always involves a constant pressure freeze⁷⁰ which does not suffer from these disadvantages. In this method, Helium is frozen upwards from the bottom of the high pressure chamber, more gas being added at the top to keep the pressure constant, so that a position is maintained on the Helium melting curve in Fig. 4.1. If the fluid-solid interface is moved very slowly up the sample, a single crystal of solid Helium is grown around it, producing nearly hydrostatic pressure. When this interface reaches the top of the chamber, the chamber may be considered as sealed, and so subsequent cooling is at constant volume, with the pressure following the isochores in Fig. 4.1. The loss of pressure in going from the

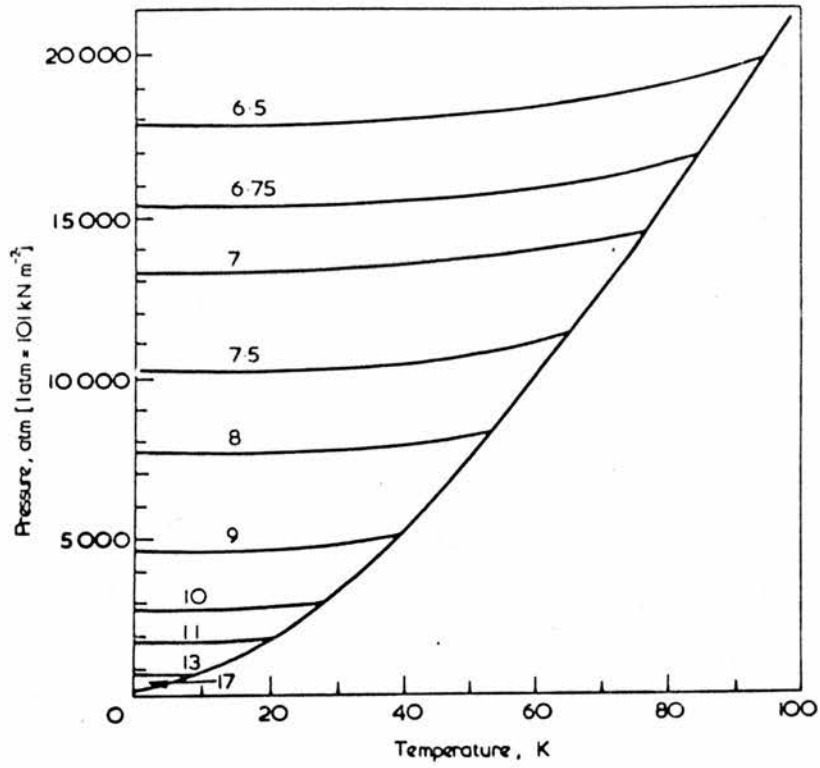


FIG 4.1 Melting curve & isochores of solid He.

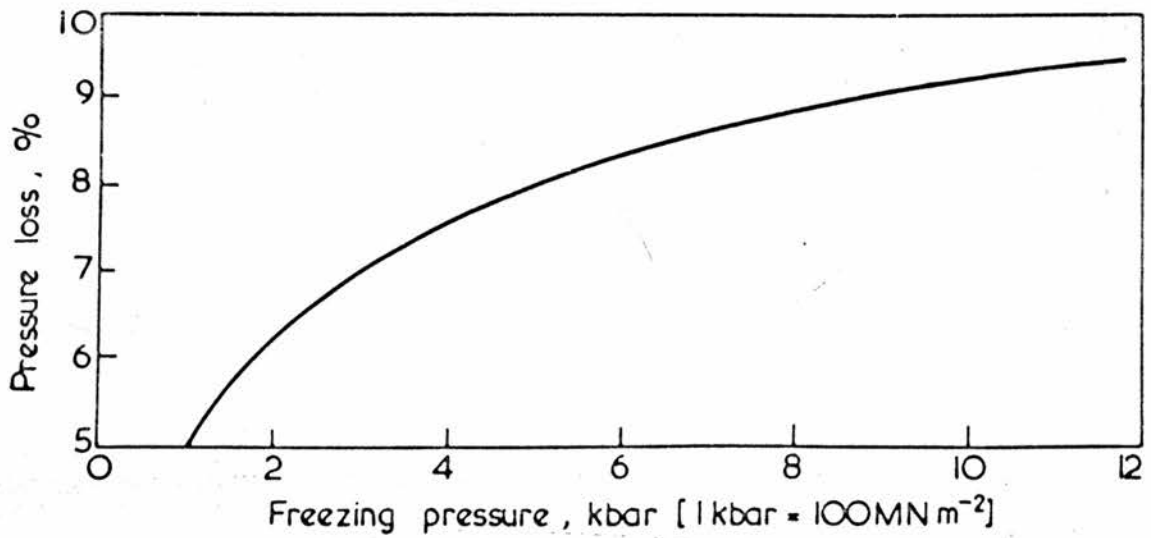


FIG.4.2 Pressure Loss on cooling along isochore to 0 K.

solidification temperature to 4.2K is several per cent and is plotted in Fig. 4.2 as calculated from PVT data⁷¹.

Much evidence has been gathered to show that solid Helium does provide nearly hydrostatic pressure⁷². Narrow superconducting transitions can be maintained at pressures up to a few KBar in solid Helium, indicating uniform stress over the sample^{73,74}. The pressure derivative of the third zone needle pocket cross section in the Fermi surface of zinc shows agreement between pressures produced by solid⁷⁵ and fluid Helium⁷⁶, whereas the solid Kerosene/Oil mixture gives a derivative too small⁷⁷, and the ice-bomb method gives the wrong sign⁷⁸. Also NMR in solid Helium⁷⁹ shows evidence of rapid diffusion even at low temperature and high pressure, indicating that solid Helium behaves very like a fluid.

In conclusion, it seems that the solid Helium technique is the best method for producing nearly hydrostatic pressure at low temperature. It suffers from two disadvantages.

Helium gas must be compressed, with the danger of its stored energy. This is overcome by reducing the system volume to a minimum.

A thermal cycle taking several hours is required to change the pressure, although the magnitude of this cycle is less for Helium than any other substance. This disadvantage was not too limiting since the samples were kept at one pressure for one or two days. Hence the pressurisation time formed a small part of the total experimentation time.

4.3 The Pressure Generating System

The gas pressure generating system shown in Fig. 4.3 may be divided into three sections for description.

A. The gas charge section consists of a Helium gas cylinder at pressures up to 140 Bar, which feeds the Haskel AG152 compressed air

driven Helium compressor. The 152 indicates the ratio of the maximum output gas pressure to the air drive pressure. Using the Department compressed air supply at ≈ 7 Bar, the AG152 can compress the Helium to ≈ 1 KBar. The Helium cylinder is protected from blow-back from the AG152 by the relief valve RV1, set at 155 Bar, and the whole charge section was protected from blow-back from the high pressure section by a rupture disk RV2, set at 1.4 KBar.

B. The oil drive section consists of an air driven Haskel M188 compressor, the ratio 188 implying a maximum oil drive of ≈ 1.3 KBar. The oil, Tellus 27, was contained in the reservoir. The intensifier was protected from over-driving by the relief valve RV3, set at 900 Bar.

C. The High Pressure side consists of the Harwood B 2.5 J Intensifier (shown schematically in Fig. 4.4) and the high pressure cell. The 11:1 intensification ratio, coupled with the maximum oil drive of 900 Bar set by RV3, indicate that pressure up to ≈ 10 KBar should be produced. However the Harwood intensifier is only rated up to 7 KBar, and so this was taken as the pressure limit of the system. The space between the intensifier pistons is filled with Tellus 27 oil, and connected to a glass tube as in Fig. 4.4. The oil level in the tube then indicates the piston position. The pressure is measured by a Heise bourdon tube type gauge, which is accurate to better than ± 7 Bar, and has a range of 0 to 7 KBar. All tubing and fittings are standard Harwood or Nova Swiss⁸⁰. 2M and 3M are used in the high pressure section, and the lower rated 4L used in the charge and drive sections.

Since the NMR cell cannot be fixed in position, it is connected to the rest of the system by flexible high pressure tubing (1/16 inch OD and 7 thou. ID). This tubing is made suitable for insertion into the 2M fittings by drilling out a one inch length of 2M tube to 1/16 inch ID, and then silver soldering this over the flexible tube. The end of this composite tube is then prepared in the normal way as for 2M.

Two major problems have arisen in the construction of this system. The first was that the original Harwood seal at the intensifier top leaked. The seal involved an O ring which was pressed against the walls by the pressure.

If this type of seal leaks at low pressure, then applying more pressure cannot force a seal. Several attempts with different O ring sizes and materials all failed. It was decided to build another design of sealing plug (Fig. 4.5) which allowed preloading of the sealing washer A, i.e. the washer may be compressed against the walls mechanically before pressure is applied. The entire plug is placed in position and the top section B is screwed down. This forces the bottom section C upwards against the middle section D, causing the Teflon sealing washer A to extrude outwards onto the wall, and inwards onto the plug stem. This plug has worked so well that we would recommend its inclusion in any intensifier of this type.

The second problem is the dead volume of the Heise gauge (≈ 15 ccs). Not only is this large volume dangerous, but it also means that more than one cycle of the intensifier must be used to produce pressures above about 3KBar. Although this problem has been lived with, work is in progress to replace the Heise by a manganin resistance cell type gauge^{56,81}.

The operation of the system may be described by the following sequence.

1. With the intensifier piston at the bottom of its stroke, and with Charge and Discharge valves open and Pressure Release valve closed, the Helium cylinder valve is opened, hence taking the whole gas section to cylinder pressure.
2. The AG152 is operated until the charge pressure has reached its maximum of about 1 K Bar. The Charge valve is then closed.
3. The M188 compressor is operated until the intensifier piston has reached the top of its stroke. This produces about 3 K Bar in the high pressure gas section. The discharge valve is then closed.
4. If higher pressure is desired, the cycle must be repeated. The drive pressure release valve is opened and the intensifier piston falls back to the bottom again. The Charge valve is opened, the AG152 operated until the charge pressure is a maximum, and then the charge valve closed. The discharge valve is then opened, allowing the high pressure section to fall to about 1.5 K Bar. The operation is repeated as from 3, except that the higher charge pressure enables pressurisation of the high pressure section to above 5 K Bar.
5. To release the pressure, the intensifier piston must be at the bottom of its stroke, or damage to the piston ensues. Opening the Pressure release valve releases the pressure (in our case into the Helium return line to our Cryogenic facility).

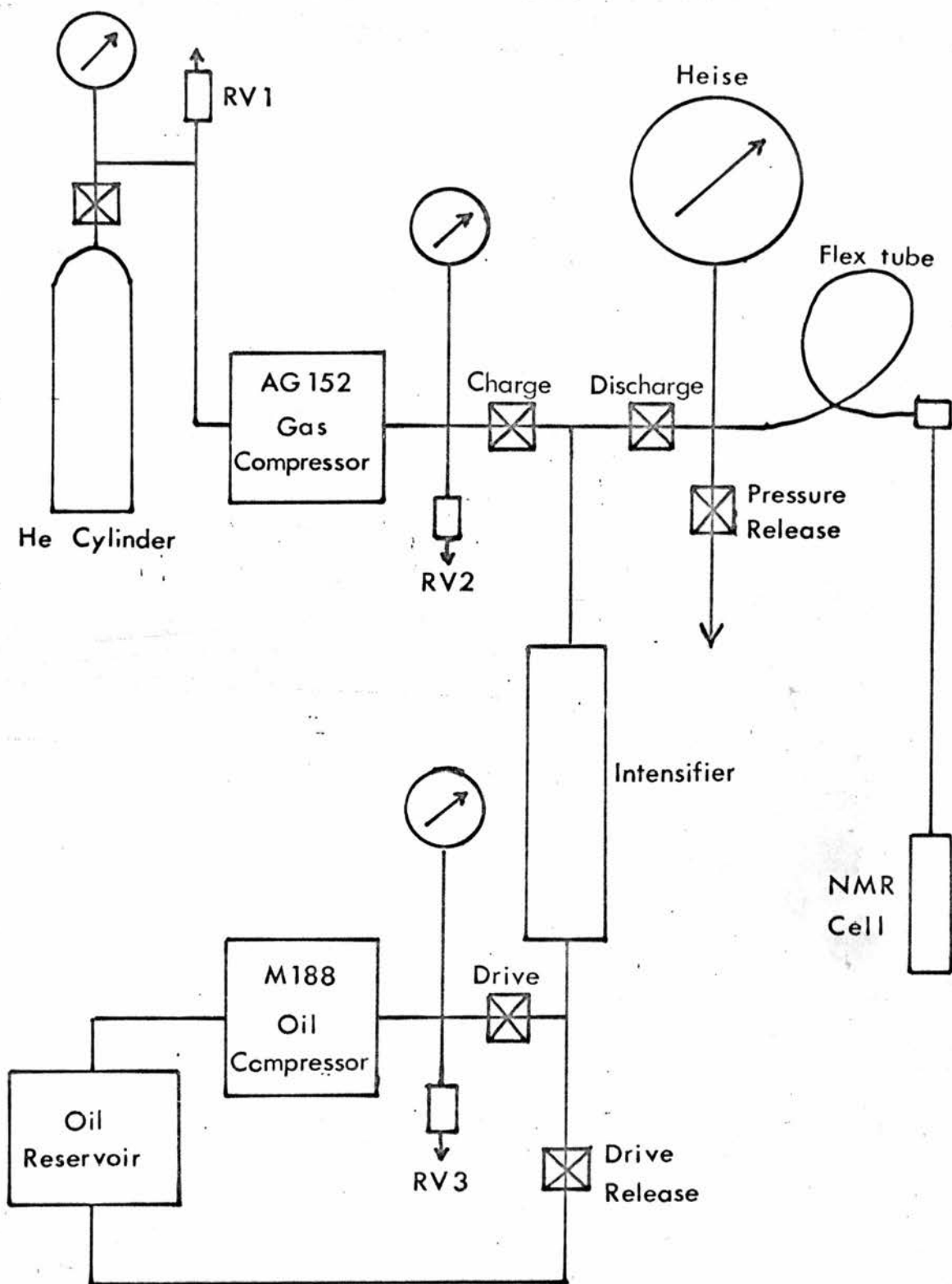


FIG 4•3 The Pressure System

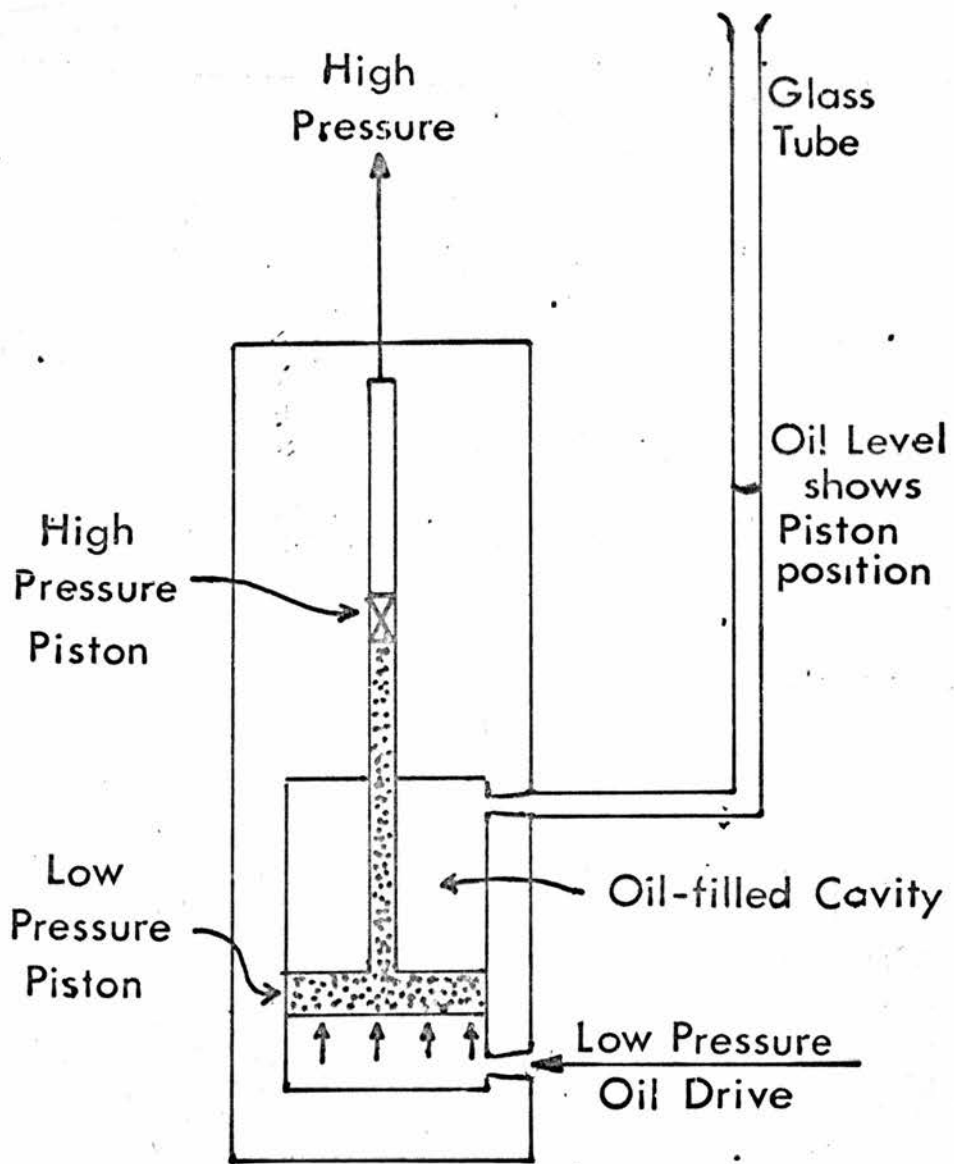


FIG 4.4 Harwood Intensifier

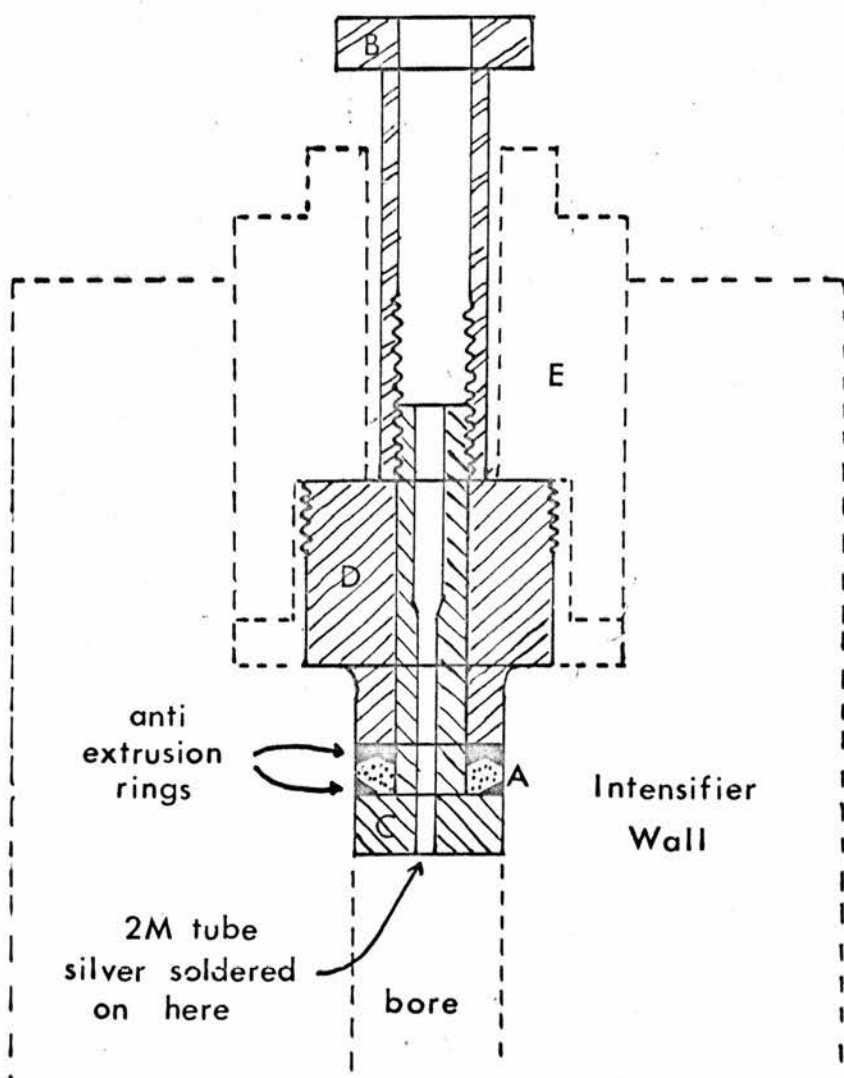
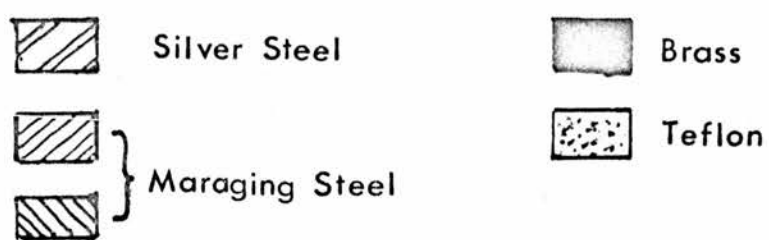


FIG 4-5 Modified Intensifier Top Seal

4.4 The High Pressure NMR Cell

Before describing the cell, it is useful to discuss briefly the reaction of a thick walled metallic cylinder to pressure in its bore. The stress-strain diagram for such a cylinder is shown in Fig. 4.6a. Initially, pressure causes the cylinder to expand elastically, in the sense that removal of the pressure causes the cylinder to revert to its original shape. As the pressure is increased, a point is reached A, at which the stress at the bore (where the stress is greatest) equals the yield stress. This pressure is known as the yield pressure P_y , and is given by^{62,82}

$$P_y = \frac{1}{2} \sigma_y \left(1 - \frac{1}{K^2}\right) \quad (4.1)$$

where σ_y is the yield strength of the material and K is the ratio of o.d./i.d. of the cylinder. For pressures greater than P_y , the inside region of the wall behaves plastically, causing small permanent deformations. However the outside region is still elastic, and hence a plastic-elastic boundary is set up in the wall, as shown in Fig. 4.6b. Further increase of pressure causes this boundary to move outwards until at B, the whole wall is plastic. Any further increase leads to a ballooning of the vessel, and shortly afterwards, at C, the vessel bursts. The ultimate burst pressure P_b can be calculated from⁸²

$$P_b = 2\sigma_u \left(\frac{K-1}{K+1}\right) \quad (4.2)$$

where σ_u is the ultimate tensile strength of the material.

If the cell is pressurised beyond P_y and the pressure removed, the permanent deformation of the inside region of the wall makes that region harder. Hence subsequent pressurisation can be made to higher pressure. This process, known as autofrettage, can extend the usable pressure range. It is recommended that autofrettage should not take the plastic region further than the geometric mean of the outer and

inner diameters. This pressure is given by⁸²

$$P_a = \frac{\sigma_y}{2} \left(1 - \frac{m^2}{K^2}\right) + \sigma_y \ln m \quad (4.3)$$

where m is the plastic elastic boundary diameter divided by the inner diameter. Cells autofrettaged to this pressure may have their usable limit extended by up to 50%.

The cell used in this work is shown in Fig. 4.7. The requirement that the cell should be non-magnetic at low temperatures led to the choice of Beryllium-Copper alloy, rather than a high strength steel. The particular alloy used was Be-Cu 250 (1.8% Be) supplied by Telcon Metals Ltd. The ingot was machined in the annealed state, and then heat treated for 4 hours at 315°C, resulting in a high strength alloy with

$$\begin{aligned} \sigma_u &= 11.8 \text{ K Bar} \\ \sigma_y &= 10.4 \text{ K Bar} \end{aligned} \quad (4.4)$$

The cell had to clear the bore of a superconducting magnet which restricted the o.d. to 48 mm, and the requirement of a large sample volume for the NMR necessitated an i.d. of 16 mm. Hence with $K = 3$,

$$\begin{aligned} P_b &= 11.8 \text{ K Bar} \\ P_y &= 4.6 \text{ K Bar} \end{aligned} \quad (4.5)$$

The high pressure gas enters the top of the cell via 2M tubing, and a standard type fitting. The Harwood 2M steel gland nut and collar were found to be magnetic and so were replaced by ones machined from Be-Cu. The head of one of these sheared on tightening, and so it was decided to use a larger gland nut to avoid this. This necessitated insertion of a spacer, to ensure the 2M tubing remained central in the larger hole.

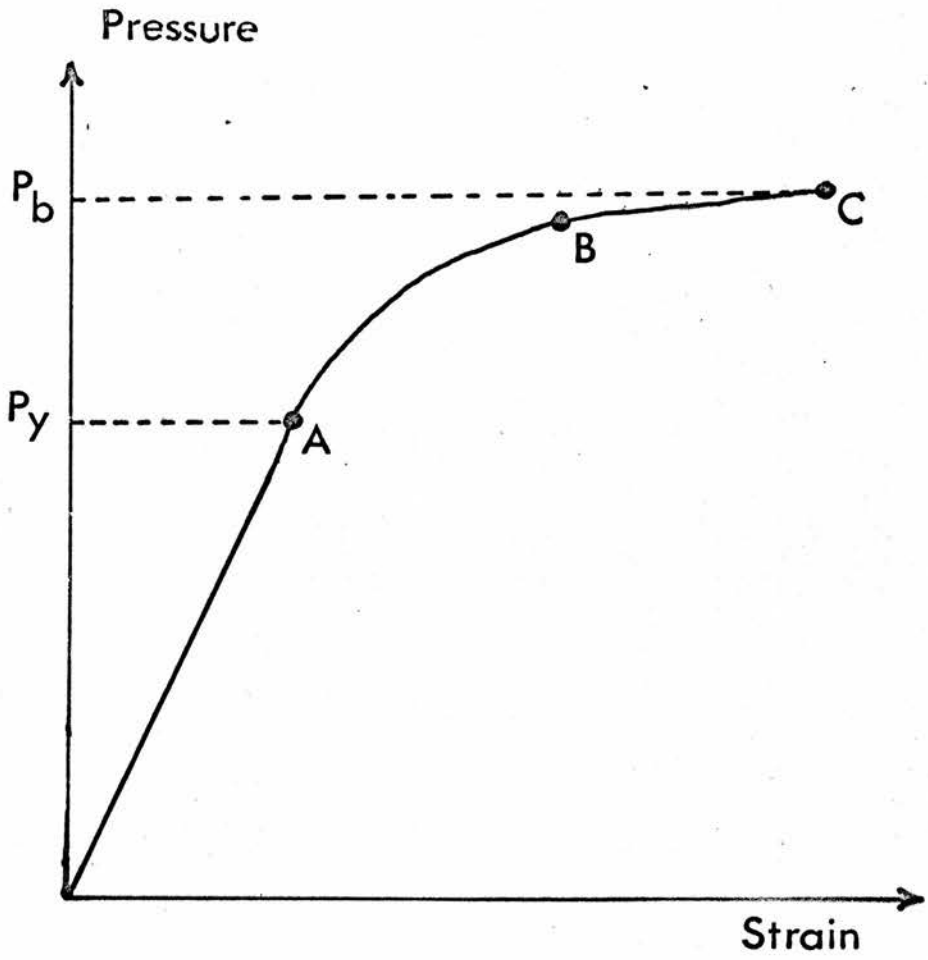


FIG 4.6a

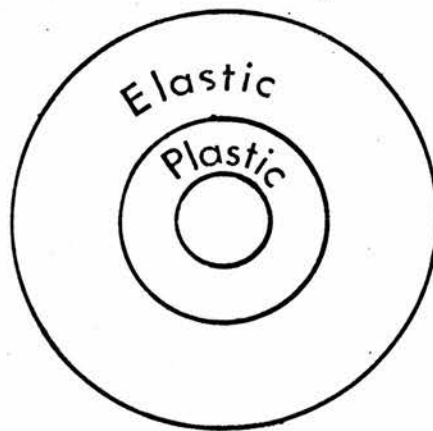
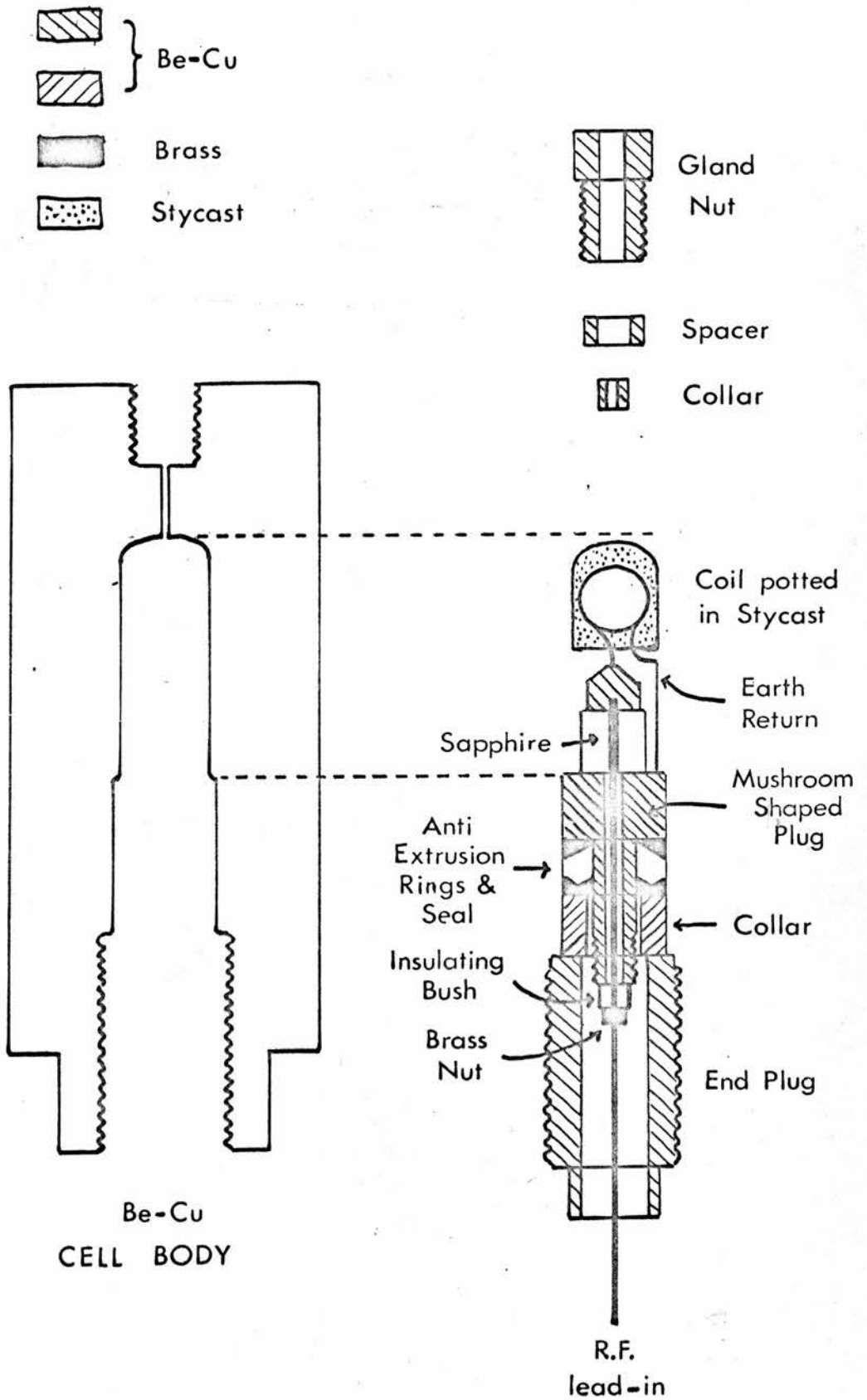


FIG 4.6b

FIG 4.7 The High Pressure Cell



The bore of the cell was radiused and hand polished to avoid stress-concentration points. The electrical lead-through and access to the pressure chamber were provided by the bottom plug. The Teflon gasket with the two brass anti-extrusion rings are pushed onto the stem of the mushroom shaped plug, and the collar pushed over the top. This plug is pushed into the cell body until it rests against the rim at the bottom of the high pressure chamber. When the end plug is screwed down on the collar, the Teflon is extruded to form a seal. This type of seal uses Bridgman's unsupported area principle⁵⁶. The force produced by the gas pressure P_o in the cell acting on the surface area of the mushroom shaped plug A_o is balanced by a force $P_1 A_1$ acting on the collar area A_1 . The pressure P_1 is transmitted to the gasket where

$$P_1 = \frac{A_o}{A_1} P_o \quad (4.6)$$

A_o is larger than A_1 by the area of the stem of the mushroom shaped plug which is the unsupported area. Hence the pressure in the Teflon is greater than P_o , and so the gas pressure does not leak past the gasket.

To remove the plug, an extractor has to be used. The extractor is a hollow cylinder with a thread cut on both the inside and outside surfaces. The inner thread is screwed onto the end of the mushroom shaped plug. A plate is fitted over the extractor to abut onto the end of the cell body. By screwing a nut down the outside thread of the extractor against the plate, the plug may be pulled out of the cell.

The electrical lead-through fits onto the mushroom shaped plug. The conical plug is insulated from the rest of the cell by the sapphire which has both ends highly polished. If the ends of the conical and mushroom shaped plugs are also highly polished, it should

be possible to achieve a seal by simply pressing the sapphire onto them. Our experience is that Aluminium foil washers, lightly smeared with vacuum grease, have to be placed on either end of the sapphire, and the whole assembly squeezed in a press. Care must be taken at this stage or the sapphire may shatter. This method produces a good seal at atmospheric pressure which is only improved by pressure. The conical plug is connected to the outside world by a 16 BA brass screwed rod which passes through holes in the sapphire and mushroom shaped plug and through an insulating nylon bush on the end of the mushroom shaped plug. A 16 BA nut screwed down the rod against the bush holds the sapphire seals firm, and does provide some degree of preloading. The rod is insulated by plastic sleeving. This type of lead-through was used in preference to the more common cone type⁸³, because it seemed easier to machine, and suffered less from electrical breakdown problems.

The NMR coil is soldered onto the conical plug with the earth return going to a pin on the mushroom shaped plug. The coil is potted in Emerson and Cuming Stycast 1266 which has stood up well to the pressure. The containers for the powdered samples were also made from Stycast, with a hole in the lid covered with nylon mesh, to allow Helium entry but prevent sample exit.

The maximum pressure that the cell can withstand is determined by the burst pressure of the body, and also by failure of the bottom plug. The former we have seen to be 11.8 KBar, while the latter is determined by either the sealing gasket pinching off the stem of the mushroom shaped plug, or the threads on the end plug being sheared off. Bridgman⁵⁶ has given a rule of thumb guide for pinch off, in that it may occur when the pressure equals the tensile strength of the material. The pressure in the gasket is $\approx 1.2 P_0$ from (4.6) and so the gas pressure may be ≈ 10 KBar. The end plug may withstand a pressure⁸²

$$P_e = \frac{DL}{2d^2} \sigma_y \quad (4.7)$$

where D is the thread diameter, d the seal diameter and L the thread length. For our cell $P_e \approx 12$ KBar.

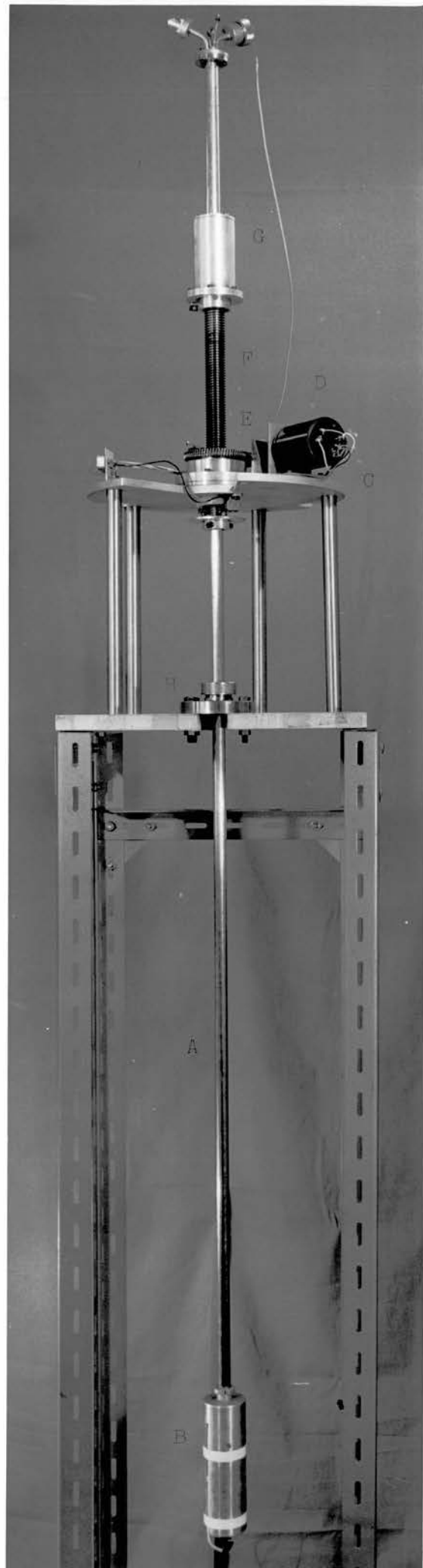
The cell was tested at room temperature by cycling the pressure six times from atmospheric to 7 KBar, the maximum attainable pressure. Although for full autofrettage about 9 KBar is required, (equation (4.3)) some had occurred since the bore changed diameter slightly. Hence taking into account all the pressure limits set above, the cell should be able to withstand pressures up to 10 KBar, which provides a safety factor of two for the pressures used in this work.

4.5 Helium Solidification

We have followed Schirber's method⁷² of pressurising with the cell above the solidification temperature T_s , and then gradually lowering the cell towards the liquid Helium level in the cryostat, keeping the pressure constant all the time. Theoretically, pressure could be applied just above T_s , but we have found that the cell leaked unless its temperature at pressurisation is greater than 180 K. This is attributed to a phase transition occurring in the Teflon seal about 160 K, below which the Teflon is not so compressible.

The remote control mechanism to drive the cell the 150 cm from the cryostat top into the magnet is shown in Plate 1. The 2M pressure tubing and the NMR and thermocouple leads were fed to the cell inside a 16 mm dia. stainless steel tube A. An Aluminium can B was fitted round the cell and clamped onto the bottom of this tube. This can ensured mechanical rigidity of the cell on the tube, and also would provide some shielding in the event of cell failure. A slot was cut down one side of the can to take the NMR lead to the plug in the cell bottom. The drive mechanism was mounted on a plate C,

PLATE 1



seated on pillars above the cryostat. A variable speed stepper motor D drove a rotating nut E, through which a screwed tube F was driven up or down. Mechanically operated micro-switches stopped the stepper motor whenever the screwed tube reached the end of its travel. A compressed air driven clutch G, attached to the screwed tube, could clamp onto tube A, hence driving the cell up or down. Tube A was led into the cryostat through the seal H, which consisted of two GACO U gaskets mounted back to back.

The lowering operation consisted of compressing the clutch and driving the screwed tube down to the bottom of its travel, thus pulling tube A and the cell with it. The clutch was then released and the screwed tube driven back up to the top and the operation repeated. The drive length of each operation was about 25 cm so six such steps were required to drive the cell down into the magnet. The cell was raised by reversing the procedure. The drive could be varied between 2 cm/hour and 300 cm/hour.

In Fig. 4.8 we tabulate the pressure at 4.2 K with the pressure required at T_s to produce this as calculated from Fig. 4.2. T_s is also tabulated as derived from the relationship of Mills and Grilly⁸⁴

$$P_s + 17.8 = 17.315 T_s^{1.5554} \quad (4.8)$$

where P_s is the solidification pressure in Bars. The cell temperature was monitored by two gold/iron vs. chromel thermocouples anchored to the top and bottom of the cell. A temperature gradient of about 2 K was observed over the length of the cell, presumably caused by heating from thermal conduction and radiation from above, and cooling from Helium evaporation from below. Schirber⁷² has given a rate of 2.5 cm/hour for solid Helium growth over the sample but points out that for experiments less sensitive to deviations from hydrostaticity, growth can be quicker. Typical rates in our experi-

ments were 5 to 10 cm/hour.

We have measured the pressure in the cell produced by solid Helium by placing a coil of Manganin wire inside it. Manganin has a negligible temperature coefficient of resistance at room temperature, but a reasonably large pressure coefficient⁵⁶ of $2.4 \times 10^{-3} \text{ K Bar}^{-1}$. About 3 m of Manganin wire were wound on a former, giving a resistance of about 111 Ω . The coil was seasoned by heat treating to 140°C for 10 hours and placed in the cell. Pressurisation at room temperature gave a value for the pressure coefficient of resistance of $(2.45 \pm 0.05) \times 10^{-3} \text{ K Bar}^{-1}$. At low temperature, the temperature coefficient of Manganin is not negligible and some sort of temperature correction must be made. The cell was cooled at atmospheric pressure and the resistance measured giving curve A in Fig. 4.9. The cell was warmed again and taken through a 3 KBar pressurisation giving curve B. Subtraction of the two curves should show up any change in pressure (Curve C). A slight bump, representing an excess pressure of ≈ 400 Bars, appears around the solidification temperature of 28 K. We cannot explain this bump except that it may indicate some deviation from hydrostaticity. Below T_s , the pressure is the same as above, and possibly shows the drop predicted by Fig. 4.2. This experiment shows that the average pressure is the same on both sides of T_s , but gives no information on the hydrostaticity.

4.6 Safety Aspects

The danger in a high pressure gas system such as ours, arises should any part of the system fail, and the stored energy of the compressed gas imparts a large velocity to any fragment produced. The stored energy in an isentropic compression of a gas may be written as

Fig 4.8 Helium Solidification

Pressure at 4.2 K Bar	Pressure at T_s K Bar	Solidification Temperature T_s °K
0.5	0.508	8.9
1.0	1.020	13.9
1.5	1.551	18.1
2.0	2.075	21.8
2.5	2.613	25.3
3.0	3.151	28.5
3.5	3.690	31.5
4.0	4.226	34.4
4.5	4.771	37.1
5.0	5.316	39.8
5.5	5.867	42.4
6.0	6.412	44.9

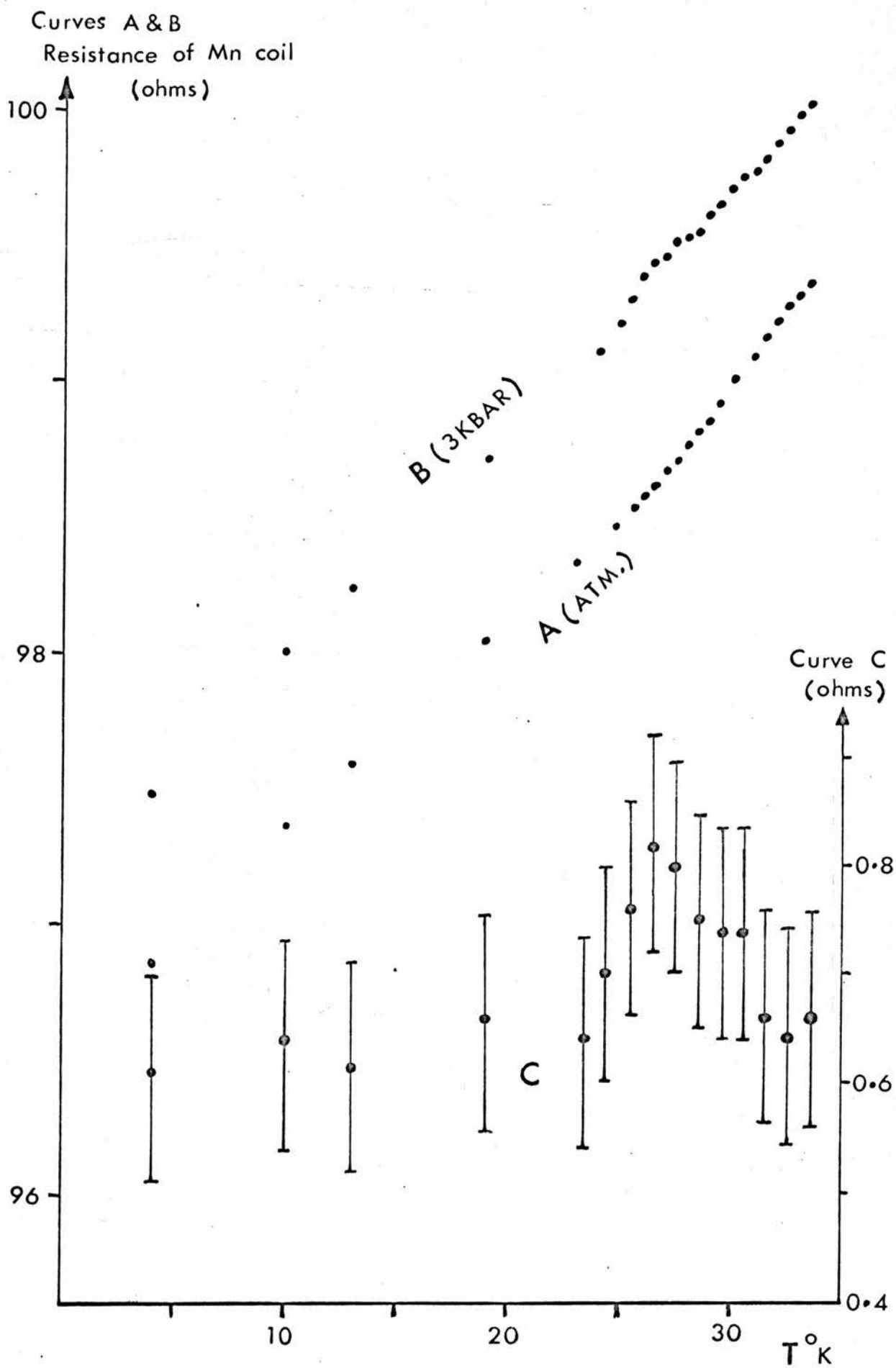


FIG 4.9 Test of Helium Solidification

$$E = \frac{1}{\gamma-1} [(PV)_{\text{initial}} - (PV)_{\text{final}}] \quad (4.9)$$

For our system at 5 KBar this gives an energy of 9 KJoules which is clearly an overestimate, since at high pressure, Helium behaves more like a liquid than a gas. In the worst case, if a plug or end section is blown out, 60% of the stored energy is transmitted into fragment K.E. and the rest is dissipated in a shock wave. For a typical 20 g plug, its velocity v can be calculated from

$$\frac{1}{2} mv^2 = 0.6 E \quad (4.10)$$

to be about 700 m/s, and its penetration depth t calculated from⁸²

$$m^{1/3} v = Kt \quad (4.11)$$

where $K = 2.6 \times 10^4$ for a mild steel plate. This produces a penetration of about 7 mm into mild steel.

A box of $\frac{1}{4}$ inch thick steel has been constructed round the pressure generating system as shown in Plate 2. Around the bottom of the box where the pumps and intensifier are situated, sandbags have been built up to provide further protection. Above the level of the sandbags, Lexan transparent sheeting has been bolted over the front, providing extra protection, and enabling reading of the gauges. This sheeting is very tough, and is virtually "bullet proof".

The NMR pressure cell is connected to the pressure generating system by about six feet of flexible tubing led out of the top of the box. Because of the danger from "whipping", should an end of this tube blow off, it was encased in thick rubber hose, which had both ends clamped in position. This tubing effectively decouples the cell from the rest of the system, since its narrow bore prevents rapid gas flow. Hence the cell sees only its own volume in the event of failure, and since this is less than 1 cm³, the cell is relatively

safe. Nevertheless the cryostat is surrounded by Lexan screens which are fixed in place during pressurisation, as shown in Plate 3.

A possible hazard in some systems arises if the cell warms up under pressure. The pressure will rise, and may reach the burst pressure of the cell. In our system, the large volume in the Heise gauge acts as a pressure sink for such an effect. Calculation and experiment both show that a cell at 4.2 K and 5 KBar will only produce 6 KBar at room temperature.

Finally we discuss a method of leak detection which may be performed with the operator in a safe position. The Harwood tubing fittings and valves all have blow-holes, so that in the event of leakage past the seal, the gas will not blow the thread off the plug. It is at the tubing fittings and valves that leaks will occur. One end of a plastic tube was stuck over each blow-hole with Plasticine, while the other ends of the tubes were led outside the box. Detection was carried out by placing a BOC gas sniffer over the end of each tube in turn. By this method, leaks could be detected which only became visible by a drop in the Heise gauge after a few hours.





Control panel with two large circular gauges and several control knobs. A label "TRONIC" is visible on the right side.

Mechanical assembly featuring a central motor, various pipes, and a vertical rod with a piston-like component. The assembly is supported by a wooden frame.

Rack-mounted electronic equipment. The central unit is labeled "TRONIC MODEL 8010 POWER SUPPLY". To its right is a "Heater Input" section and another "TRONIC MODEL 8010" control unit with a digital display and various knobs.

CHAPTER 5

REVIEW OF EXPERIMENTAL DATA ON THE BRONZES5.1 Introduction

Sodium Tungsten Bronze, Na_xWO_3 , is so called because at high Sodium concentration x , it resembles bronze in appearance. It belongs to the family of Tungsten Bronzes, A_xWO_3 , where A is usually an alkali metal. The bronzes can exist in many crystal structures, but in this review we shall concentrate on the cubic phase which has the same structure as Perovskite, CaTiO_3 .

5.2 Crystal Structure

In the cubic phase, Na_xWO_3 has the perovskite structure shown in Fig. 5.1a. It should be noted that there is another equivalent unit cell consisting of the W atom at the cube body centre, Na atoms at a fraction x of the corners, and O atoms at the face centres. The phase diagram of Ribnick et al⁸⁵ (Fig. 5.2) shows that the cubic phase is stable for $x > 0.4$. Lightsey⁸⁶ has shown however that this phase is stable to lower x , and that it is possible to obtain crystals in a metastable cubic phase down to $x \approx 0.2$. The lattice constant for the cubic phase varies with x according to⁸⁷

$$a = (3.7845 + 0.0820x) \text{ \AA} \quad (5.1)$$

Hence x ray measurements provide a useful method of determining the x value.

There is evidence in many perovskites, ABO_3 , that the Oxygen atoms are displaced from their normal positions. This is best described⁸⁸ by constructing Oxygen octahedra around each B site as in Fig. 5.1b. Displacements are then treated as distortions or tilts of these octahedra⁸⁹. For example the low temperature phase

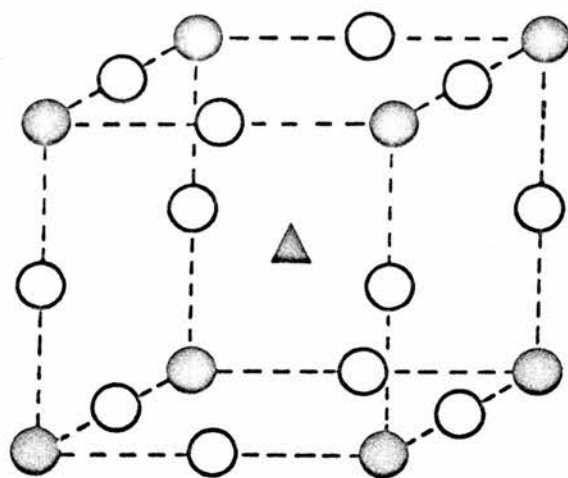


FIG 5.1a

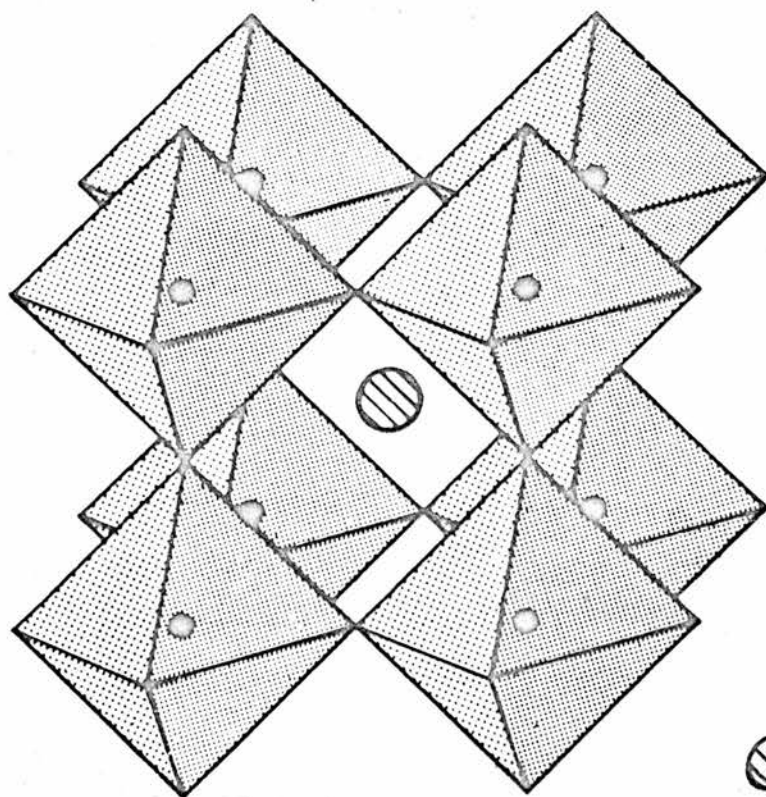
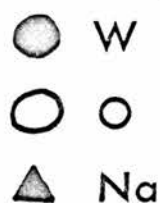


FIG 5.1b

Oxygen Octahedra



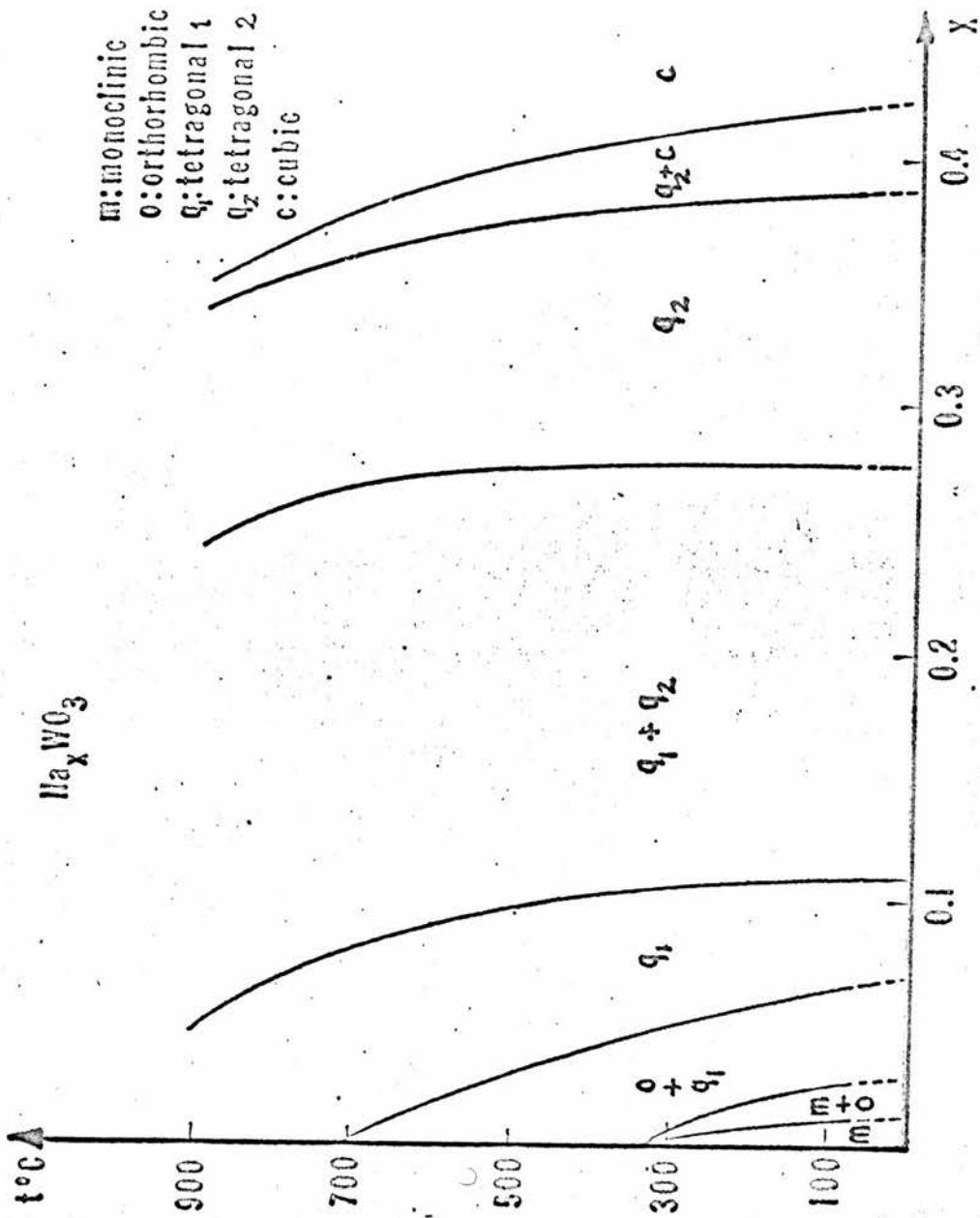


Figure 5-2 Phase diagram of Na_xWO_3

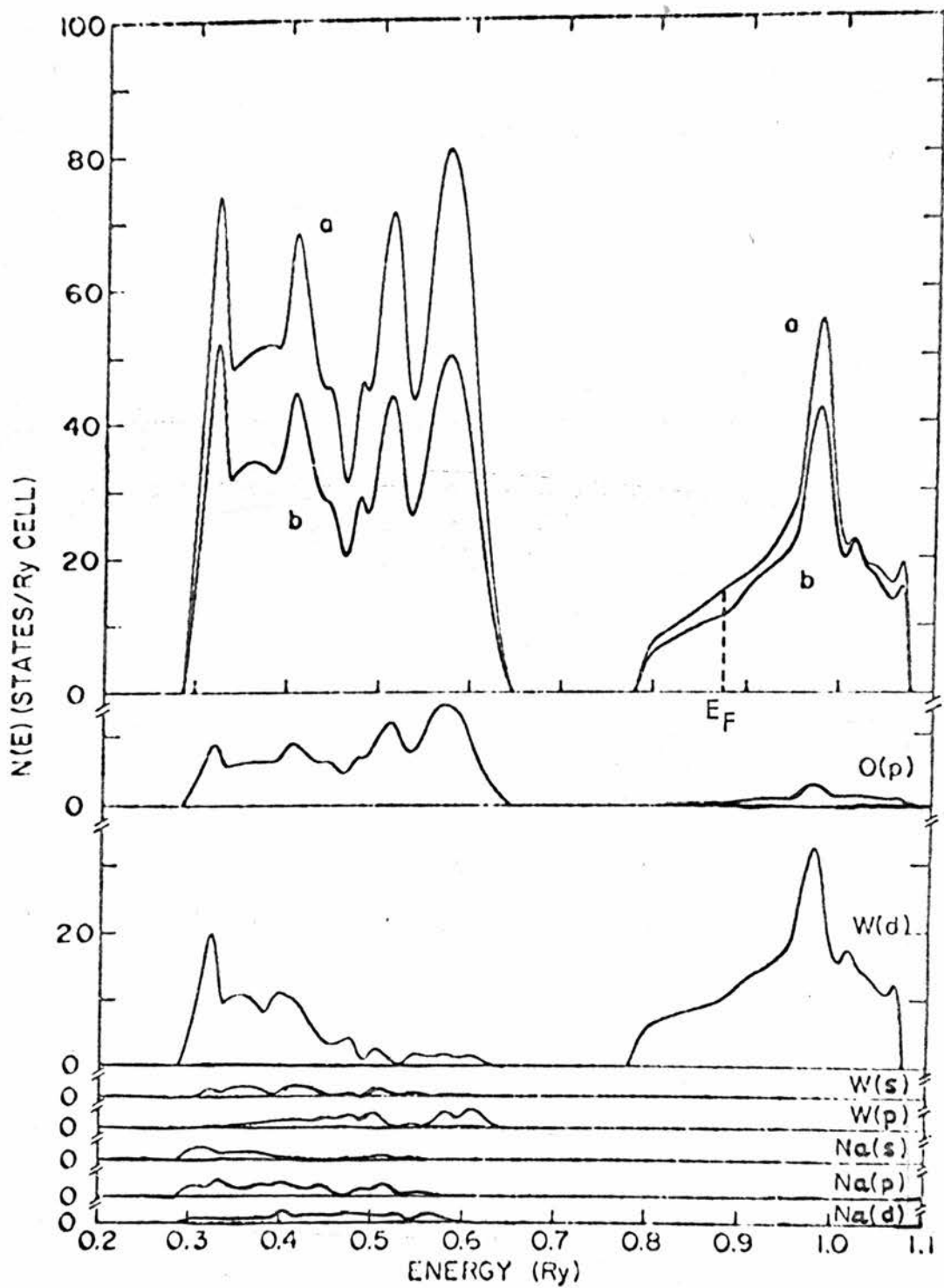


FIG 5-3 Band Structure of NaWO₃

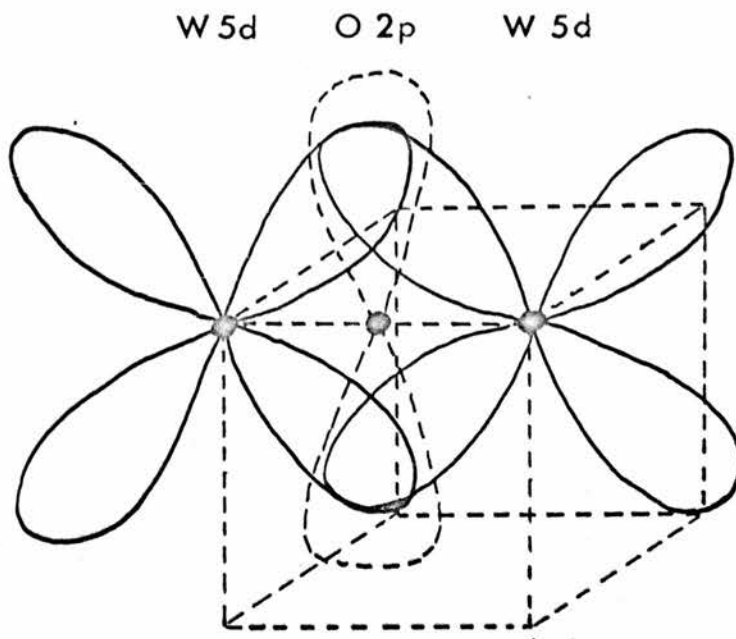


FIG 5.4a Planar Character of the Orbitals

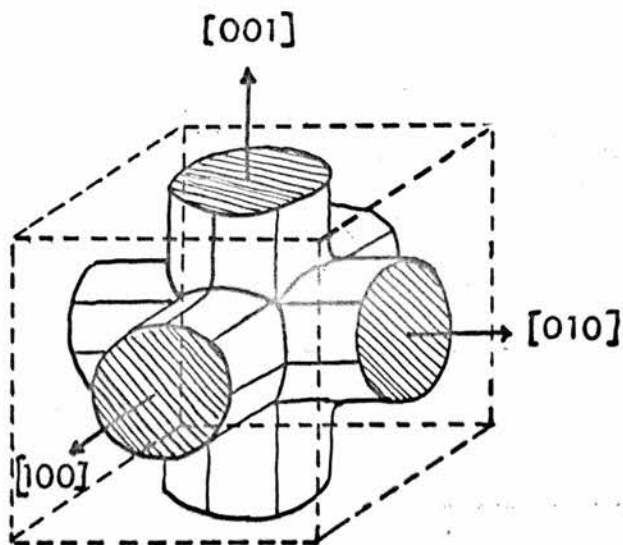


FIG 5.4b The Fermi Surface

of SrTiO_3 consists of octahedra tilted about the 001 axis, so that the Oxygen atoms are displaced towards the body-centred positions⁹⁰. Displacements are also found in the Tungsten Bronzes. X ray work⁹¹ on H_xWO_3 shows a doubling of the unit cell due to opposite tilts of neighbouring octahedra, the Tungsten atoms retaining cubic symmetry. In Na_xWO_3 , no displacements have been found by x ray work, but neutron diffraction⁹², birefringence⁹³ and NMR data^{94,95} all point to small displacements which may be unobservable by x rays.

5.3 The Conduction Band and the Fermi Surface

There have been five models to explain the conduction band in Na_xWO_3 . Keller⁹⁶ proposed a band of W 6s states, but this was rejected when the large negative W Knight shift was discovered, as was the Mackintosh model⁹⁷ of Na 3p states. Sienko⁹⁸ proposed a band of W 5d states which Goodenough⁹⁹ modified to include W 5d and O 2p hybridisation. Finally Fuchs¹⁰⁰ assumed that the conduction electrons avoid vacant Na sites, and hence reduced the problem to one of percolation.

The similarity between the transport properties of Na_xWO_3 and ReO_3 , for which band structure calculations¹⁰¹ show a 5d (t_{2g}) conduction band populated by one electron from each Re atom, led to the proposal that the conduction band of Na_xWO_3 might also be of 5d character, populated by electrons donated by the Sodium. A similar type of band structure calculation¹⁰² on the molybdenum bronze $\text{K}_{0.92}\text{MoO}_3$ also supported this model as did a recent band structure calculation on NaWO_3 ¹⁰³. The calculated density of states for NaWO_3 is shown in Fig. 5.3, where the bottom curves are the orbital densities of states, curve b is their sum, and curve a is the total density of states. It shows a conduction band made up of Tungsten 5d (t_{2g}) states with a small admixture of Oxygen 2p, and with a bandwidth of about 4 eV. X ray photoemission spectra¹⁰⁴ also show

a 5d conduction band for Na_xWO_3 with the area of the peak increasing as x increases, thus demonstrating the filling of the conduction band with electrons donated by the Sodium. As we shall see in section 5.8, this model also explains the NMR data.

Hence as each Sodium atom enters the lattice, it donates its 3s valence electron into a conduction band formed from W 5d (t_{2g}) and O 2p orbitals.

The immediate consequence of this choice of orbitals is that the electrons tend to concentrate in the cube faces as shown in Fig. 5.4a. This planar character of the orbitals occurs in many d band perovskites such as SrTiO_3 , BaTiO_3 and KTaO_3 . It produces the Fermi surface shown in Fig. 5.4b, where the main feature is the three intersecting cylinders, although there is evidence for two roughly spherical electron pockets at the centre of the Brillouin zone. Hence Wolfram¹⁰⁵ points out that conduction is two dimensional, in the sense that the energy depends on only two components of the wavevector. Wolfram also shows that this will lead to discontinuities in the density of states at the band edges, and to a logarithmic singularity in the band interior. Examination of Fig. 5.3 shows both these effects are probably present, although are smeared over by other interactions.

A study of the Kohn effect¹⁰⁶ has been made for $0.56 < x < 0.83$. When a single phonon wavevector q can span the Fermi surface i.e. when $q = 2k_F$, then a discontinuity arises in the phonon dispersion curve. A plot of q at the discontinuity in different directions maps out the Fermi surface. This study also shows the intersecting cylinders whose radii decrease with decreasing x , suggesting electrons being removed from the band.

Finally we introduce a model for the density of states proposed by Wolfram¹⁰⁵ and developed by Tunstall⁹⁵. From the band structure calculations, it seems reasonable to fit $N(E)$ over the range of x of interest by

$$N(E) = A e^{E/E'} \quad (5.2)$$

where A and E' are constants depending on the exact shape of the band. If x electrons fill up the band to the Fermi level E_F then

$$x = \int_0^{E_F} N(E) dE \quad (5.3)$$

performing the integration one obtains

$$N(E_F) = \frac{x}{E'} + A \quad (5.4)$$

This linear relationship of $N(E_F)$ with x is at variance with free electron theory which predicts $N(E_F) \propto x^{1/3}$.

5.4 Transport Data

Much of the early work on conductivity in Na_xWO_3 is dubious, either because of sample impurity or sample inhomogeneity. Brown and Banks¹⁰⁷ (1951) and Gardner and Danielson¹⁰⁸ (1954) found a resistivity minimum around $x = 0.7$, but Ellerbeck¹⁰⁹ (1961) could find no minimum with better crystal homogeneity. With very homogeneous crystals, Muhlestein and Danielson¹¹⁰ (1967) found a minimum in the resistivity slope at $x = 0.75$, but no minimum in the resistivity itself. This they ascribed to Sodium ordering, as described by Atoji and Rundle⁹², where at $x = 0.75$ the unit cell is octupled in volume and the two Sodium sites on one of the new cube's body diagonals are vacant. These results and others^{111,112} are shown in Fig. 5.5 as a function of x and in Fig. 5.6 as a function of temperature.

The resistivity data may be summarised as follows. At high x , Na_xWO_3 is a good metallic conductor, with a room temperature resistivity six times that of copper. The resistivity decreases with decreasing temperature with a large residual resistivity due to scattering from Sodium vacancies. As x decreases, the resistivity

increases, and the temperature dependence flattens, until at $x = 0.25$, $\sigma(1.3 \text{ K}) \approx \sigma(300 \text{ K})$. For $0.2 < x < 0.25$ the resistivity increases as the temperature decreases, which suggests thermal activation of some of the carriers. Below $x \approx 0.2$ it is impossible to obtain cubic crystals, but measurements on non-cubic samples show a semiconducting type of behaviour.

The Hall data^{86,110} of Fig. 5.7 shows that one conduction electron is being donated by each Sodium atom. Once again there is evidence of some thermal activation at low x and also the suggestion of an anomaly at $x = 0.75$.

5.5 Electronic Specific Heat and Magnetic Susceptibility

In a metal, the specific heat is usually written as

$$C = \gamma T + \beta T^3 \quad (5.5)$$

where γ is associated with the conduction electrons and β with the lattice. Measured values of γ are shown in Fig. 5.8^{113,114}. It can be shown that if exchange and correlation are neglected, then

$$\gamma = \frac{1}{3} \pi^2 k_B^2 \rho(E_F) \quad (5.6)$$

Zumsteg¹¹⁴ points out that the free electron prediction of $\rho(E_F) \propto x^{1/3}$ as shown by the solid line in Fig. 5.8, does not fit the data well. Instead a much better fit is obtained by using $\rho(E_F) \propto x$, the dependence referred to in section 5.3.

The electronic magnetic susceptibility^{114,115} is shown in Fig. 5.9. In the nearly free electron model

$$\chi_e = \mu_B^2 \rho(E_F) \left[1 - \frac{m^2}{3m^{*2}} \right] \quad (5.7)$$

where μ_B is the Bohr magneton and m^* is the electronic effective mass.

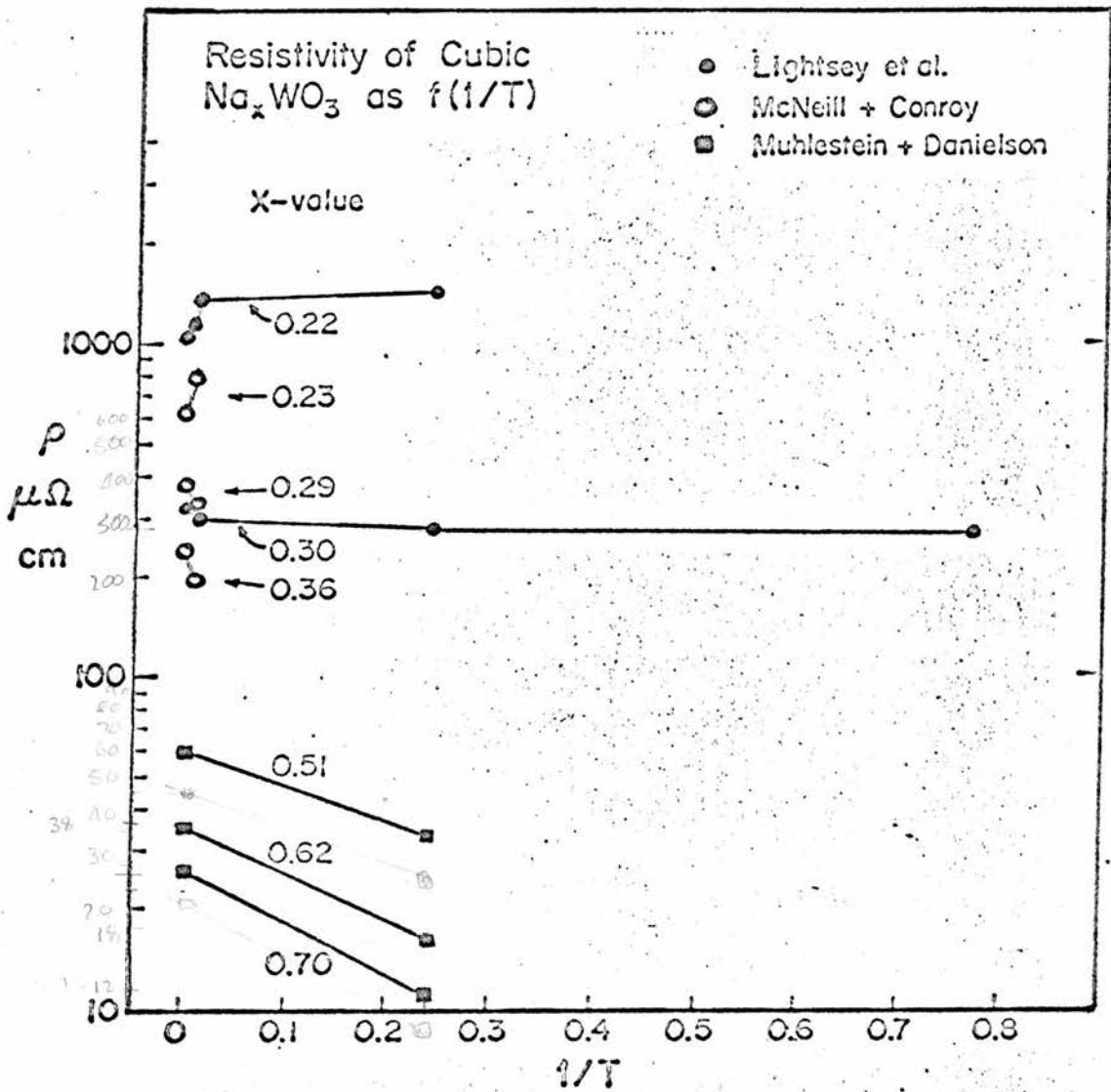


Figure 5-6 Temperature dependence of Na_xWO_3 resistivity

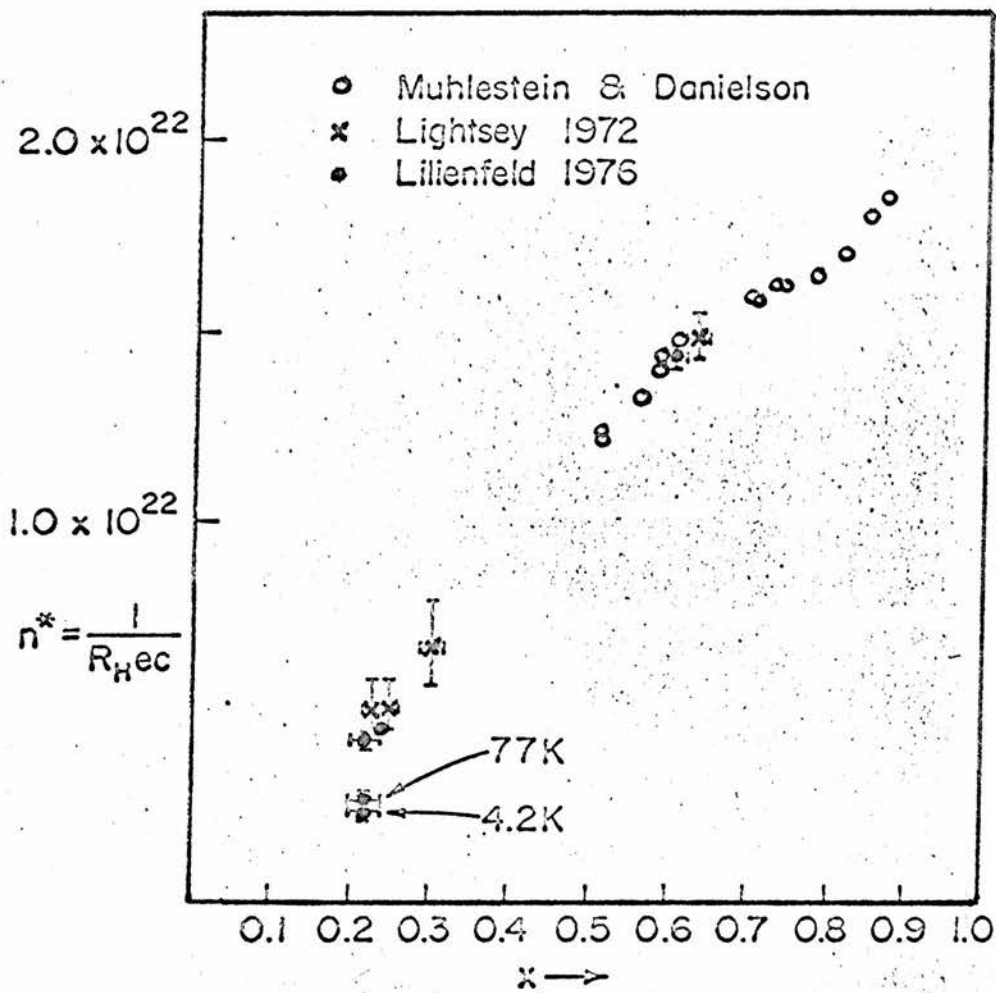


Figure 5-7 Number of Hall carriers for Na_xWO_3

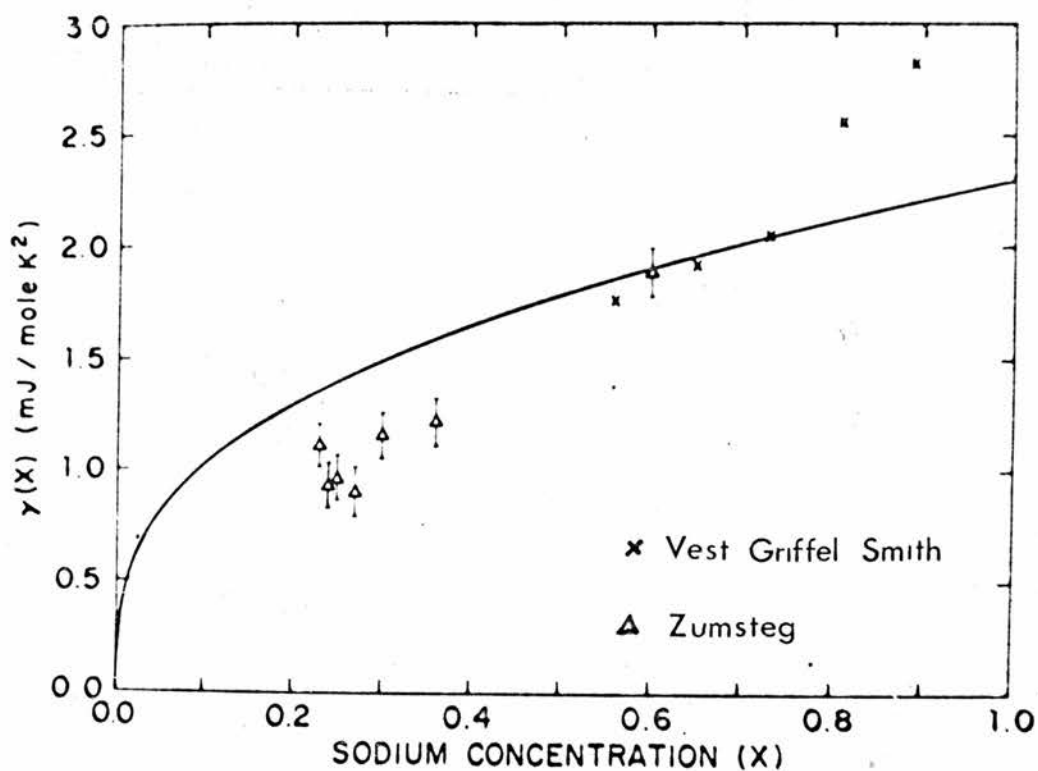


FIG 5-8 Specific Heat

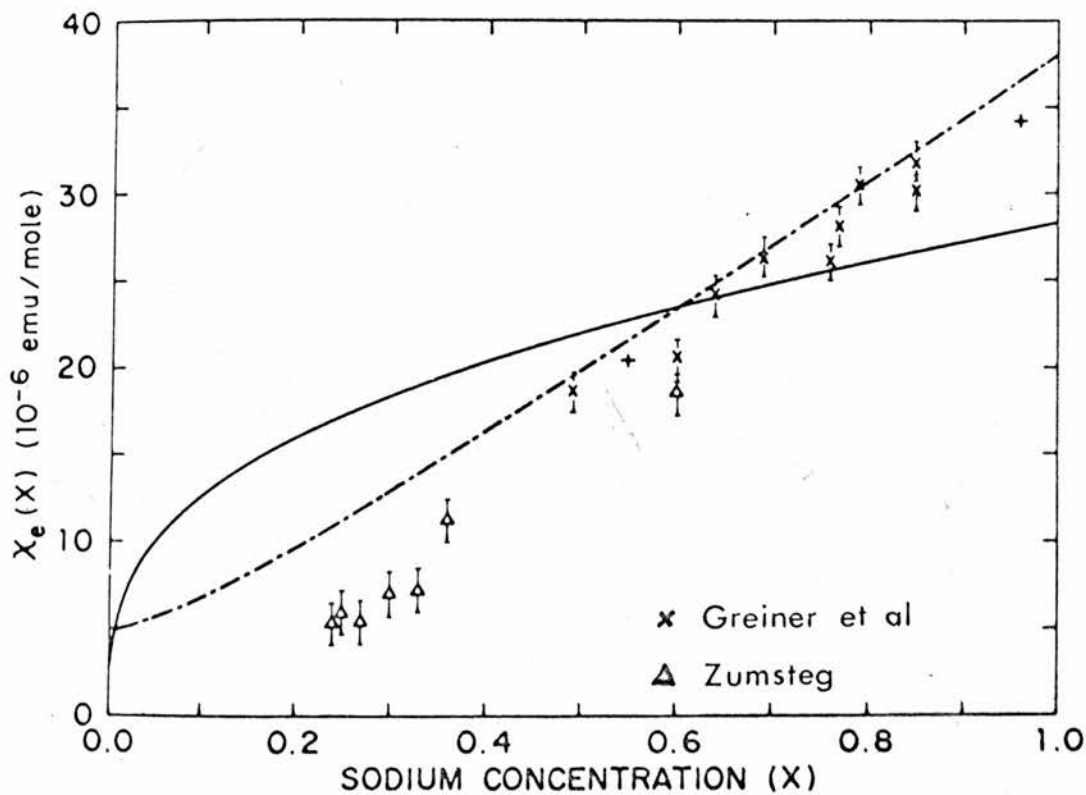


FIG 5-9 Magnetic Susceptibility

The second term in brackets is the correction for the diamagnetic susceptibility.

Greiner et al¹¹⁵ show that the best fit to the data with a free electron density of states gives $m^* = 1.6 m$, but that this is a very poor fit as shown by the full line in Fig. 5.9. However they show that if $\rho(E_F)$ is calculated from the specific heat data rather than from free electron theory, then a much better fit is obtained.

Zumsteg¹¹⁴ shows that the better fit obtained by using the specific heat data can be explained if the density of states used in both specific heat and susceptibility values is proportional to x . The assumption that $\rho(E_F) \propto x$ leads to the dotted line in Fig. 5.9.

In conclusion, both γ and χ_e suggest that $\rho(E_F) \propto x$. This result is at variance with the free electron model, but can be explained by an exponential bandshape.

5.6 Thermal Properties

Measurements of the coefficient of thermal expansion¹¹⁶ in Na_xWO_3 in the range $0.3 < x < 0.84$ and between room temperature and 900 K, show that below about 500 K, all samples have approximately the same value of $12 \times 10^{-6} \text{K}^{-1}$. However at a certain temperature, which depends on x , the coefficient changes sharply and reversibly to the lower value of $5 \times 10^{-6} \text{K}^{-1}$. The transition temperature as a function of x is shown in Fig. 5.10 and exhibits a broad minimum around $x = 0.5$.

Shanks and Redin¹¹⁷ have measured the thermal conductivity in this temperature range, and find a discontinuity at the same temperature as the transition in the thermal expansion data. Complete agreement of the two sets of data is not possible, since as shown in Fig. 5.10, only two samples were studied for the thermal conductivity data. Shanks and Redin propose a structural transition involving the

Oxygen atoms, since the constancy of the x ray data through the transition rules out ~~and~~ ^{any} Tungsten displacement, and the absence of any effect in Ellerbeck's transport data¹⁰⁹ probably implies that the Sodium is not involved.

There is also evidence in another work¹¹⁸ of an anomaly in the thermal conductivity for $x \approx 0.75$, which is ascribed to a similar process to that causing the anomaly in the transport data.

5.7 Optical Properties

In appearance, Na_xWO_3 is a yellowish metallic looking crystal for $x \approx 0.8$, darkening to red for $x \approx 0.6$ and then to a dark metallic blue for $x \approx 0.3$. Below $x = 0.2$, the metallic lustre disappears, and the crystals become pale yellow, similar to WO_3 .

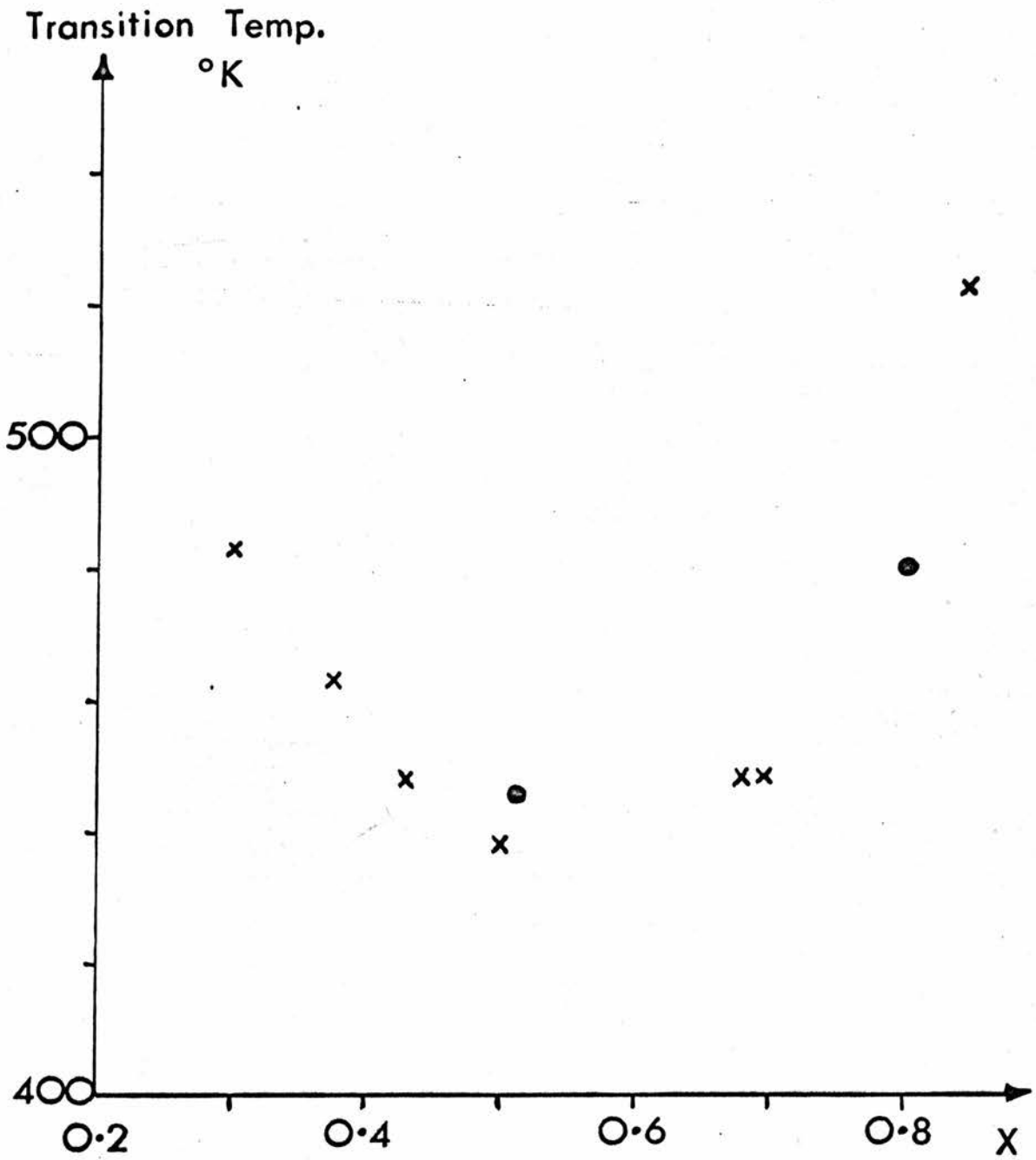
The absorption coefficient has been measured by Brown and Banks¹¹⁹ as shown in Fig. 5.11, and is usually explained in terms of plasma modes¹²⁰. The absorption spectra can be divided into three regions. Region 1 with a low absorption coefficient is typical of free carrier absorption. Region 2 shows a peak due to the excitation of plasma modes. This should occur at the plasma frequency ω_p , which for a free electron gas is given by

$$\omega_p = \left(\frac{4\pi n e^2}{m^*} \right)^{\frac{1}{2}} \quad (5.8)$$

Region 3 shows a drop in absorption. In this region, any structure present is due to interband transitions.

For the bronzes, $n = x/a^3$ and hence as x increases, the absorption peak moves to higher energies, producing the observed colour variation with x . Lightsey⁸⁶ has compared the measured ω_p with that determined from equation (5.8) and obtains reasonable agreement with $m^* = 3.8 m$. A value of m^* more in keeping with that obtained from the susceptibility if the free electron type equation (5.8) was replaced by one

FIG. 5-10



x Thermal Expansion

• Thermal Conductivity

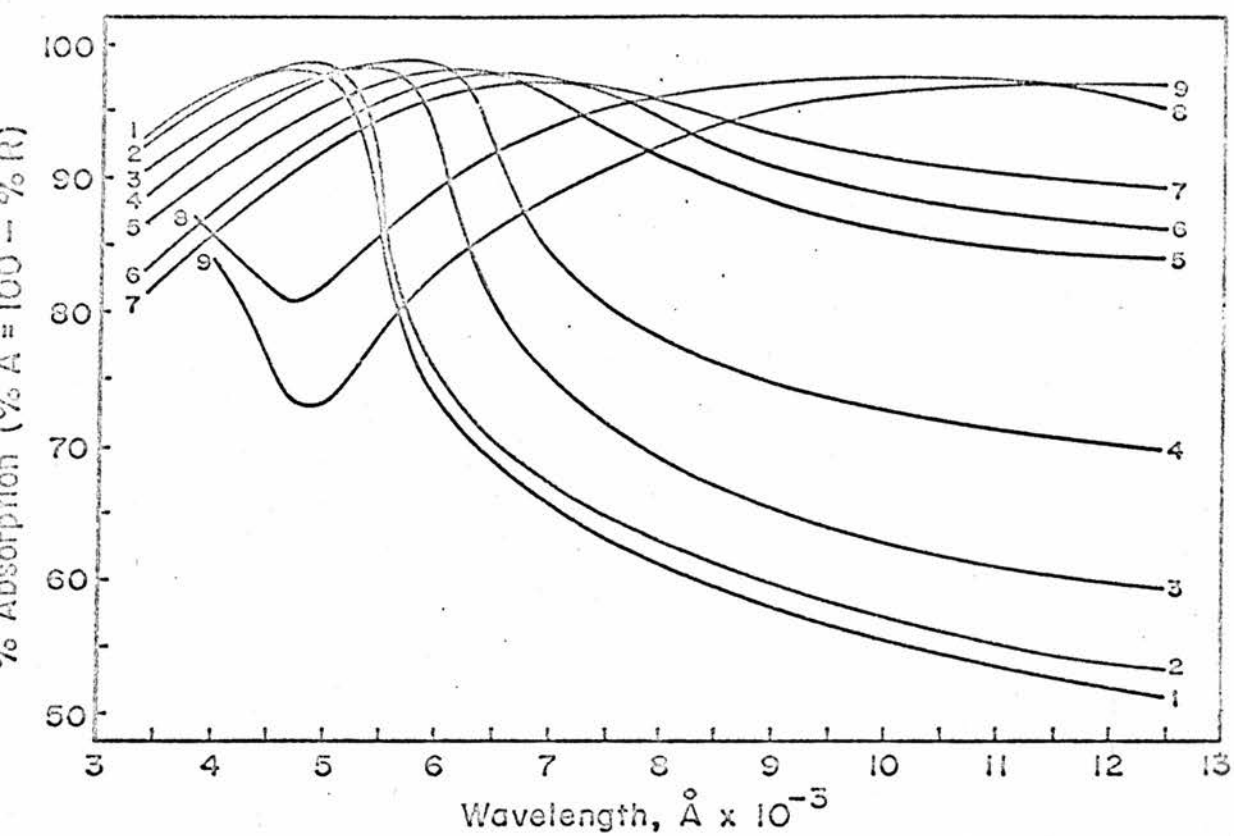


Figure 5.11 Absorption spectra of Na_xWO_3 : 1. $x = 0.85$;
 2. $x = 0.75$; 3. $x = 0.60$; 4. $x = 0.50$; 5. $x = 0.40$;
 6. $x = 0.30$; 7. $x = 0.20$; 8. $x = 0.15$ (nom., WO_3
 struct.); 9. $x = 0.10$ (nom., WO_3 struct.).

more suitable to the exponential bandshape.

The lack of a plasma peak for $x = 0.10, 0.15$ in Fig. 5.11 is taken as evidence that the system is non-conducting for $x < 0.2$. Plasma oscillations are also evident in electroreflectance spectra¹²¹, giving a peak which moves to higher energy as x increases. However the effective mass deduced from this work is much lower, giving $m^* \approx m$.

5.8 Nuclear Magnetic Resonance Studies

In this section we shall present a chronologically ordered review of the seven previous NMR investigations of Na_xWO_3 . Two nuclei, Na^{23} (spin $3/2$, natural abundance 100%) and W^{183} (spin $1/2$, natural abundance 14%) have been studied. The O^{17} resonance (spin $5/2$, natural abundance 0.04%) has not yet been detected, not because of receiver sensitivity, but probably because the line is smeared by quadrupole effects due to the non-cubic environment around the Oxygen sites. The first four studies used the same samples, with the emphasis on studying the conduction band. The fifth study, on purer samples, probed the high temperature phase transition. The last two studies extended the sample range to lower x , and cleared up some anomalies in the previous investigations.

1. Jones, Garbaty and Barnes¹²² (1962) Na Resonance

This preliminary CW room temperature study of seven samples $0.56 < x < 0.89$ showed that the Na Knight Shift was negative and very small, and increased from -56 ppm ($x = 0.56$) to -69 ppm ($x = 0.75$) and then fell to -22 ppm ($x = 0.89$). At 77 K the shifts were slightly smaller. This implied that the conduction band consisted of W 5d or W 6s orbitals, both of which have zero density at the Sodium nucleus. The linewidths agreed with those calculated from the Van Vleck theory, hence indicating that the main broadening

mechanism was the dipolar interaction between Sodium nuclei.

2. Narath and Wallace¹²³ (1962) W Resonance

This was another CW room temperature investigation on the same samples as 1, but observing the Tungsten resonance. The Knight Shifts were found to be negative and much larger than the Sodium shifts, increasing from -1590 ppm ($x = 0.56$) to -2010 ppm ($x = 0.89$). This suggested that the conduction band consisted of W 5d orbitals which produced the negative shifts by a core polarisation mechanism. The linewidths were found to be ≈ 5 mT, which are much greater than the calculated dipolar width.

3. Fromhold and Narath¹²⁴ (1964) Na Resonance

In this study, pulsed NMR was used to measure T_1 . The first major development occurred when a two pulse "spin echo" sequence was used. After the first pulse, a free induction decay (FID) was observed with a decay time $T_2^* \approx 300 \mu\text{s}$. However after the second pulse, a narrow echo was found with $T_2^* \approx 40 \mu\text{s}$. Since the T_2 of the echo was between 700 μs and 1400 μs , it was suggested that the echo was due to static second order quadrupole broadening of the central transition. Hence it was assumed that the nuclei contributing to the Echo came from different sites in the sample to those contributing to the FID. We note that the previous CW work must only have detected the FID nuclei.

Fromhold and Narath calculated the electric field gradient at a Sodium site due to a single nearest neighbour Sodium vacancy, and found that it could produce the requisite broadening of the Echo. This implied that the FID nuclei arose from sites with all the nearest neighbour Sodium sites either all full, or all empty. For a random distribution of Sodium sites, the number of nuclei contributing to the FID should drop sharply as x was decreased. From Fig. 5.12 it can be seen that this did not occur, and so clustering of a fraction

of the Sodium atoms into local $x = 1$ regions. The FID was assumed to arise from nuclei in the clusters, and the Echo from nuclei randomly dispersed outside. The FID T_2 would be independent of x , whereas the Echo T_2 would increase as x decreased due to dilution. Both these T_2 dependences seemed to be followed by the experimental data.

T_1 measurements showed that above 77 K, $T_1 T = \text{constant}$, as expected from magnetic coupling to the conduction electrons. Below 77 K there was considerable evidence of relaxation due to paramagnetic impurities. It was also found that T_1 did not have a definite x dependence, which would be expected if clustering occurred. Finally, using T_1 and K values, the maximum amount of Na 3p character at the Fermi surface was estimated to be 33%, hence supporting the Sienko model of W 5d states.

4. Fromhold and Narath¹²⁵ (1966) W Resonance

In this work, pulse techniques were used to measure the Tungsten T_1 . The experiment is quite difficult, since the low abundance and sensitivity of the W^{183} nucleus necessitates high magnetic fields, low temperatures and signal averaging. The observed T_1 s were more than two orders of magnitude shorter than the Sodium T_1 and comparable with those of Tungsten metal. This supported the model of the conduction band composed of Tungsten orbitals. T_1 showed the T^{-1} dependence characteristic of magnetic relaxation via the conduction electrons. The experimental values of $T_1 T$ were smaller than those predicted by the Korringa relation from the known Knight shift. This was explained by a cancellation in K of the positive contact and orbital terms by the negative core polarisation. Since the total shift is negative, core polarisation is the dominant contribution.

The linewidths obtained were comparable to the Knight shifts, which led to the assumption that the large linewidths were due to

local variations of the Knight shift. Quadrupolar broadening was ruled out since W^{183} has spin $\frac{1}{2}$. The linewidth was broadest at low x , which agreed well with the proposal that the variation in electron density depended on the variation in the arrangement of the surrounding Sodium sites.

In summary, the four investigations discussed so far have indicated a conduction band consisting of W 5d orbitals. Also the T_2 values and the existence of two sites have indicated that Sodium clustering may occur. However the following investigations will question the values of T_1 and K because of the paramagnetic impurities, and will also question the conclusions concerning clustering.

5. Bonera et al⁹⁴ (1971) Na Resonance

This pulsed NMR investigation of the Sodium resonance between 100 K and 700 K presents evidence of a phase transition around 400 K, and also proposes a new model to explain the two Sodium sites. At 8 MHz, the Echo dephasing time was about a third of that at 24 MHz, which is in agreement with the frequency dependence of second order quadrupole broadening. Also it is shown that the Fromhold and Narath dephasing time of 40 μ s for the Echo, gives only the pulse spectral width, since they were not using large enough B_1 fields.

The authors also criticise the idea that the large electric field gradients responsible for the Echo are produced by nearest neighbour Sodium vacancies. They show that the conduction electron screening can reduce the field gradient produced by a vacancy by an order of magnitude. This reduction assumed a uniform electronic charge density, and it is proposed that the non-uniform 5d orbitals could reduce it even more. Hence it is proposed that the field gradients are caused by Oxygen displacement of the type mentioned in section 5.2. The FID nuclei are then surrounded by a cubic arrangement of nearest neighbour Oxygens, whereas the Echo nuclei are not.

As the temperature is increased, the Echo T_2^* increases, until at a certain temperature T_0 , it equals the FID T_2^* . At higher temperatures there is no further variation. This is ascribed to a phase transition from a low temperature distorted phase to a high temperature cubic phase and provides further evidence for field gradients caused by Oxygen displacement. The transition temperatures T_0 are approximately the same as those found for the anomaly in the thermal expansion and thermal conductivity, and show the same sort of x dependence, although complete agreement is not possible because the x range of the NMR data is above the minimum in T_0 found in the thermal expansion data. The spin lattice relaxation rates show a peak around T_0 which is explained by an enhancement of the quadrupole relaxation rate, or a slowing down of the magnetic fluctuations close to the phase transition.

The temperature dependence of the quadrupole coupling constant ν_Q could be fitted by a $(T_0 - T)^{\frac{1}{2}}$ law, implying that the field gradient is linear in the order parameter. This rules out a simple distortion such as those occurring in BaTiO_3 and LaAlO_3 where the field gradient is quadratic in the order parameter. This leads the authors to propose a more complex distortion such as that in NaNbO_3 , where two Sodium sites have also been observed¹²⁶. Borsa¹²⁷ has followed this proposal, and has developed a model of Oxygen octahedra rotated about the C-axis, with neighbouring octahedra along this axis rotated in the same direction. This model is discussed further in Chapter 7.

6. Tunstall⁹⁵ (1975) Na Resonance

This study extended the sample range down to $x = 0.22$, below which cubic structure could not be obtained. The region between $x = 0.22$ and 0.35 is of interest since it spans the conductivity values $300 \Omega^{-1} \text{cm}^{-1}$ and $3000 \Omega^{-1} \text{cm}^{-1}$, and hence may be the diffusive region referred to in Chapter 3.

Fig 5.12

Previous Intensity Data

Y and Y* as defined in equations (6.2) and (6.3)

	x value	Y	Y*
Fromhold and Narath	0.56	0.22	0.10
	0.73	0.29	0.14
	0.89	0.32	0.16
Bonera et al	0.517	0.25	0.12
	0.72	0.28	0.135
	0.855	0.22	0.10
Tunstall	0.22	0.47	0.26
	0.25	0.38	0.20
	0.30	0.50	0.29
	0.35	0.42	0.22
	0.40	0.50	0.29
	0.57	0.43	0.23

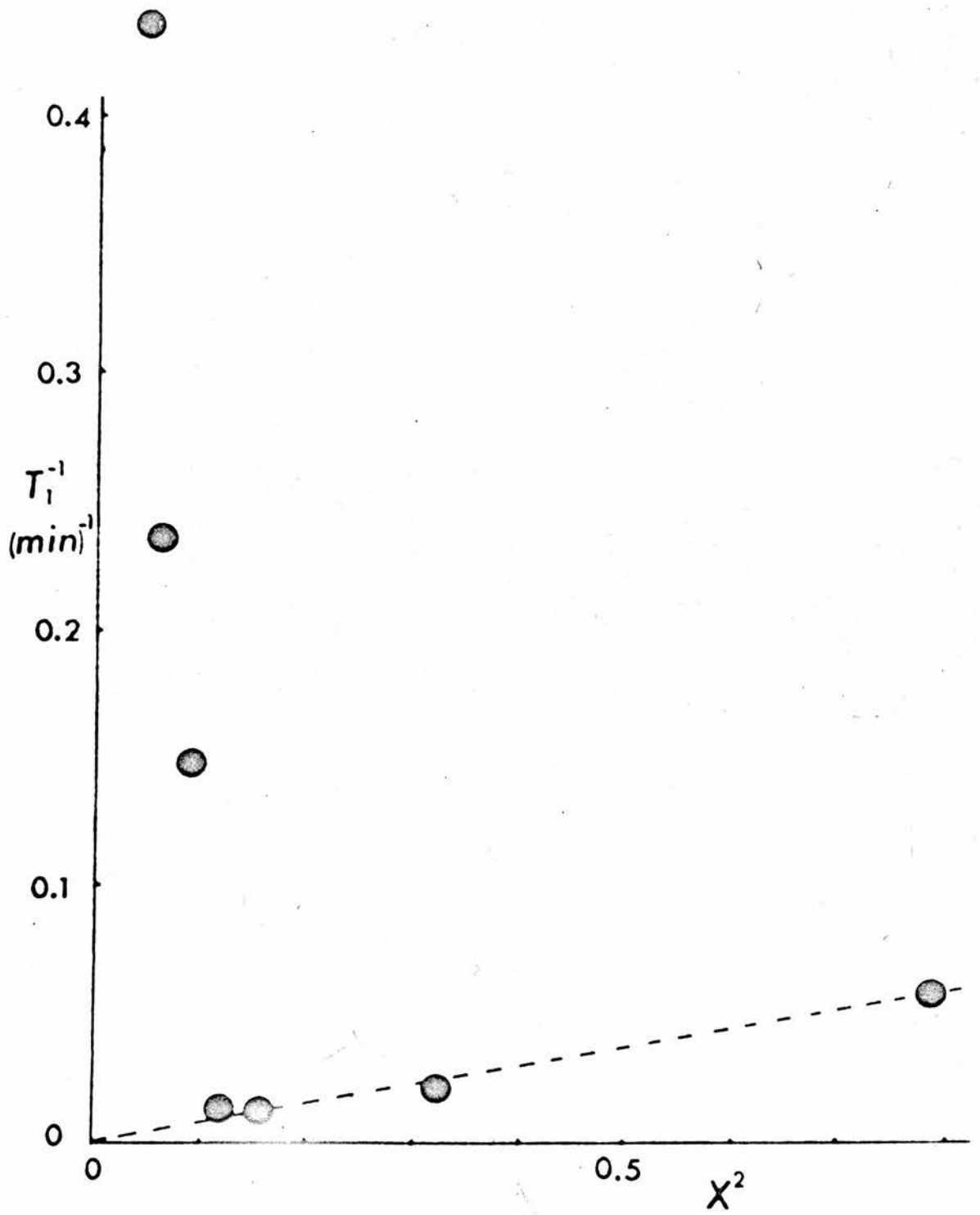


FIG 5.13 Na T_1 Data (Tunstall 1975)

Tunstall finds that T_1 has a temperature dependence characteristic of magnetic relaxation via conduction electrons over the entire x range studied, and has an x dependence shown in Fig. 5.13. For $x > 0.35$ the spin lattice relaxation rate is proportional to x^2 , which supports the idea of an exponential bandshape since

$$\frac{1}{T_1} \propto [\rho(E_F)]^2 \propto x^2 \quad (5.9)$$

Below $x = 0.35$, enhancements are found in the relaxation rate. Since these samples are in the diffusive region of conductivity, the Warren mechanism of section 2.7 may be involved. Using equation (2.44), a log-log plot of ρ against η does produce a reasonable straight line with gradient of one. However the product $\sigma\eta$ is far too large for the constant on the right hand side of equation (2.44) if the jump distance d is assumed to be equal to the lattice spacing. Jump distances about five times the expected distance are required to obtain agreement. This implies that the Warren mechanism alone probably cannot produce the large enhancements.

An alternative explanation is that lattice contraction as x decreases may cause Sodium 3s and 3p bands lying well above the conduction band at high x to be driven down in energy. Then the states at the Fermi surface would acquire some Sodium character. The Knight Shift is shown to decrease from -45 ppm ($x = 0.57$) to -26 ppm ($x = 0.22$). Tunstall proposed that 6% Sodium 3s and 15% Sodium 3p character could explain the large enhancements in the relaxation rate, but would have a smaller effect on the Knight shift due to cancellation of s contact with p core polarisation.

The FID T_2^* was found to be independent of x with a value $\approx 500 \mu\text{s}$. The non-observance of any dilution effect as x decreases (see section 2.8.1) is attributed to gradual removal of the satellites from the central transition by first order quadrupole coupling. The

echo T_2^* decreases as x decreases. This is explained by the change in occupancy of nearest neighbour Sodium shells. The T_2 of the Echo decreases as x increases, as is predicted by the effect of dilution. The extrapolated T_2 at $x = 1$ is however longer than that calculated from the second moment, probably because quadrupole interactions varying from site to site make the nuclei look "unlike", hence quenching the B term in the dipolar interaction, and narrowing the line.

Finally, a model is presented for the two sites. The FID nuclei are assumed to occupy two of the sites in a new octupled unit cell such that these sites are surrounded by Oxygens distorted in such a way as to retain cubic symmetry. The Echo nuclei can occupy the other six sites which have a non-cubic Oxygen environment. This model is discussed further in Chapter 7.

7. Weinberger¹²⁸ (1977) W Resonance

This work, on the same samples as 6, extended the Tungsten resonance to the low x range. The spin lattice relaxation rates (Fig. 5.14) show a temperature dependence characteristic of relaxation via the conduction electrons. For $x > 0.35$ T_1^{-1} shows the x^2 dependence expected from the exponential bandshape, while below $x = 0.35$ there is a slight drop below the x^2 line. The Knight shifts (Fig. 5.15) show the x dependence expected from

$$K \propto \rho(E_F) \propto x \quad (5.10)$$

above $x = 0.35$, but drop precipitously by an order of magnitude between 0.35 and 0.22. Weinberger explains the low x results as implying that the wavefunctions at the Fermi surface acquire about 20% Sodium character and about 6% Tungsten 6s character. The 6% 6s character provides additional relaxation but this will be more than cancelled by the loss of 20% 5d character. Hence the relaxation

rate would show a slight drop. However the 6s character would make the Knight shift less negative as would the loss of 20% 5d character, and hence these two add to produce the precipitous drop in K.

Weinberger also shows that if the wavefunctions acquire 20% Sodium character, then in order to explain the relaxation rate of the Sodium at low x, about half of that Sodium character must be 3s. However he is unable to explain why the Sodium Knight shift remains negative.

The Tungsten linewidths (Fig. 5.16) are broad, and show a maximum for $x \approx 0.4$. The similar magnitude of the linewidths and Knight shifts leads Weinberger to assume a distribution of Knight Shifts similar to that of Sundfors and Holcomb in doped Silicon¹²⁹.

In this model, the local magnetisation M_{loc} obeys the relationship

$$M_{loc} = N_{loc} \langle \mu_e \rangle \quad (5.11)$$

where N_{loc} is the local conduction electron density and $\langle \mu_e \rangle$ is the average electron magnetic moment which is not a local property since the spin flip time is greater than the electron transit time for several lattice constants

$$\langle \mu_e \rangle = \frac{2}{n} \rho(E_F) H_0 \mu_e^2 \quad (5.12)$$

where n is the total number of electrons per unit volume. Hence from (5.11) and (5.12)

$$\chi_{loc} = 2 \frac{N_{loc}}{n} \rho(E_F) \mu_e^2 \quad (5.13)$$

and from equation (2.23)

$$K_{loc} = \frac{2}{n\beta} H_{hf}^{loc} \mu_e^2 \rho(E_F) N_{loc} \quad (5.14)$$

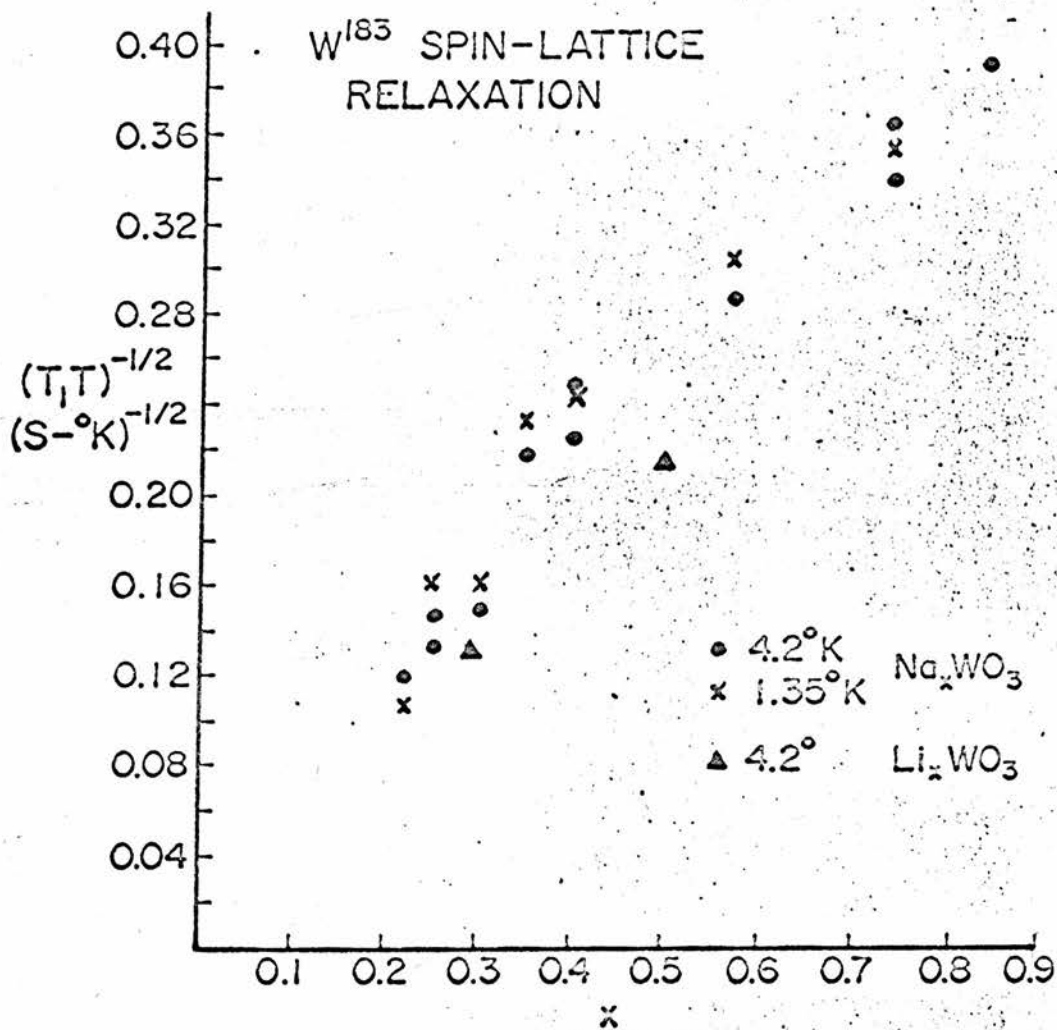


Figure 5-14 W^{183} T_1 results from Weinberger

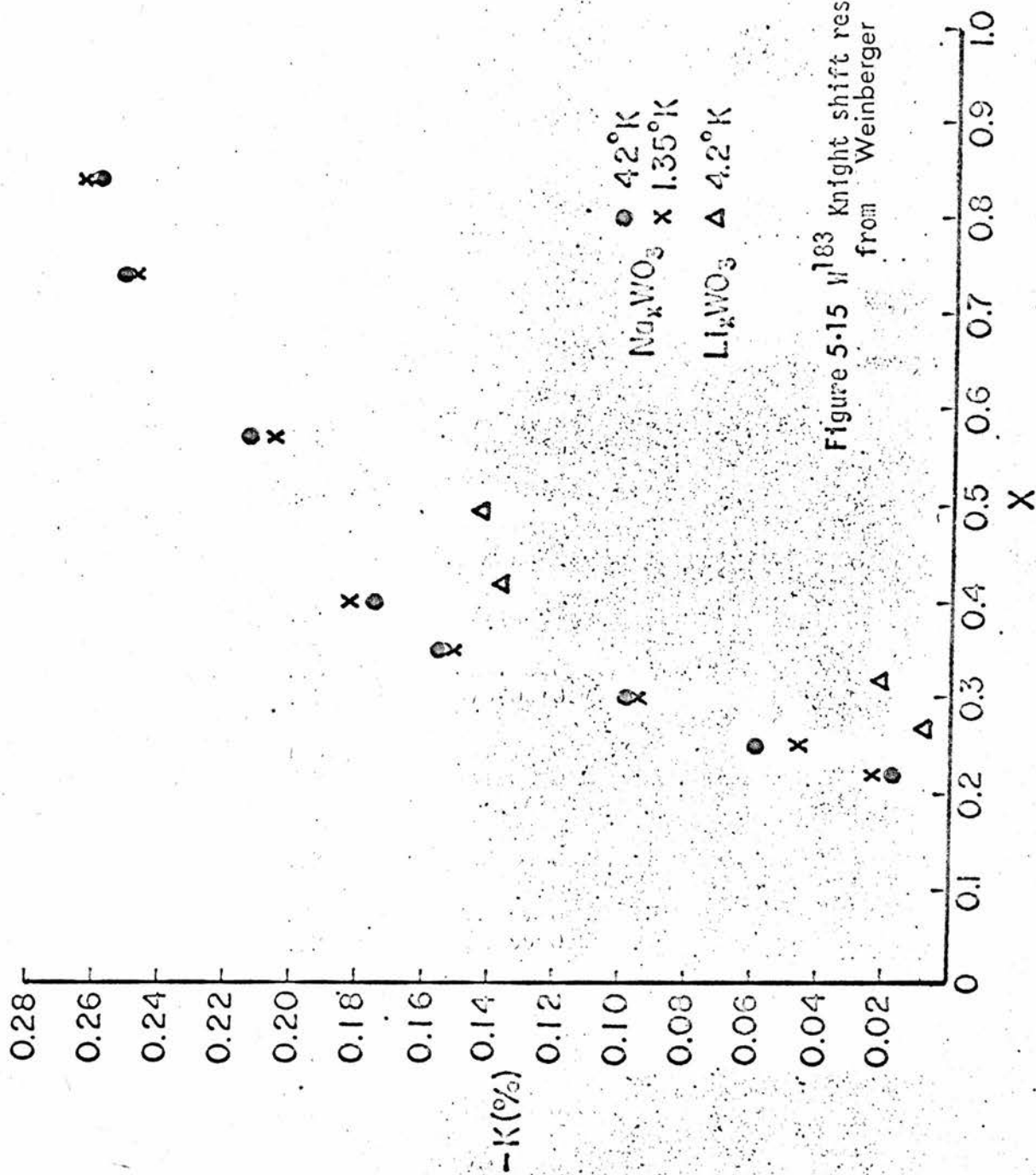


Figure 5-15 ^{183}W Knight shift results from Weinberger

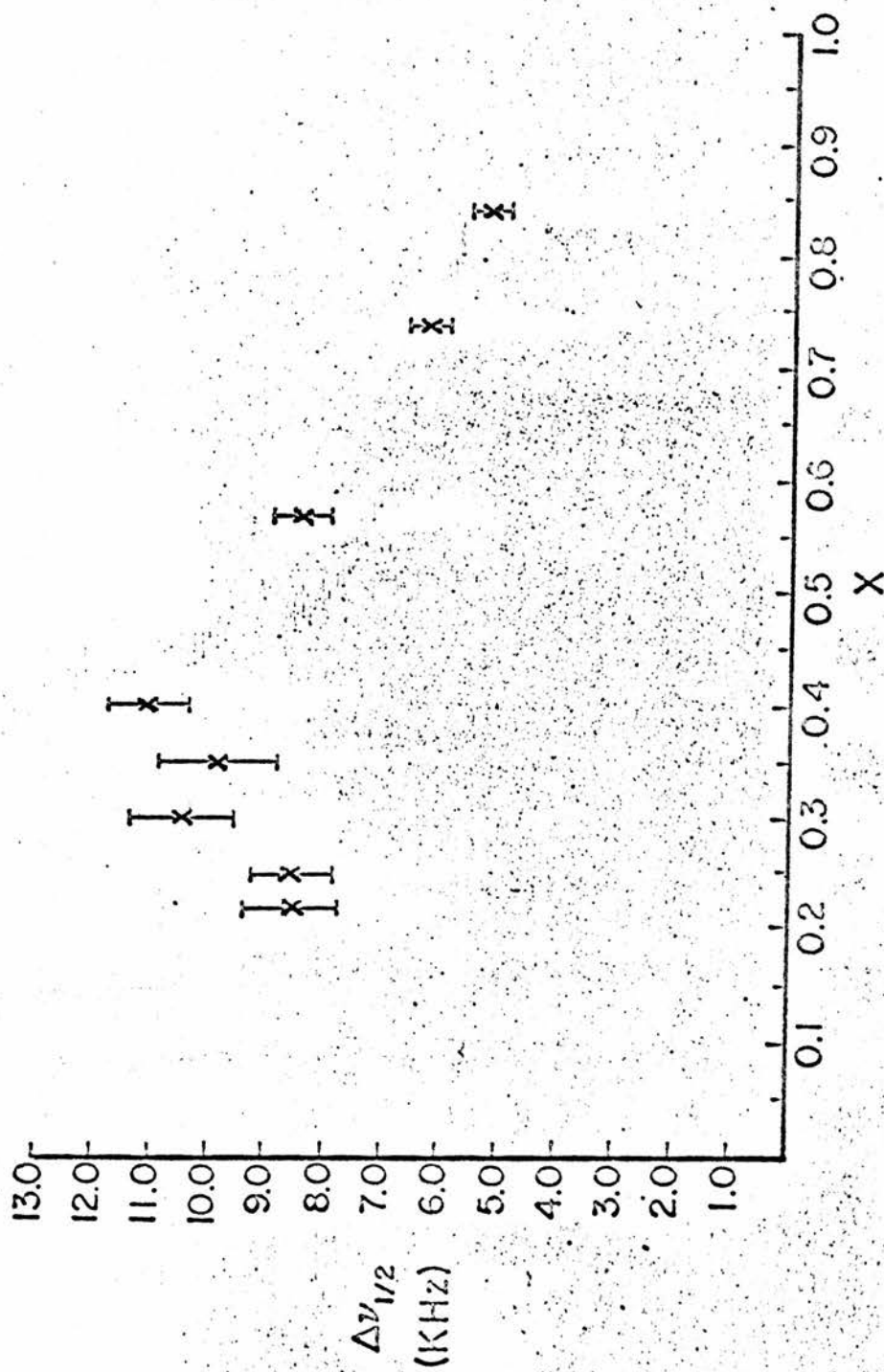


Figure 5-16 ^{183}W linewidths obtained by Weinberger

If the local density of conduction electrons is assumed to be the local Sodium density then

$$K_{loc} \propto \frac{1}{x} \rho(E_F) x_{loc} \quad (5.15)$$

The lineshape then depends on the distribution of K_{loc} , which from (5.15) depends on the distribution of x_{loc} . For a random arrangement of filled Sodium sites, this distribution is a Gaussian with a half width $\sqrt{x(1-x)}$. Hence the linewidth can be shown to be

$$\Delta\nu \propto \frac{1}{x} \rho(E_F) \sqrt{x(1-x)} \quad (5.16)$$

By using the specific heat data to establish

$$\rho(E_F) \propto (7.6x + 1) \quad (5.17)$$

and modifying this by some sort of cut off at low x to take into account the rapid drop in K below $x = 0.35$, then Weinberger shows that the predicted shape of $\Delta\nu$ does show a maximum around $x = 0.4$.

In conclusion, the last three investigations have shown that the two Sodium sites arise from Oxygen displacement rather than Sodium clustering. At high x there is support for the exponential band model with its prediction that $\rho(E_F) \propto x$. At low x there is evidence of some transfer of conduction electron character from Tungsten to Sodium, and/or some slowing down of the electron dynamics. Finally in Fig. 5.12 we include a table of the relative FID and Echo intensities obtained in these studies.

5.9 Other Bronzes and Related Compounds

The most commonly studied alkali Tungsten Bronzes are those involving Hydrogen, Lithium, Sodium or Potassium. Resistivity measurements (Fig. 5.17) demonstrate that the conduction processes

are essentially independent of the alkali atom and of the crystallographic phase, hence showing that the conduction band consists of states derived from the WO_3 matrix. This phase independence probably only holds for the tetragonal and cubic phases, since a recently discovered triclinic $Na_{0.33}WO_3$ ¹³⁰ has been found to be a semiconductor, and amorphous films of H_xWO_3 are only metallic above $x = 0.32$.

For H_xWO_3 , the magnetic susceptibility¹³² agrees with that of Na_xWO_3 . NMR¹³³ shows motional narrowing of the proton linewidth above 250 K which is attributed to Hydrogen diffusion through the lattice. This effect, and the change in colour it produces, have possibilities for display devices¹³⁴,

Weinberger¹²⁸ has studied the Li W resonances in Li_xWO_3 for $0.27 < x < 0.49$. No higher x crystals could be grown. He finds that the W resonance T_1 , K and linewidth are similar to those found in Na_xWO_3 but that the Li resonance is markedly different. The Li Knight Shifts are practically zero and T_1 s at 300 K decrease with increasing x as was found for the resonance. However T_1 gets shorter as the temperature is lowered which throws some doubt on sample purity. Comparison of the properties of Na_xWO_3 and Li_xWO_3 may however be clouded by the fact that the former the lattice contracts as x decreases whereas in the latter it expands.

Optical¹³⁶ and transport measurements in ReO_3 have shown that the conduction band is similar to that of the bronzes. NMR results¹³⁷ support this, since the relaxation is fast and the Knight shift is negative, with both T_1 and K agreeing with the values for the Tungsten in Na_xWO_3 extrapolated to $x = 1$. The linewidths show that quadrupolar effects are negligible, despite the large quadrupole moment of the Re nuclei. This is interpreted as implying that Oxygen displacements do not occur in ReO_3 .

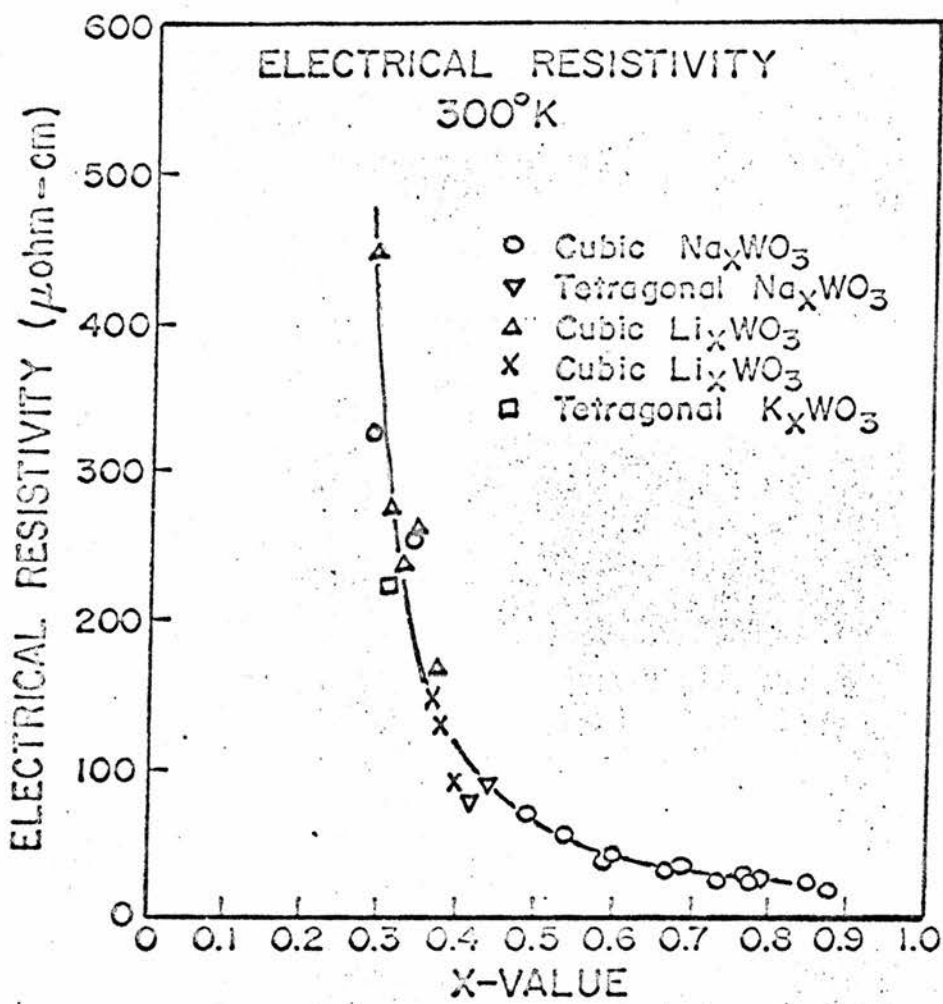


Figure 5-17 Resistivity of the alkali tungsten bronzes

Finally, the role of the A ion is not the same in all ABO_3 perovskites. For example¹³⁸ in $SrTiO_3$, the Sr spin lattice relaxation rate is fast, implying that the conduction band contains more A character than in the bronzes.

5.10 The Metal Non-metal Transition

The rapid decrease in conductivity as x approaches 0.2 in Na_xWO_3 , accompanied by evidence of thermal activation of carriers, indicates the existence of a metal non-metal transition around $x = 0.2$. The semiconducting properties of the different crystalline phases below $x = 0.2$ indicate that the electronic transition is accompanied by a structural transition, just as in the better known systems VO_2 and V_2O_3 ²⁴. Since the electronic properties on the semiconducting side of the transition are complicated by the different phases, descriptions of the mechanisms causing the transition are usually restricted to the metallic side.

Fuchs¹⁰⁰ and Lightsey⁸⁶ have treated the transition in terms of site percolation, where the conduction electrons exist in W 5d orbitals, but avoid those cells with vacant Sodium sites. The volume V occupied by the electron gas is then proportional to x . Using the free electron theory,

$$\rho(E_F) \propto Vn^{1/3} \propto x \quad (5.18)$$

since n is independent of x in each metallic region. This fits in with the specific heat and susceptibility data. Computer simulation of the system in terms of resistor arrays shows that the conductivity can be written as

$$\sigma = (x - x_c)^t \quad (5.19)$$

where $t = 1.5$ for site percolation, and x_c is the critical concen-

tration below which conducting paths no longer exist across the sample. x_c depends on the coordination number Z . For a cubic lattice with nearest neighbour linkages, $x_c = 0.307$ which is too large. Lightsey introduced an effective coordination number of 14, which takes into account linkages with second and third nearest neighbours, and obtained a good fit to the conductivity data with $x_c = 0.18$.

An alternative model of percolation in the bronzes is due to Webman, Jortner and Cohen⁵⁴, and has already been mentioned. They propose that not only do the electrons avoid vacant sites, but the Sodium atoms themselves tend to cluster together, producing local $x = 1$ regions. The surface energy limits the size of the clusters to about 100 Å in diameter. We shall discuss this model further in Chapter 6, and detail our objections to it in Chapter 7.

A different treatment of the transition is proposed by Mott¹³⁹ along the lines of some of the ideas in Chapter 3. He states that the three mechanisms which may each cause the transition are:

1. Random Na^+ charges introduce disorder into the system and so cause Anderson localisation.
2. An impurity band is formed, and Anderson localisation due to lateral disorder occurs at $x = 0.2$.
3. The Hubbard U splits the impurity band, and the transition occurs due to Anderson localisation in the pseudogap.

Since no enhancements are observed in the specific heat or magnetic susceptibility, Mott assumes that the Hubbard U plays very little part in the transition. Also the random nature of the donors, and the relatively high concentration at which the transition occurs, indicate that localisation probably sets in long before an impurity band is formed. Hence Mott proposes that Anderson localisation occurs in the tails of the conduction band. As x decreases, the Fermi level moves down the band, until at $x \approx 0.2$ it crosses the

mobility edge, and all states become localised. Support for this explanation comes from conductivity measurements¹⁴⁰ in polycrystalline $\text{Na}_x\text{WO}_{3-y}\text{F}_y$, where the samples span the transition, which seems to occur at $x \approx 0.2$ for $y \approx 0.16$. The conductivity temperature data show all the characteristics of an Anderson transition, with a minimum metallic conductivity of $300 \Omega^{-1} \text{cm}^{-1}$, and evidence for $T^{\frac{1}{4}}$ hopping below the transition at low temperatures.

Returning to the Na_xWO_3 Hall data, Mott proposes that the temperature dependence of the $x = 0.22$ sample may be explained by the onset of Anderson localisation. From equation (3.15) R_H should increase threefold over its free electron value before localisation occurs. This seems to happen if the low temperature Hall data is taken. Also if the specific heat is taken to be a measure of $\rho(E_F)$, then $\rho(E_F)$ is about 1/3 of its free electron value at $x = 0.22$. Both these pieces of evidence are taken to imply that at $x = 0.22$, the electron gas is very near an Anderson transition.

The increase in R_H at $x = 0.22$ becomes smaller as the temperature is raised. Mott proposes that $\rho(E_F)$ lies in a sharply rising density of states such that at high temperatures, many electrons will be excited into states away from the mobility edge and so will not exhibit such a large R_H .

CHAPTER 6RESULTS6.1 Compressibility

Since many of the results in this chapter are measured as a function of pressure, we shall firstly study the effect of pressure on Na_xWO_3 . The compressibility of an $x = 0.68$ sample has been calculated from elastic constant data to be¹⁵³

$$\beta = 8.2 \times 10^{-4} \text{ K Bar}^{-1} . \quad (6.1)$$

We shall assume that β has no strong x dependence in the cubic range, and provide arguments supporting this assumption in Chapter 7. Therefore application of a 4 KBar pressure should reduce the lattice constant by 0.11%. However equation (5.1) shows that the lattice constant may also be reduced by decreasing x , and it can be shown that a reduction of x by about 0.05 can cause a similar contraction to that caused by 4 KBar pressure. Since at the low x end of our sample range the x values differ by 0.05, then a pressure of 4 KBar should effectively span the region in between samples. This should enable us to separate the effect of reducing x from the accompanying effect of reducing the lattice constant.

6.2 The Two Signals

The Na^{23} NMR response in Na_xWO_3 is characterised by two signals. If a $\pi/2$ pulse is applied to the spin system, the resultant free induction decay can be decomposed into two components:- a relatively intense component A with a short T_2 , and a less intense component B with a much longer T_2 . If a $\pi/2 - t - \pi$ pulse sequence is used, then a spin echo appears at a time $2t$ after the first pulse. The decay time of this echo is similar to that of the A component, implying that only the A component is refocused by the second pulse. The B component

is not refocused since its T_2 is the same as its T_2^* .

In this work, the A component proved difficult to study by a $\pi/2$ pulse alone, since its short decay ($\approx 40\mu\text{s}$) was partially obscured by receiver recovery from overload after the pulse. Hence the A component was studied by spin echo techniques, and is referred to as the Echo. The B component however was studied by applying a $\pi/2$ pulse, and is referred to as the FID.

The relative intensities of the two signals are shown in Fig. 6.1 as a function of x . Column 2 introduces the parameter Y defined as

$$Y = \frac{\text{FID Intensity}}{\text{FID Intensity} + \text{Echo Intensity}} \quad (6.2)$$

Since we shall see that the Echo signal does not contain any contribution from the first order quadrupolar satellites, then Y gives a measure of the number of sodium nuclei contributing to the FID as a fraction of the total number of sodium nuclei, provided that the FID does not contain any contribution from its satellites. If the FID signal does contain the satellites, then the ratio of the FID nuclei to the total number of nuclei is given by

$$Y^* = \frac{0.4 \times \text{FID Intensity}}{0.4 \times \text{FID Intensity} + \text{Echo Intensity}} \quad (6.3)$$

The values of Y^* are tabulated in column 3. Assuming that the first order quadrupolar spectrum does not vary strongly with x , then it can be seen that the ratio of the number of Sodium nuclei contributing to the FID to the total number of Sodium nuclei is constant over the whole x range studied. The actual value of the ratio depends on whether or not the satellites contribute to the FID. It was also found that this ratio is independent of pressure up to 4 K Bar.

Column 4 lists the intensity of the FID for each sample. Although each sample was weighed and the intensity corrected for different sample weights, different particle sizes can lead to different RF penetrations, and so column 4 can only be regarded as approximate. However it does show that the FID intensity is roughly proportional to x . Since Y and Y^* are constant with x , then the total intensity is proportional to x , indicating as has previously been noted⁹⁵, that wipe out of the Sodium resonance by second order quadrupolar effects is negligible. In addition, comparison of the $x = 0.25$ sample (where presumably skin depth problems are negligible) and NaCl, yielded after the intensities had been corrected for different densities, roughly the same number of nuclei present.

6.3 The Echo Width

In Fig. 6.2, the full width of the Echo at half maximum height is shown as a function of x , and can be seen to exhibit a broad maximum around $x = 0.5$. Bonera et al⁹⁴ have measured the decay constant of the Echo for $x = 0.52, 0.72$ and 0.86 , and find that it is about three times smaller at 8 MHz than at 24 MHz. This frequency dependence implies that the Echo results from those nuclei experiencing static second order quadrupolar broadening of their central transition. Our results at 50 MHz support this, since Bonera's results at 24 MHz, translated into Echo widths at 4.2K give widths about one half of those in Fig. 6.2. In addition, the x dependence of Bonera's widths match our own x dependence in the same x region. Unfortunately Bonera's samples do not extend to low enough x values to include the maximum.

The Echo widths reported by Tunstall⁹⁵ at 11 MHz are smaller than those predicted from our work assuming the 11/50 reduction due to frequency. However the errors in the widths of the 11 MHz Echoes are

FIG. 6.1 Intensity Data (Atmospheric Pressure)

x value	Y %	Y*%	Relative FID Intensity (arbitrary units)
0.22	21	9.6	0.25
0.25	23	10.1	0.32
0.30	19	8.6	0.66
0.35	19	8.6	0.55
0.40	17	7.6	0.63
0.57	19	8.6	1.04
0.74	19	8.6	1.00
0.84	21	9.6	1.03

The errors in Y and Y* are about 20%. The errors in the actual measurements of the FID Intensity are probably about 10%.

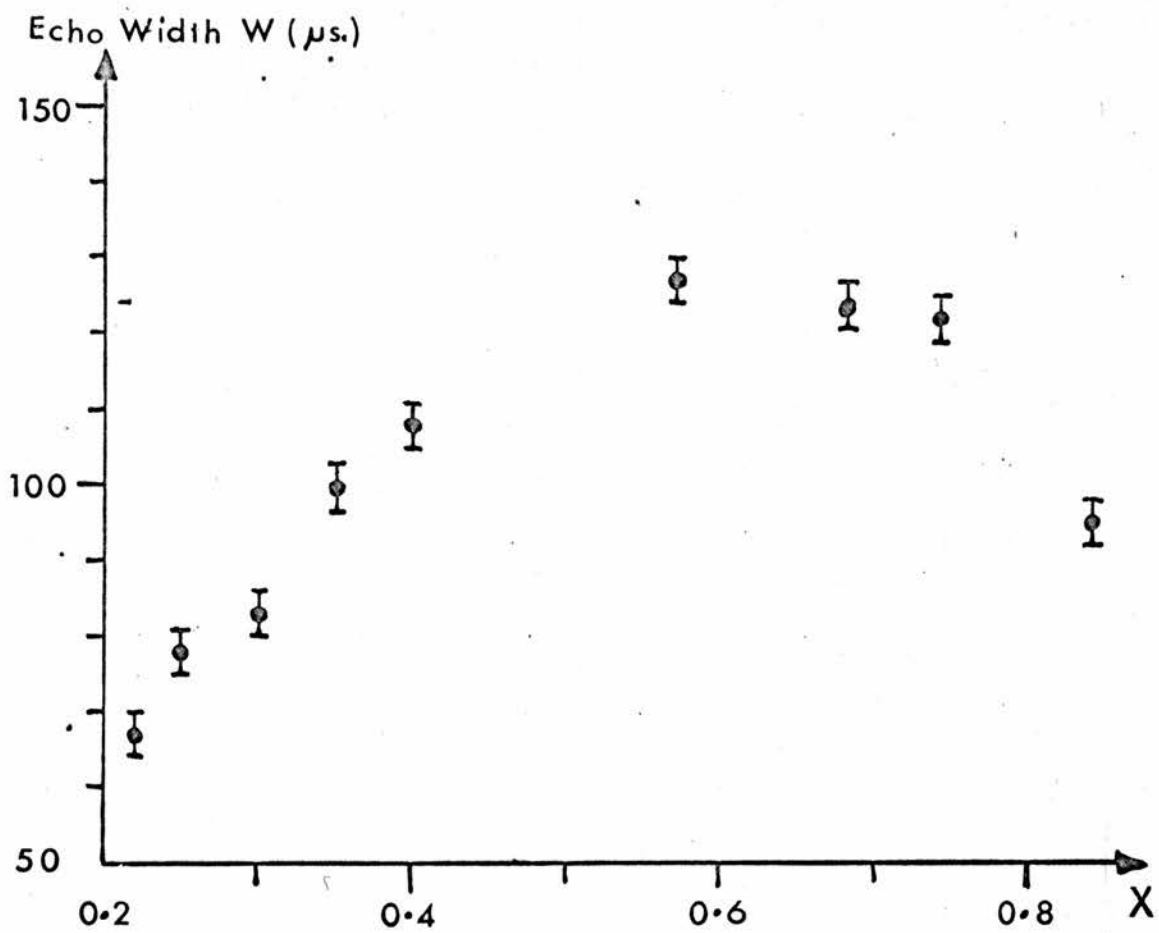


FIG 6.2

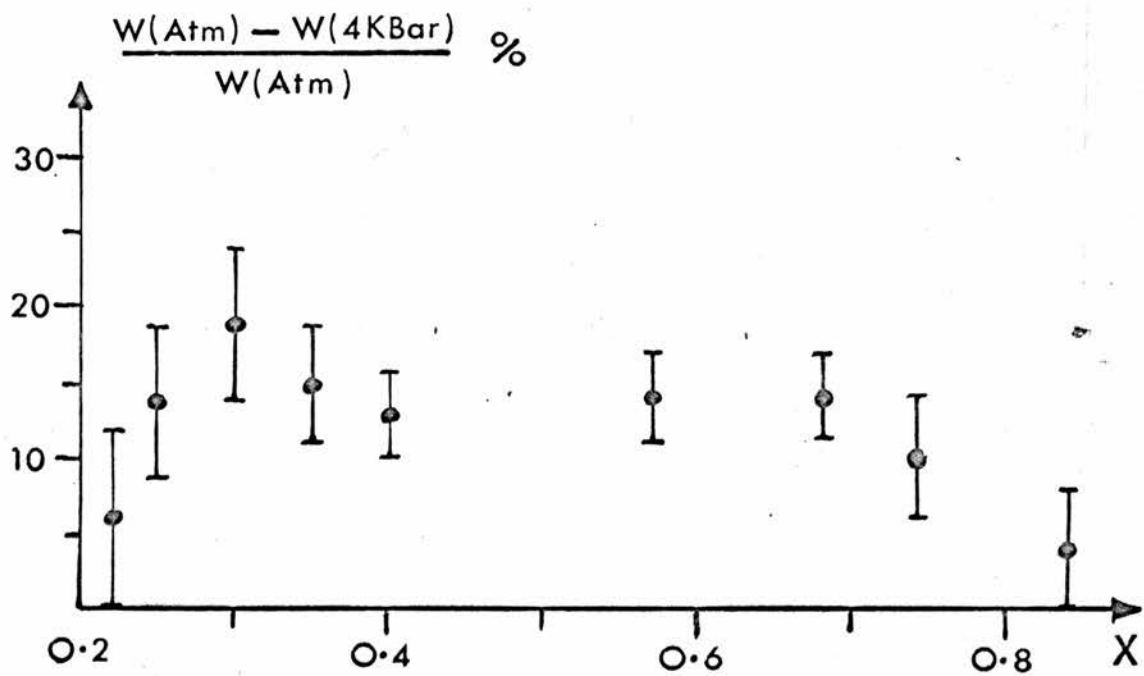


FIG 6.3

large because the technique used involved recording the Echoes on Polaroid film with a minimum sweep of $50\mu\text{s}/\text{cm}$. Hence if we assume a 50% error in each measurement, the 11 MHz results probably agree with our own. The Echo widths reported by Fromhold and Narath¹²⁴ must be disregarded since as Bonera et al have pointed out, they merely provide a measure of the spectral width of the pulse. This also means that their intensity ratio for the FID and Echo must be in error.

For our powders, the central transition in the presence of second order quadrupolar broadening, when all nuclei are subjected to the same field gradient should look like that of Fig. 1.1. Hence if the B_0 field is set to sit on one peak, then beats should be observed from the other. If the field is set elsewhere, then beats should be observed from both the peaks. No beats were obtained, and the Echo looked symmetric and Gaussian in shape. Hence we propose that some distribution of field gradients must be present, causing the lineshape of Fig. 1.1 to be smeared out into a broad Gaussian type of line.

The pressure dependence of the Echo width in Fig. 6.3 shows that the width decreases with pressure, the relative change being roughly constant ($\approx 15\%$) over most of the x range, but tending to zero at $x = 0.22$ and also at $x = 0.84$.

6.4 The Echo and FID T_2

The T_2 values for the Echo are shown in Fig. 6.4. The T_2 was measured by the standard saturation $-t - \pi/2 - \tau - \pi$ sequence, where t was kept constant and of the order of T_1 , and τ was varied from about 0.2 ms to 1.2 ms. A plot of the log of the echo height versus τ gives T_2 . The plots were slightly non-linear, which implies that the decay is non-exponential, and so T_2 is defined as the time for the echo height to fall to $1/e$ of its value at $\tau = 0$. These plots were also

used in obtaining the intensity data of section 6.2. The echo height was measured at $t \approx 5T_1$ and with a pulse separation $\tau \approx 0.7$ ms. The intensity required is that at $\tau = 0$, so the measured intensity was extrapolated back to $\tau = 0$ using the above plots.

From the discussion of linewidths in Chapter 2, we should expect that in the x region studied, the Echo T_2 should be proportional to $x^{-\frac{1}{2}}$ due to dilution of the spins. Fig. 6.4 shows that this relation probably is valid, although the error bars are large enough to allow an x^{-1} dependence also. However the better fit is obtained by the $x^{-\frac{1}{2}}$ dependence. The extrapolation to $x = 1$ produces a T_2 of about 0.5 ms. The T_2 calculated from equation (2.47) assuming that the linewidth is due to Sodium-Sodium dipolar interaction is 0.35 ms. However when adjacent nuclei have their central transitions occurring at different frequencies, as happens when second order quadrupolar interactions vary from site to site, then the nuclei become "unlike" and T_2 is extended by about 50%. Since there is some evidence from section 6.3 that the Echo nuclei do experience some distribution of quadrupolar interactions, then this mechanism becomes a plausible explanation of the extension.

The FID T_2 is shown in Fig. 6.5 and was calculated by observing the decay after a single $\pi/2$ pulse. As can be seen, it is relatively independent of x over the whole range of x studied, in marked contrast to the Echo T_2 . This observation led Fromhold and Narath¹²⁴ to propose that the FID nuclei exist in clusters, and the Echo nuclei occur randomly outside these clusters. However Tunstall⁹⁵ has proposed that as x decreases, increasing first order quadrupole interactions gradually remove the satellites from the central transition, thus broadening the line, and countering the effect of dilution so as to make the FID T_2 independent of x .

Both the Echo and FID T_2 s were found to be independent of pressure up to 4 K Bar.

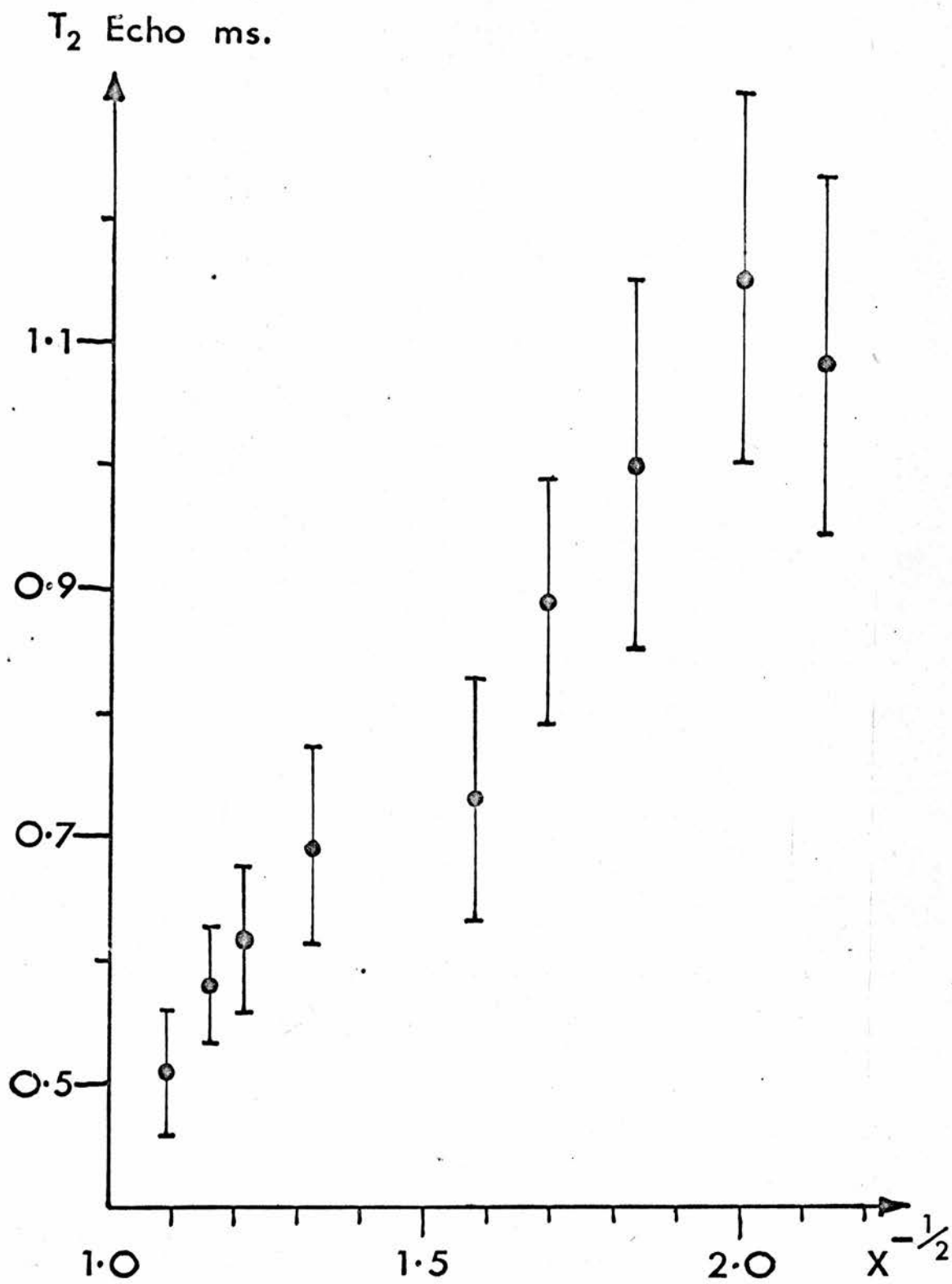


FIG 6.4

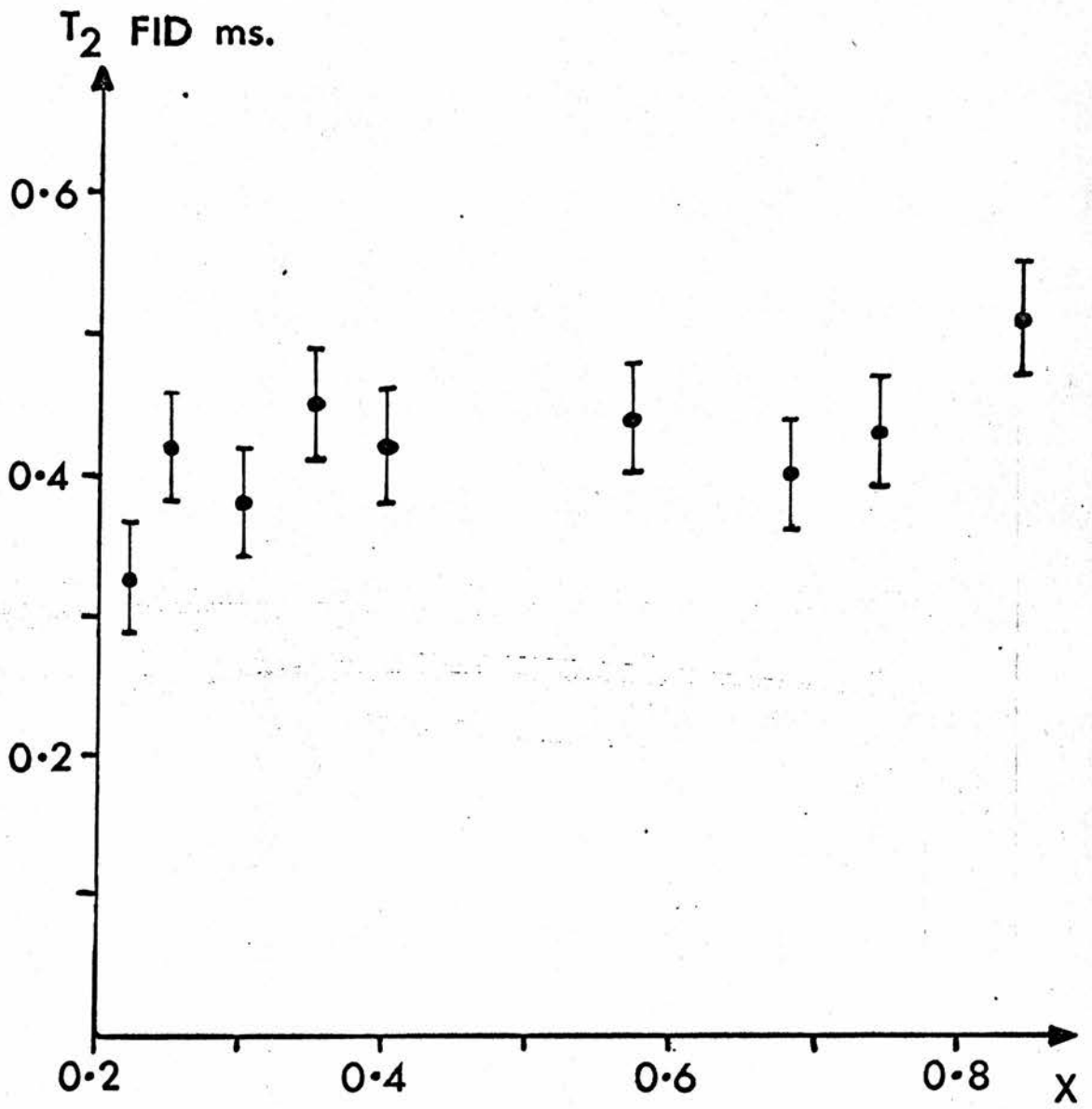


FIG 6-5

6.5 Pulsewidths

It was found that the pulsewidth required to maximise the FID ($\pi/2$ FID) was different from that required to maximise the Echo. The decay following a single pulse of width t_w is shown in Fig. 6.6 for different t_w . It can be seen that the short Echo decay after the pulse is maximised by about a $4\mu\text{s}$ pulse, whereas the FID is maximised by a $6\mu\text{s}$ pulse. Indeed for pulses of 7 and $8\mu\text{s}$, the reversal in sign of the Echo signal indicates that the pulse is now greater than π for the Echo nuclei, whereas the non-reversal of the FID signal shows that the pulse for those nuclei is still less than π . An alternative procedure of maximising the Echo height produced by a $t_w - 2t_w$ pulse sequence also gave a value for $\pi/2$ Echo similar to those obtained from the above method. The $\pi/2$ pulsewidths for FID and Echo are shown in the following table for various samples.

x value	$\pi/2$ FID μs	$\pi/2$ Echo μs
0.22	5.5	4.0
0.25	5.5	4.0
0.84	6.5	4.0

The pulsewidths quoted are widths at half peak height and have errors of about 10%. The $\pi/2$ pulsewidth for Aluminium metal was measured at 4.2K to be $10\mu\text{s}$. Allowing for the fact that the Aluminium loads the coil more than the Bronzes, the true $\pi/2$ pulse for the Bronzes is probably around $8\mu\text{s}$.

The explanation of this anomaly may lie in the discussion of the pseudo-spin $\frac{1}{2}$ nuclei of section 2.9. The Echo nuclei will have their satellites so far removed from the central transition that equation (2.54) will hold, and the $\pi/2$ pulse width will be halved, in keeping with the experimental results. In order to explain why the $\pi/2$ pulse for the FID is less than twice that for the Echo, we propose that there

PULSEWIDTH μs

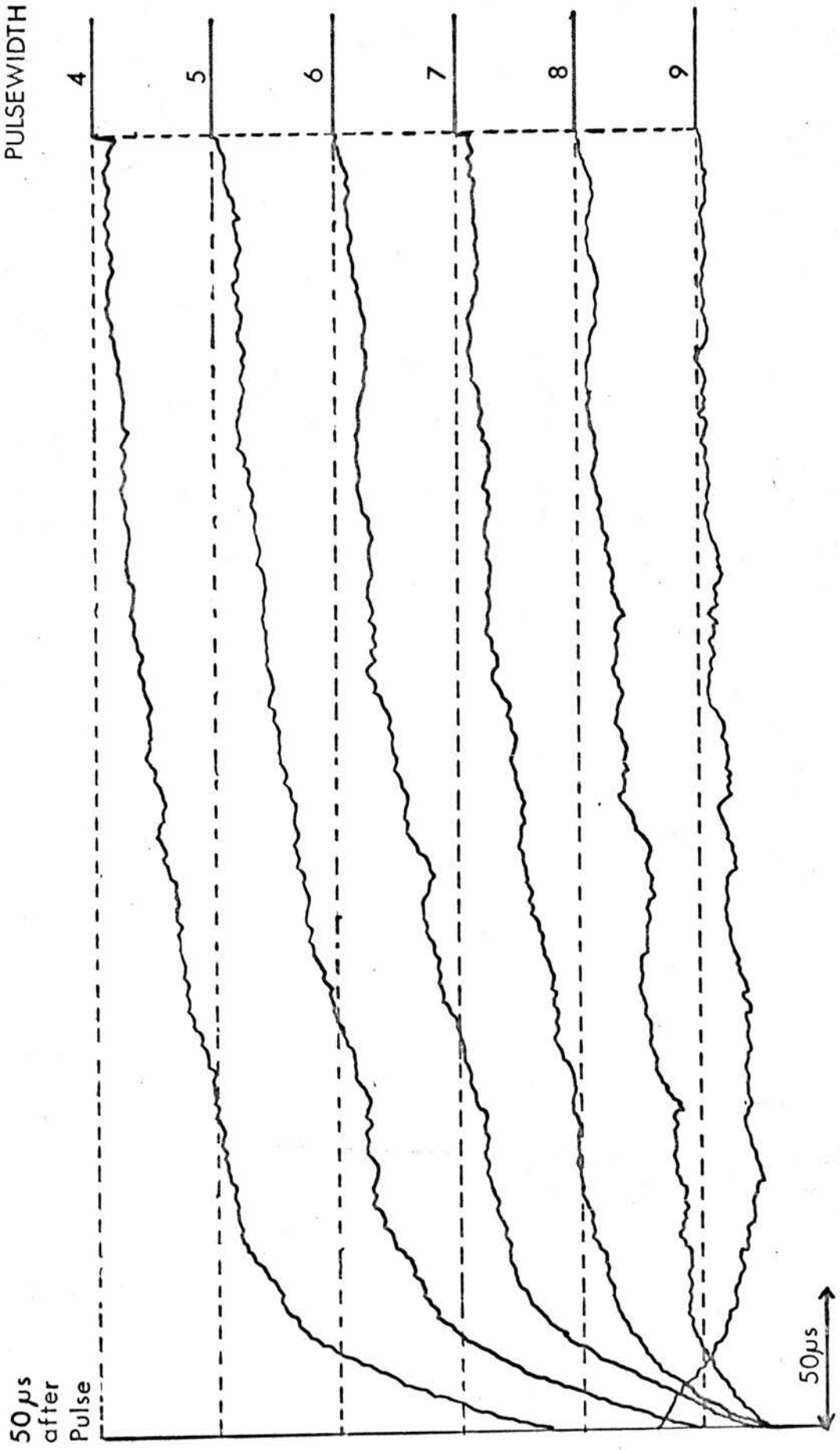


FIG 6-6 DECAYS AFTER PULSE

must be some distribution of first order quadrupolar interaction, resulting in some FID nuclei having their satellites within the B_1 field, and others outside. We note that we have already proposed some type of distribution of field gradients for the Echo nuclei also. The immediate consequence of this is that the ratio of FID nuclei to the total number of Sodium nuclei will lie somewhere in between the Y and Y^* values of section 6.2.

The different pulsewidths must throw some doubt on previously published intensity ratios. Bonera et al⁹⁴ obtained ratios for Y of about 25%, but the intensities seem to have been measured after a single pulse. Since we have shown that it is impossible to maximise both the FID and Echo signals with the same pulse, then the relatively good agreement between their ratios and ours may be coincidental, arising from the fact that their pulsewidth may be less than $\pi/2$ for the FID and more than $\pi/2$ for the Echo.

Tunstall⁹⁵ obtained a value for Y of about 45% but this was obtained by using a pulsewidth to maximise the FID. This will result in too large a value for Y , since the Echo will not see a $\pi/2 - \pi$ sequence.

6.6 Quadrupolar Echoes

We have attempted to obtain information on the first order quadrupole spectrum for the FID nuclei by the method of quadrupolar echoes discussed in section 2.9. We have used a $\pi/2 - t - \pi/3$ pulse sequence with t between $100\mu\text{s}$ and $200\mu\text{s}$ but could not detect any such echoes. Unfortunately if the echo exists, it occurs at a time $2t$ after the first pulse, which is precisely where the magnetic spin echo occurs. Since the Echo nuclei are more numerous than the FID, the magnetic spin echo may obscure the quadrupolar echo from the FID. Bonera et al⁹⁴ claim to have separated the two echoes by applying a

$\pi/2 - \tau - \pi/2$ sequence with the second pulse shifted in phase by 90° relative to the first place. Separation is possible since the phase shift does not affect the spin echo, but increases the height of the quadrupolar echo. They find that the quadrupolar echo width is larger than 10 Gauss, but cannot obtain any more information, presumably because their B_1 field is of similar magnitude.

6.7 Spin-Lattice Relaxation Rates

The spin-lattice relaxation time T_1 was measured by a comb of $\pi/2$ pulses to saturate the resonance, followed at time τ by a sampling $\pi/2$ pulse for the FID measurements, or by a $\pi/2 - \tau - \pi$ sequence with $\tau = 700\mu\text{s}$ for the Echo measurements. In Fig. 6.7 the spin-lattice relaxation rate T_1^{-1} is plotted against x^2 . This relationship has already been shown in section 5.8 to be consistent with the dependence of $N(E_F)$ with x . The graph is similar to that in Fig. 5.13 except that data points have been added above $x = 0.57$, and that there is a reduction in the relaxation rate of the $x = 0.22$ sample to a value similar to that of $x = 0.25$. The $x = 0.22$ data point at 11 MHz is shown by the triangle on the graph for comparison. For $x > 0.35$ the proportionality of T_1^{-1} against x^2 is quite marked, whereas for $x < 0.35$, the enhancement of the relaxation rate is again evident.

For $x > 0.35$, the recovery of the magnetisation after a comb is found to be exponential, with the line being easily saturated by relatively short comb lengths. However for $x < 0.35$, recoveries are non-exponential. Tunstall⁹⁵ has suggested that this non-exponentiality is not caused by incomplete initial saturation since long intense combs were used, and he proposed that in this region T_1 was varying so rapidly as a function of x , that the small inhomogeneities in x which exist in the samples would give a distribution of T_1 values, and hence a non-exponential recovery. We offer two new experimental results in favour

of this latter argument. Firstly we have performed a "hoist" type experiment on the $x = 0.25$ sample by removing the NMR probe from the B_0 field but keeping it in the Helium bath. The sample remained out of the field for about one hour ($\approx 20 T_1$) and was then plunged back into the B_0 field, and a sampling $\pi/2$ pulse applied after a time τ . The time required to raise or lower the sample was about 5 seconds. This method gave a similar non-exponential recovery to that produced by saturation by a comb. Secondly the recovery of the $x = 0.22$ sample is more exponential than that of the $x = 0.25$ sample. This is especially marked for the Echo signal. This return towards an exponential recovery was not in evidence in Tunstall's measurements at 11 MHz. We correlate this with the fact that in our measurements, the $x = 0.22$ sample may lie on a plateau region of T_1 and hence would not experience such a large distribution of T_1 s as Tunstall's 11 MHz result where T_1 is still varying rapidly with x .

In previous work⁹⁵, T_1 is defined as the time for the magnetisation to recover to $(1 - e^{-1})M_0$. Using this definition we obtain the points in Fig. 6.7 shown by the black circles. However this definition overemphasizes the contribution of fast relaxation rates to the total rate. A numerical simulation of a distribution of T_1 values centred at T_0 and with a width of about $\frac{1}{2}T_0$ produced the curve in Fig. 6.8 where $\ln(M_0 - M)$ is plotted against time after saturation. If T_1 is taken to be the time to recover to $(1 - e^{-1})M_0$, then a time $T_1 = T_0^*$ is obtained where $T_0^* < T_0$. We have found that if instead of this method, the tangent to the curve at $\frac{1}{2}M_0$ is drawn, then the gradient of this tangent produces a value very close to T_0 . With this method we have calculated corrected relaxation rates for $x < 0.35$ which are shown by the crosses on Fig. 6.7. Comparison of the T_1 value given by this correction method and that of the original $(1 - e^{-1})M_0$ method can give quantitative measure of the non-exponentiality. If we define a parameter A as

$$A = \frac{T_1(\text{corrected}) - T_1(\text{original})}{T_1(\text{original})} \quad (6.4)$$

then A measures the deviation from the exponential recovery and is shown in Fig. 6.10. It can be seen that the maximum occurs for $x = 0.25$ and $x = 0.30$, which is the region in which T_1 is changing most rapidly.

The relaxation rate for the Echo was also measured and follows the same pattern as that of the FID, except that the Echo T_1 was always slightly shorter than that of the FID. The two T_1 s are tabulated in Fig. 6.9.

The pressure dependence of T_1 is also shown in Fig. 6.9 and is shown graphically for the FID signal in Fig. 6.12. The Echo pressure dependence is similar to that of the FID. It can be seen that in the region $x < 0.35$ there is a small increase in T_1 i.e. a decrease in the relaxation rate. This change was difficult to measure, since it was of the same order as the error in the measurement of T_1 . We found that in this region of non-exponential recoveries, a large error was introduced into the measurement by drawing the curve through the experimental points. This was due to three factors. Firstly, if the data points lie on a curve, and there is an error bar on each point, then it is more difficult to draw a reproducible best curve through all the points, than it is if as in the case for $x > 0.35$, all the data points lie on a straight line and a straight line is drawn through them. Secondly, the definition of T_1 as the time to fall to $(1 - e^{-1})M_0$ is more crucially dependent on the value of M_0 when the data points are not exponential. Finally, for the low x samples, the signal to noise ratio is reduced due to the decrease in the number of Sodium atoms, and this leads to larger error bars on each data point, making it more difficult to draw the best curve through the points. Hence in order to measure the small shifts in T_1 with pressure, it was necessary for

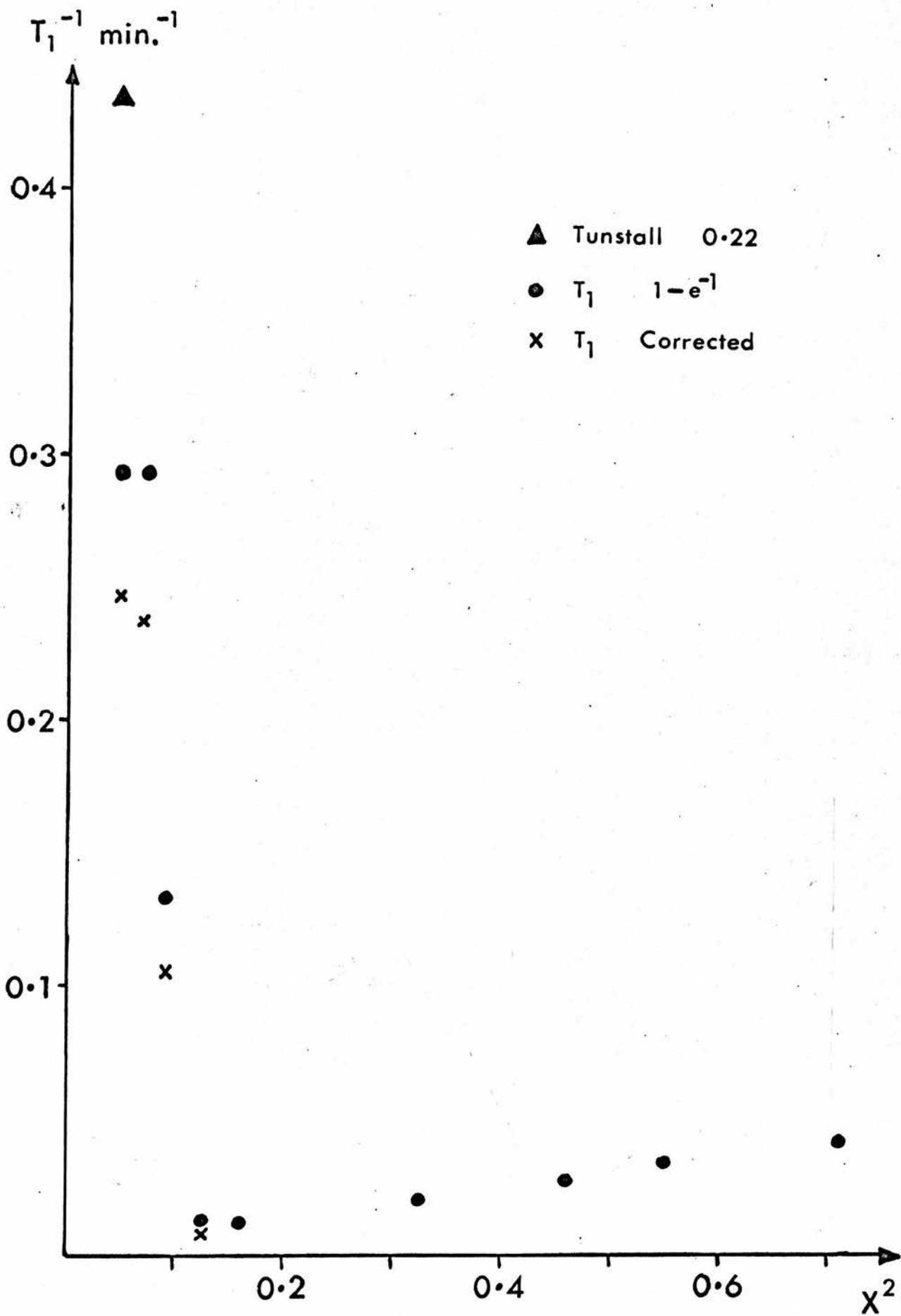


FIG 6.7 FID

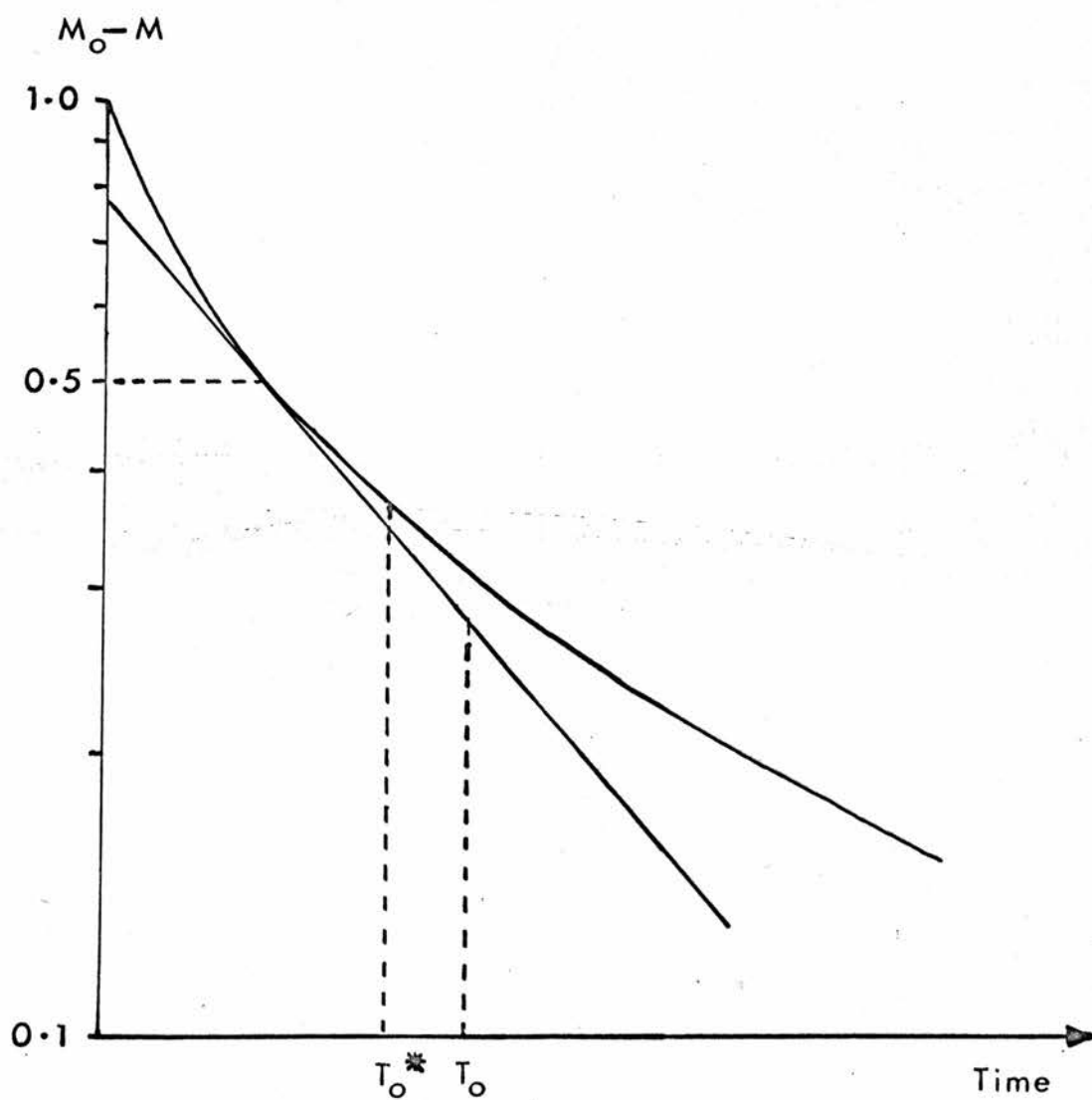
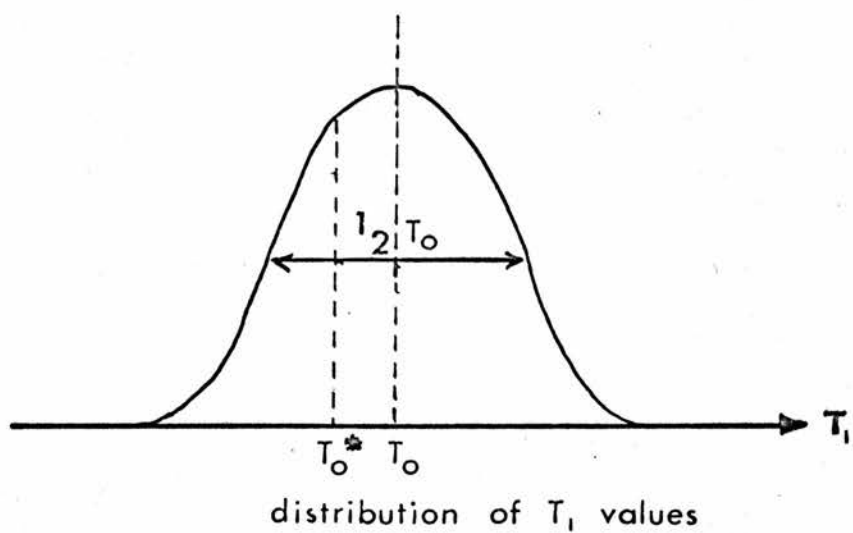


FIG 6-8 Correction to T_1 data

FIG. 6.10 Non exponentiality of T_1

A parameter %

x value	FID Atm.	FID 4 K Bar	Echo Atm.	Echo 4 K Bar
0.22	21	19	14	9
0.25	24	21	12	15
0.30	24	23	14	13
0.35	15	11	7	7

FIG. 6.11 Temperature dependence of T_1
for the two lowest x samples using corrected T_1 data.

x = 0.22

$T^{\circ}K$	FID Atm.	FID 4 K Bar	Echo Atm.	Echo 4 K Bar
4.2	4.1	4.4	4.1	4.7
2.1	15.3	10.0	12.2	11.0

x = 0.25

$T^{\circ}K$	FID Atm.	FID 4 K Bar	Echo Atm.	Echo 4 K Bar
4.2	4.2	5.8	3.9	4.6
2.1	9.6	9.7	9.0	8.3

FIG. 6.9 Spin-Lattice Relaxation Times

T ₁ (FID) minutes				
x value	Atm.	Atm. (corrected)	4 K Bar	4 K Bar (corrected)
0.22	3.4	4.1	3.6	4.4
0.25	3.4	4.2	4.8	5.8
0.30	7.5	9.3	10.0	12.3
0.35	80.0	92.0	82.0	91.0
0.40	79.6		77.8	
0.57	50.0		48.8	
0.68	37.0		33.0	
0.74	29.8		29.5	
0.84	24.2		27.0	

T ₁ (Echo) minutes				
x value	Atm.	Atm. (corrected)	4 K Bar	4 K Bar (corrected)
0.22	3.6	4.1	4.3	4.7
0.25	3.4	3.9	4.0	4.6
0.30	5.5	6.3	7.4	8.4
0.35	65.0	70.0	70.0	75.3
0.40	75.4		70.0	
0.57	49.0		50.8	
0.68	31.7		32.2	
0.74	27.5		24.6	
0.84	22.0		22.5	

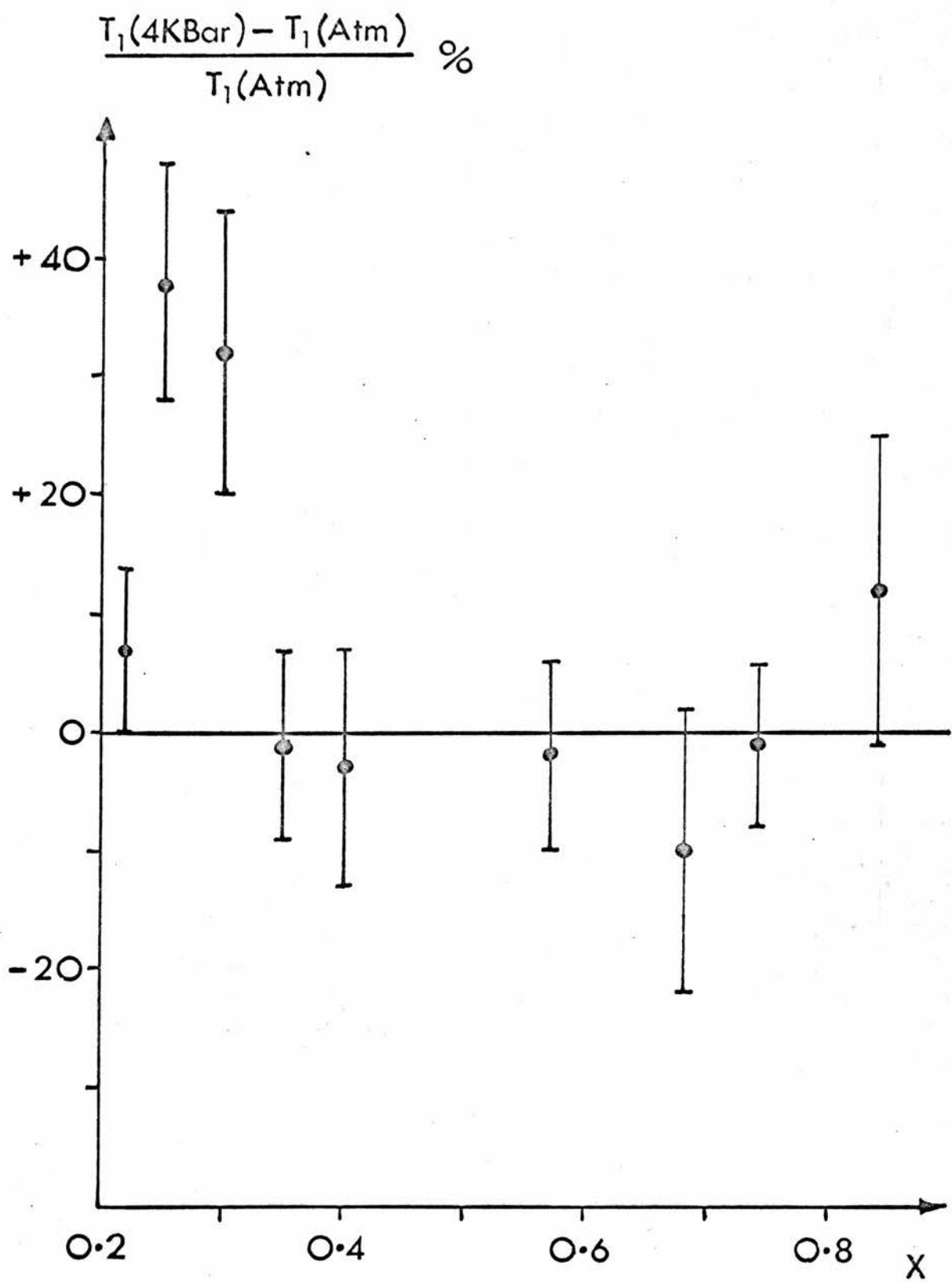


FIG 6.12 Pressure dependence of T_1 (FID)

$x < 0.35$ to take between five and ten separate determinations of T_1 , and by calculating the mean and the standard error, the error in T_1 could be reduced to about 10%. For $x > 0.35$, the better signal to noise ratio and the exponential recovery enabled T_1 to be measured to within 10% error by a single set of data.

The flattening of the relaxation rate at $x = 0.22$ and the field dependence of this sample led us to measure the relaxation rates of the two lowest x samples at 2.1 K. The results in Fig. 6.11 show that at atmospheric pressure, both samples do not follow the $T_1 T = \text{constant}$ dependence predicted in section 2.7, and found in the higher x samples. The deviation is marginal for the $x = 0.25$ sample, but quite marked for the $x = 0.22$ sample. It is also in evidence in Tunstall's measurements⁹⁵ of the same two samples although it is not commented on. We find also that pressure tends to drive both of the samples towards a better fit to $T_1 T = \text{constant}$. The lineshapes of these two samples was also studied at 2.1 K and it was found that there was no measurable difference between the shape at 4.2 K and that at 2.1 K.

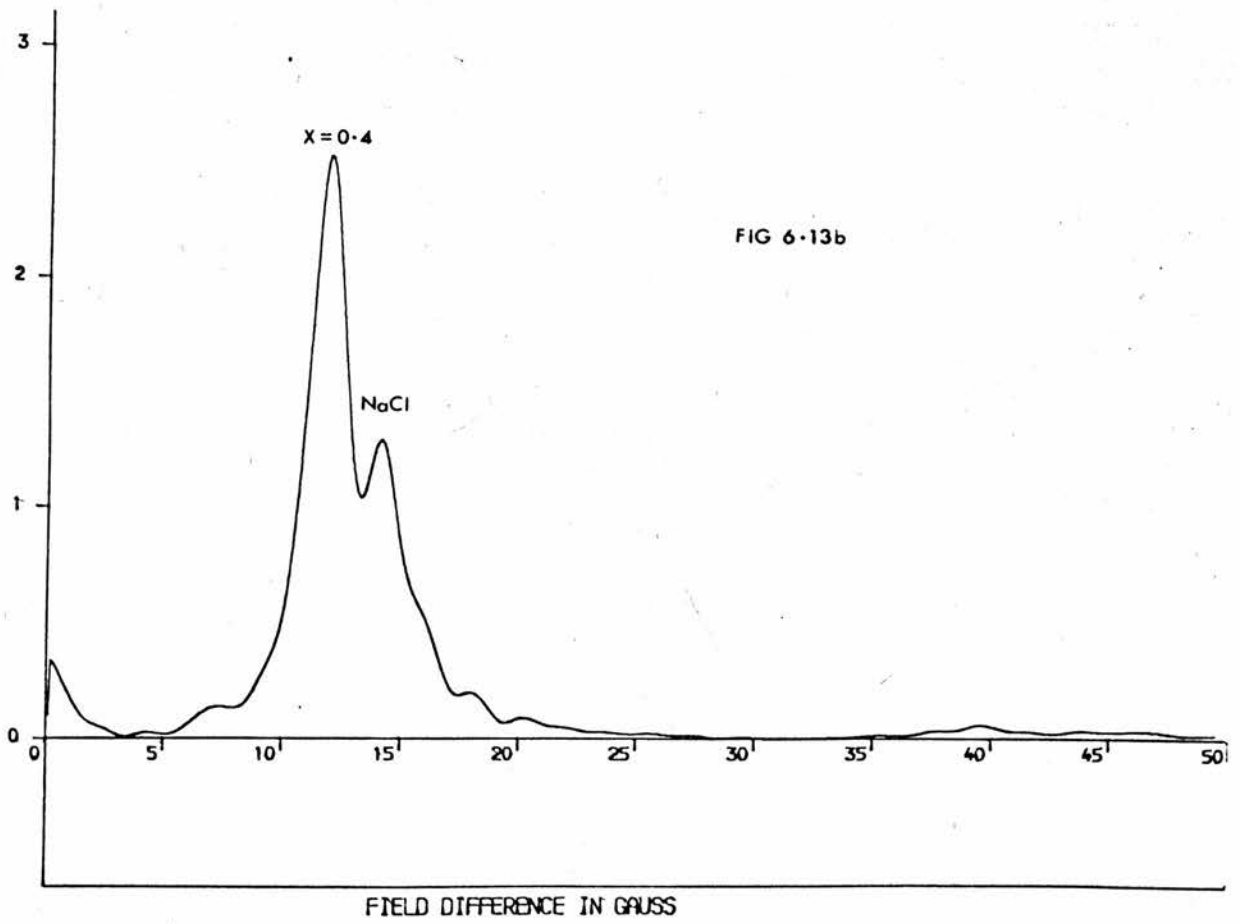
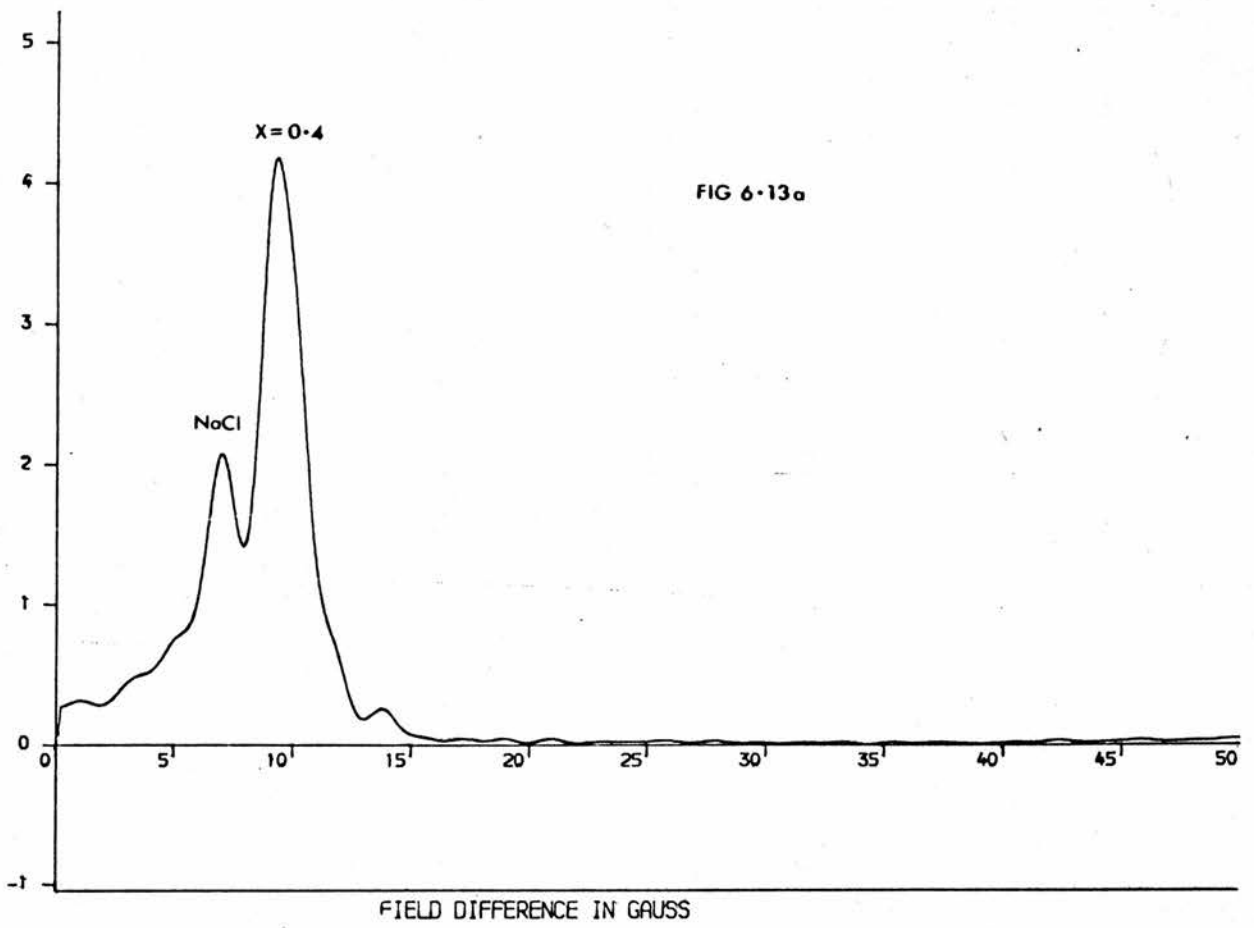
6.8 The Knight Shift

The shift of the Sodium resonance in the bronzes was measured relative to the Sodium resonance in NaCl by mixing the bronze samples with analytically pure NaCl powder. The level of any impurity in the NaCl was less than 3 ppm. The FID from the composite samples was Fourier transformed and then the Power Spectrum was plotted. Details of this procedure are given in the Appendix. A typical Power Spectrum is shown in Fig. 6.13. The top trace is for a B_0 field less than that required for resonance and hence the shift is negative. If the B_0 field is increased so that it is greater than that required for resonance, then the bottom trace is obtained.

Recognition of the peaks is achieved by noting that NaCl has a much longer T_1 than the bronze. Hence if the time between saturation and the sampling $\pi/2$ pulse is increased, the bronze peak reaches a constant height, whereas the NaCl peak is still increasing. Also since the two peaks are close together, they will only be resolved if they are of comparable intensities. This can also be achieved by varying the time between saturation and the sampling pulse. As can be seen from Fig. 6.13, there is a possibility that the more intense bronze peak could overlap the NaCl peak sufficiently to cause the latter peak to appear shifted towards the bronze peak. This was checked by subtracting the bronze peak on the side opposite to the NaCl peak from the total spectrum on the NaCl peak side. It was found that this rarely made any difference to the position of the NaCl peak.

For each sample, field settings and times between pulses were varied, resulting in about twelve separate spectra. The mean of these was taken as the Knight Shift K , and the value of K for different x is shown in Fig. 6.14. The results show that the shifts are all negative with a minimum around $x = 0.5$. This we shall interpret as being due to an increase in the shift roughly proportional to x with a bump superimposed on the line below $x = 0.5$. Although the line proportional to x cannot be accurately determined since we do not have sufficient samples in this region, there is evidence from other work¹²² that this dependence is followed between $x = 0.5$ and 0.75 . We cannot find evidence of the decrease in the Knight shift at high x , although our samples probably do not go high enough.

The Korringa products are shown for both the Tungsten and Sodium nuclei in Fig. 6.15. The products are approximately constant at high x , but fall by an order of magnitude at low x . The drop in the Sodium product is due to the enhanced relaxation rate, whereas the Tungsten drop is due to the reduction in the Knight shift. Finally the Sodium Knight shift is independent of pressure up to 4 KBar.



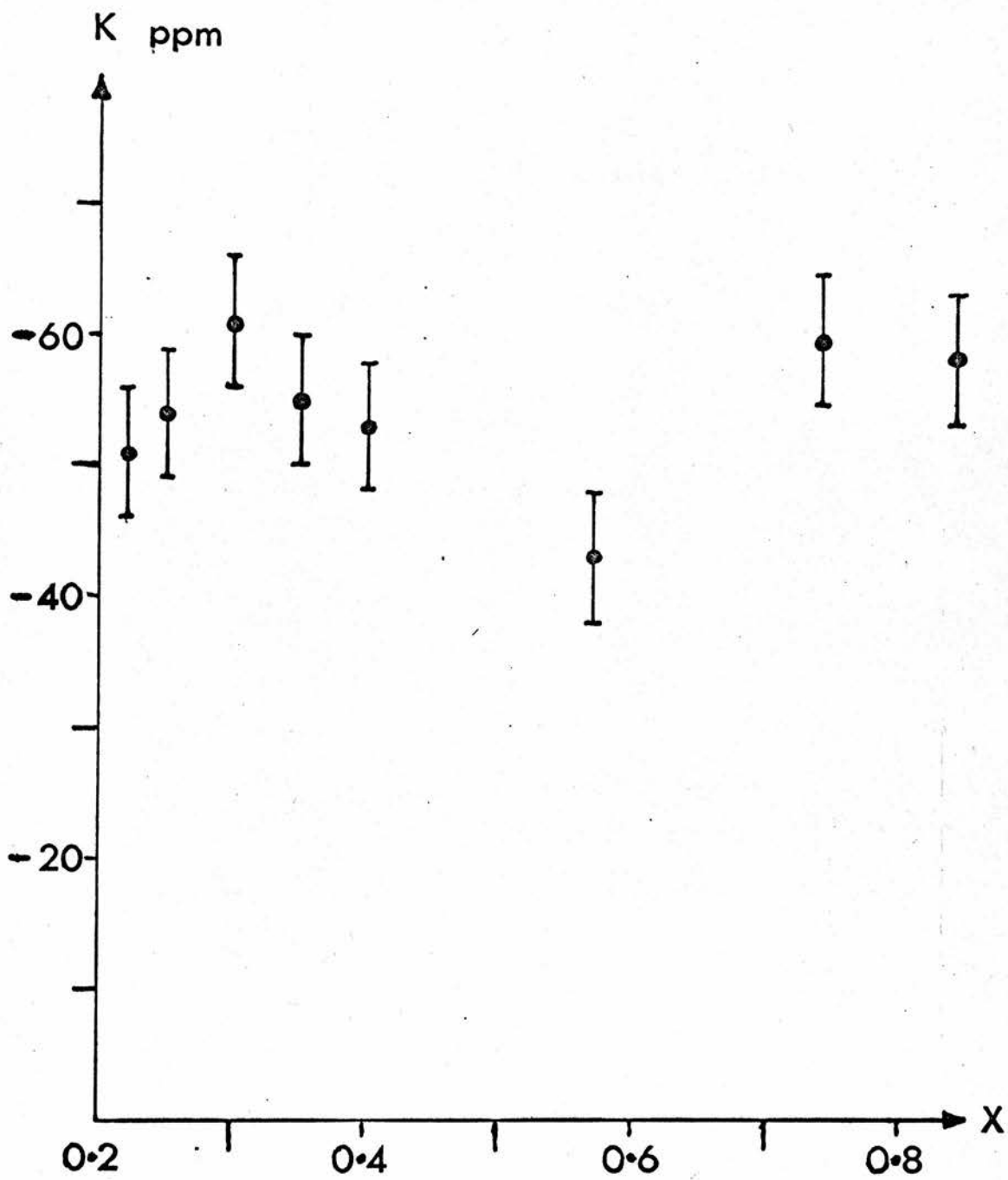


FIG 6.14 Knight Shifts

FIG. 6.15 Korringa Products

$$K^2 T_1 T \times 10^{-6} \text{ seconds } ^\circ K$$

x. value	Sodium	Tungsten
0.22	2.7	2.2
0.25	3.1	12.4
0.30	8.7	43.2
0.35	70.1	49.8
0.40	56.4	52.9
0.57	23.3	52.7
0.74	26.1	49.9
0.84	20.5	41.3

6.9 Electrostatic Energies

As was mentioned in section 5.10, Webman, Jortner and Cohen⁵⁴ have proposed that metallic clusters of local concentration $x = 1$ are formed in the bronzes. The physical origin of their formation is shown to lie in the relative magnitudes of two energies calculated for clustered and dispersed phases.

(a) An electronic band energy arising from the transfer of electrons from Sodium to Tungsten. Using a semicircular band model, Webman, Jortner and Cohen show that at low x this energy is negligible for a dispersed phase and is about 1.6 eV per electron for the clustered phase.

(b) An electrostatic energy resulting from the attraction between the Sodium ion and the conduction electron. For the dispersed phase, Webman, Jortner and Cohen consider the potential energy of a Sodium ion surrounded by a charge of minus one eighth of an electronic charge on each of the eight nearest Tungsten atoms, a distance $\sqrt{3}/2a$ away, giving an energy

$$E_2^d = -\frac{2}{\sqrt{3}} \frac{e^2}{4\pi\epsilon_0 a} \quad (6.5)$$

Mutual repulsion between electrons is invoked to halve this, giving an energy of about -2.2 eV. For the clustered phase, the Sodium ions and the conduction electron on each Tungsten site ~~from~~ ^{form} a CsCl structure with a Madelung energy of

$$E_2^c = -1.76 \frac{e^2}{4\pi\epsilon_0 a} = -6.6 \text{ eV} \quad (6.6)$$

This calculation shows that the clustered model is more stable than the dispersed by about 2.8 eV per Sodium atom. However it is possible that if screening is considered, then this may be reversed. Also Webman, Jortner and Cohen neglect any ionicity in the WO_3 matrix,

which will have a different energy for the two models. Finally, in a recent paper, Crandall and Faughan¹⁵⁴ have shown that thermodynamic measurements on the bronzes do not support the cluster model. In addition to the usual energy terms they also calculate the entropy term and show that this will always oppose clustering.

We have calculated the Madelung energy for Na_xWO_3 following a point charge method due to Whittingham¹⁵⁵, and assuming full ionicity of all the atoms (i.e. Na +1, W +6, O -2). Whittingham has calculated the four lattice sums

$$a = 1855.5058606$$

$$b = 1856.5235555$$

$$c = 5570.6294663$$

$$d = 5569.8995850$$

with energies calculated from

	W	on	a	sites
Tungsten	O	"	c	"
	Na	"	b	"
	Na	on	a	sites
Sodium	W	"	b	"
	O	"	d	"
	O	on	a	sites
Oxygen	2/30	"	d	"
	1/3W	"	c	"
	1/3Na	"	d	"

which gives an electrostatic energy per cell for the basic WO_3 lattice of

Tungsten $(6 \times 6)a + (6 \times -2)c$

Oxygen $(-2 \times -2)a + (-2 \times -2)2/3d + (-2 \times 6)1/3c$

and since there are three Oxygens to one Tungsten, the total electrostatic energy per cell is

$$-71.6388 \frac{e^2}{4\pi\epsilon_0 a} \quad (6.7)$$

We have calculated the Madelung energy for Na_xWO_3 as a function of x for the dispersed model, and making two assumptions.

Firstly every Sodium site is occupied by a charge of $+x$. When the whole lattice sum is considered, this is equivalent to a charge of $+1$ on x Sodium sites and zero on the others.

Secondly the $-x$ charge of the conduction electron is uniformly distributed among the Na^+ , W^{6+} and O^{2-} ions. This results in the charges

$$\text{Na}(+0.8x) \quad \text{W}(6-0.2x) \quad \text{O}(-2-0.2x)$$

and gives an energy

$$(-71.6388 - 2.224x - 0.809x^2) \frac{e^2}{4\pi\epsilon_0 a} \quad (6.8)$$

which is shown by the curve on Fig. 6.16, where the variation of the lattice constant a with x has also been taken into account. We note that this equation compares favourably with that derived by Smith¹⁵⁶, who assumes a uniform smear of conduction electron charge over the whole cell. His relation for the energy is

$$(-71.6388 - 1.3122x - 1.4187x^2) \frac{e^2}{4\pi\epsilon_0 a} \quad (6.9)$$

The Madelung energy of the clustered model will be the sum of the energies of the basic WO_3 matrix regions and the $x = 1$ regions, and is determined by the straight line in Fig. 6.16. We see that the

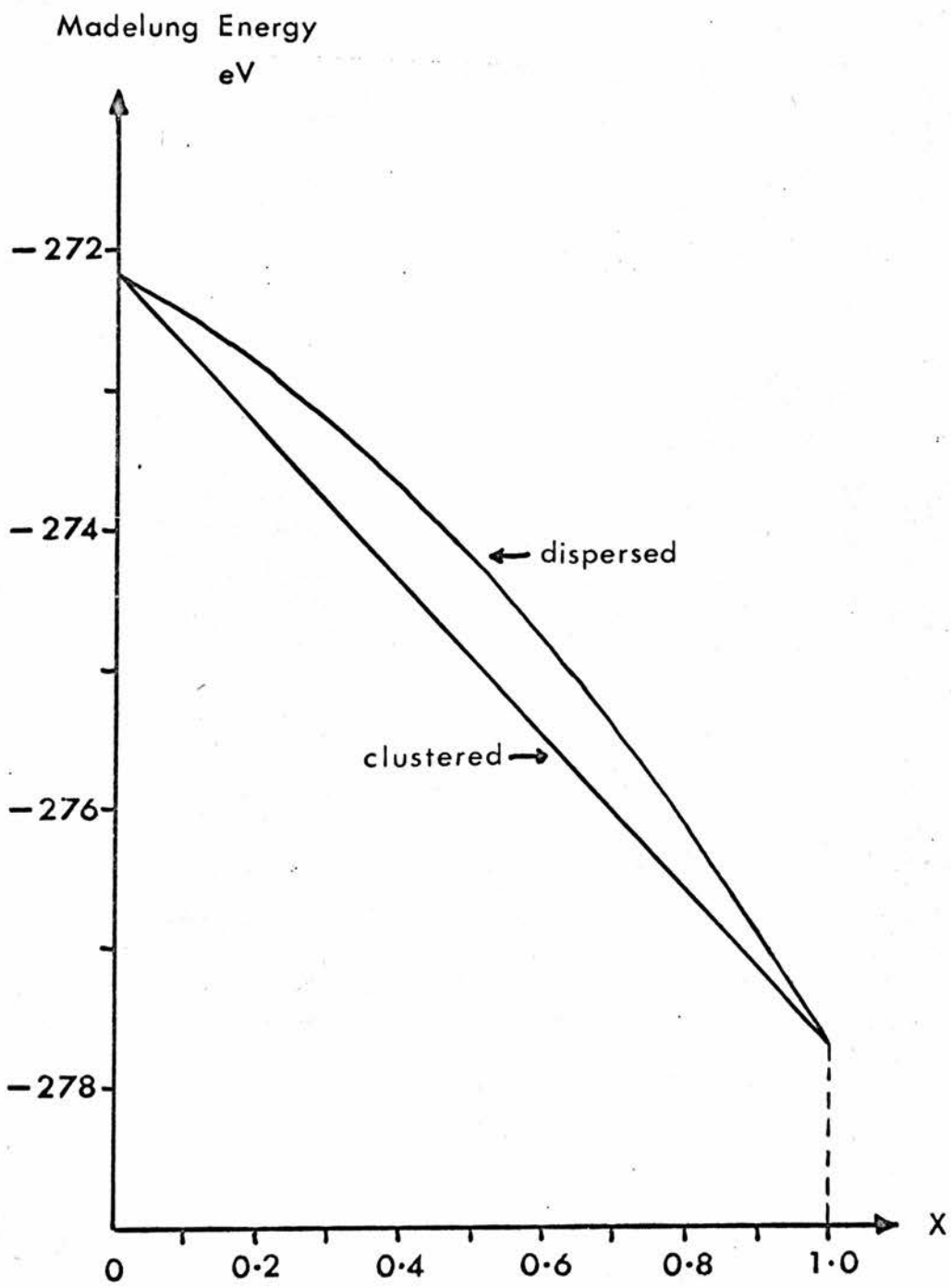


FIG 6.16

cluster model is more favourably electrostatically by at most about 0.8 eV. However when the original Webman, Jortner and Cohen band energies are considered, the larger band energy of the clustered model should make the dispersed system more favourable energetically.

Although our method is also approximate since it ignores screening, we have shown that the relative stabilities of the two models depend critically on the assumptions made in calculating the energies. This is probably due to the energy difference between the two models being so small compared to the total energies of about 280 eV. Hence we do not consider that it is feasible to predict the stability of one model purely on energy considerations.

CHAPTER 7DISCUSSION7.1 Structural properties derived from quadrupolar spectra and linewidth data

The data to which this discussion refers may be summarised as follows. The two different signals, FID and Echo, are assumed to originate from nuclei in different crystalline environments. The FID nuclei are situated in a predominantly cubic environment, although the satellites may be removed from the central line. No information on these satellites could be obtained by the method of quadrupolar echoes, but pulsewidth measurements indicate some distribution of the quadrupole coupling constant. The FID T_2 remains approximately constant over the whole range of x , although showing some tendency to fall away in the $x = 0.22$ sample. The Echo nuclei are situated in a heavily distorted environment such that the quadrupolar satellites are completely removed from the resonance, and the central transition is broadened by second order quadrupolar interaction. The lack of any observed structure in the Echo leads us to assume once again the existence of a distribution of quadrupole coupling constants. There is a maximum in the Echo width around $x = 0.5$ which implies either a minimum in the average quadrupolar coupling constant, or a minimum in the width of the distribution of coupling constants. The Echo width decreases with pressure. The relative change in 4 K Bar is about 15% for all x except $x = 0.22$ and $x = 0.84$. The Echo T_2 values show the $x^{-\frac{1}{2}}$ dependence predicted from dilution of the nuclei. The ratio of the FID nuclei to the total number of Sodium nuclei remains constant over the whole range of x with a value of 20% if the FID satellites do not contribute to resonance, and a value of 9% if they do. Since it is probable that some FID nuclei have satellites inside and others outside the B_1 field, then the true ratio is probably somewhere between 9% and 20%.

There are two basic models to explain these properties. The first is a cluster type model proposed by Fromhold and Narath¹²⁴ and developed by Webman, Jortner and Cohen⁵⁴, while the second involves a random Sodium distribution accompanied by displacements of the Oxygen atoms. We shall show that our data provides new evidence for disregarding the first model while supporting the second.

1. The Cluster Model

Fromhold and Narath¹²⁴ calculated the field gradient at the Sodium nucleus due to a single nearest neighbour Sodium vacancy to be $5.06 \times 10^{19} \text{ V/m}^2$ giving a first order satellite separation of 338 KHz, and a second order linewidth of 6.6 KHz, with two or more vacancies producing larger gradients. Hence they assumed that all the FID sites must have all nearest neighbour Sodium sites either filled or empty. For $x \approx 0.5$, the number of those nuclei becomes vanishingly small if the FID sites are assumed to be randomly dispersed. Since experimentally the number of FID sites remains constant, Fromhold and Narath proposed that clustering of the Sodium atoms into local $x = 1$ regions occurred, with the FID signal coming from Sodium nuclei inside these regions. Hence the FID T_2 would be independent of x and would have a value close to the dipolar T_2 for $x = 1$, which is in excellent agreement with our results. The Echo signal comes from those Sodium nuclei which are positioned randomly outside the clusters. Their central transitions are broadened in second order by the field gradients produced by nearest neighbour vacancies. Since the Echo nuclei are randomly dispersed, the Echo T_2 should have the $x^{-\frac{1}{2}}$ dependence which again is in excellent agreement with our data. Moreover the cluster model has been used to obtain an excellent fit to the transport data. However the agreement between this model and experiment seems to be confined to these points.

Our Sodium spin-lattice relaxation rates show the x^2 dependence for $x > 0.35$ arising from the dependence of the density of states at the Fermi surface on x . This does not lend support to the cluster model in which the relaxation rate would be independent of x . The cluster model should also predict different relaxation rates for Tungsten nuclei inside and outside clusters, with the rate for those inside clusters being independent of x . However Weinberger¹²⁸ has found a single relaxation rate proportional to x^2 .

Bonera et al⁹⁴ have criticised the calculation of the field gradient produced by a Sodium vacancy. They show that if screening by the conduction electrons is considered, the field gradients are an order of magnitude smaller than those given by Fromhold and Narath. This gives a quadrupole interaction large enough to shift the satellites by tens of Gauss, but has a negligible effect in second order on the central transition. Bonera et al also point out that the non-uniform nature of the 5d wavefunctions may reduce the field gradient even further. We add to this the comment that, as can be seen from Fig. 5.4a, the 5d wavefunctions have considerable overlap around the face centres of the unit cell. This high electron concentration is between adjacent Sodium sites and hence may further reduce the field gradients due to vacancies.

Additional evidence that vacancies do not produce large enough field gradients to produce the Echo is provided by the pressure dependence of the Echo width. For a single vacancy a distance a away, the field gradient V_{zz} neglecting screening can be written as

$$V_{zz} = \frac{2q}{4\pi\epsilon_0 a^3} \quad (7.1)$$

and hence changing a by Δa by pressure gives

$$\frac{\Delta V_{zz}}{V_{zz}} = \frac{3\Delta a}{a} \quad (7.2)$$

From section 6.1 we have $\Delta a/a = 1.1 \times 10^{-3}$. The Echo width W is proportional to V_{zz}^2 and hence

$$\frac{\Delta W}{W} \approx 2 \frac{\Delta V_{zz}}{V_{zz}} \quad (7.3)$$

Hence with 4 K Bar we would expect the Echo width to change by 0.7%. The actual change is about 15% and so we are forced to look elsewhere for the origin of the field gradients.

Bonera et al⁹⁴ have found that the Echo width increases with temperature until at about 400 K, the Echo signal disappears, and all nuclei are in the FID. They interpret this as a phase transition involving the Oxygen octahedra. To explain this in the context of a cluster model, it is necessary to suppose that as the temperature increases, diffusion of the Sodium ion averages out the field gradients. However the measured diffusion constant is not large enough for this to occur at 400 K. If large clusters exist, then a local $x = 1$ region should have a lattice constant of 3.866 \AA and the Sodium free region 3.7845 \AA . Hence a doublet should be observed in the x ray spectrum. Instead only narrow singlet lines are obtained. Photoemission spectra¹⁰⁴ show that as x increases the conduction band is gradually filled up by electrons which would not occur if the electrons existed solely in local $x = 1$ regions. Finally, the Kohn anomaly work¹⁰⁶ has shown that the radii of the Fermi surface cylinders decreases as x decreases. If all the nuclei were in local $x = 1$ regions however, the radii would be independent of x .

2. Oxygen Displacement Model

Evidence that displacements of the Oxygen atoms from their regular positions occur in many perovskites and indeed in other Tungsten bronzes⁸⁸ has led to speculation that such displacements may be responsible for the peculiar quadrupolar spectrum of Sodium Tungsten bronze. X ray work has so far failed to determine any displacements, but neutron diffraction data of Atoji and Rundle⁹² suggest that at $x = 0.75$ the unit cell is octupled in volume with the Sodium sites at $(\frac{1}{4}, \frac{1}{4}, \frac{1}{4})$ and $(\frac{3}{4}, \frac{3}{4}, \frac{3}{4})$ in the enlarged cell vacant. In addition, to generate the lattice constant doubling, the Oxygens are displaced towards or away from the Sodium sites.

Oxygen displacement in the bronzes is determined by the binding energy and the atomic size of the constituents. The former determines the atomic positions and hence the size of the unit cell, while as we shall show below, the latter can give some indication of what type of displacements may occur. Assuming full ionicity, we can use the following ionic radii⁸⁸

Na^+	0.96 Å
O^{2-}	1.35 Å
W^{6+}	0.62 Å
Re^{6+}	0.52 Å

These figures are only approximate, but we see that the $x = 1$ lattice constant of 3.866 Å for Sodium Tungsten bronze is less than the W-O-W cube edge of 3.94 Å predicted above. However ReO_3 with a lattice constant of 3.75 Å can just accommodate Re-O-Re along a cube edge. There is evidence from NMR work¹³⁷ that ReO_3 does not suffer from Oxygen displacements. Also the O-Na-O length of 5.467 Å is larger than the 4.62 Å predicted from above, and so in Sodium Tungsten bronze, the Oxygens have some room to bend towards or away from the

Sodium site so as to reduce the predicted lattice constant to a value approaching that of the measured one.

Megaw⁸⁸ has treated the Oxygen displacements in ABO_3 compounds in terms of three different types of motion.

- (a) The Oxygen octahedra may be distorted in shape, becoming for example a tetragonal bipyramid. This is most common in systems where the B cation experiences non-octahedral covalent bonding, or where the A cation is covalently bonded.
- (b) The B cation may be displaced from the centre of its octahedron. This is most common when B is too small for its surrounding Oxygens.
- (c) The Oxygen octahedra may remain regular, but may tilt relative to one another, hence reducing the size of the A cavity. This is most common when the A cation is too small. Tilting may occur about any axis or all three at once, and may be accompanied by the other two mechanisms.

We now consider three actual models for the Oxygen displacements in Na_xWO_3 .

The first model uses to a large extent the data of Atoji and Rundle⁹². Tunstall⁹⁵ proposed that the Oxygen atoms are displaced in such a way as to retain a cubic nearest neighbour environment at the $(\frac{1}{4}, \frac{1}{4}, \frac{1}{4})$ and $(\frac{3}{4}, \frac{3}{4}, \frac{3}{4})$ sites, while the other six sites in the enlarged unit cell are in a non-cubic Oxygen environment. If these two sets of sites are populated randomly, then there should be three times more Echo nuclei than FID nuclei. Tunstall's data supports this ratio if the FID nuclei are assumed to retain their satellites. However as we have shown in section 6.5, this data is subject to uncertainty arising from the problem of defining the $\pi/2$ pulse. Moreover, if ordering of the Sodium atoms as proposed by Atoji and

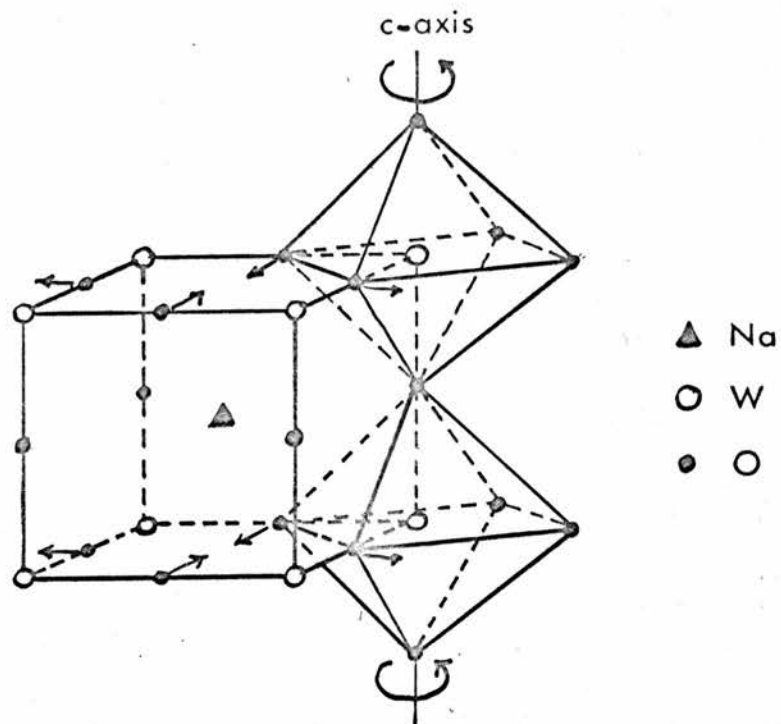


FIG 7.1

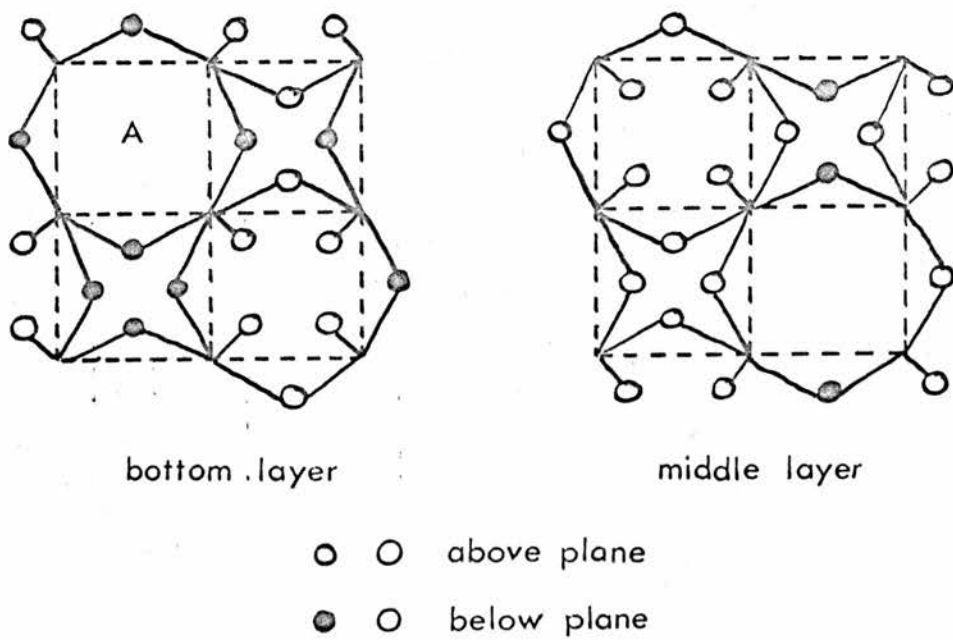


FIG 7.2

FIG. 7.3

Computer calculation of field gradients and quadrupolar coupling constants for different Oxygen displacements h where h is a fraction of the half lattice constant. The results below are for $x = 0.35$ and hence h is the fraction of 1.9066 \AA by which the Oxygens are moved from their cubic positions.

h	$V_{zz} \times 10^{-19} \text{ V/m}^2$	$\nu_Q \text{ MHz}$
0.02	7.38	0.49
0.04	14.59	0.98
0.06	21.59	1.45
0.08	28.43	1.91
0.10	35.05	2.25
0.12	41.45	2.78
0.14	47.65	2.19
0.16	53.63	3.59
0.18	59.39	3.98
0.20	64.92	4.35

V_{zz} was calculated without the anti-shielding factor γ whereas ν_Q was calculated from V_{zz} with $\gamma = 4.53$.

Rundle does occur at $x = 0.75$, then around this value the FID signal should disappear. There is no evidence of this occurring.

The second model was proposed by Borsa¹²⁷, and is based on a tilting of the Oxygen octahedra. From the work of Bonera et al⁹⁴, it was found that above about 400K, Na_xWO_3 has the ideal cubic perovskite structure, but at lower temperatures it undergoes a structural transition to a non-cubic phase. In this non-cubic phase the quadrupole coupling constant (qcc) follows a temperature dependence of the type $(T_0 - T)^{\frac{1}{2}}$ where T_0 is the structural transition temperature. Borsa infers that if the order parameter is the octahedra tilting angle, then the qcc ν_Q is linear in the order parameter. Hence the tilting system is as shown in Fig. 7.1 where neighbouring octahedra in the c direction are rotated in the same direction. If the angle of tilt is ϕ then

$$\nu_Q \approx 9\phi \quad \text{MHz} \quad (7.4)$$

Since, as has already been shown, the qcc increases with decreasing temperature, then the octahedra rotate more as the temperature is lowered. Borsa estimates a tilt of 4° at room temperature increasing to 7° at 100K. Our main criticism of this model is that it fails to explain the FID signal since it predicts a non-cubic environment for all sites. One would have to assume that pockets of ideal cubic structure exist below the phase transition. Not only is this unlikely from a theoretical viewpoint, but also the ratio of FID to Echo nuclei would presumably be x dependent, and would also depend on the thermal history of the sample. The constancy of this ratio however leads us to believe that the FID sites should be included as part of a regular structure.

We propose a third model based on our own data. As has already been stated, the ratio of the FID nuclei to the total number of nuclei

is between 9% and 20%. Assuming that about half the FID nuclei contribute their satellites to the signal, this ratio becomes 12.5% and hence there are seven Echo nuclei to every one FID nucleus. If we take the Atoji and Rundle⁹² enlarged unit cell, then one site may contain a FID nucleus while the other seven may be Echo sites. The only nearest neighbour Oxygen arrangement which can retain cubic symmetry at the Sodium nucleus involves all the Oxygens bent towards the Sodium, or all bent directly away from it. Starting from the subcell A in Fig. 7.2 which has cubic symmetry with all the Oxygens bent away from the Sodium, then the enlarged unit cell can be built up as shown, to produce non-cubic symmetry at the other seven subcell Sodium sites. Hence this model involves both tilting and distortion of the Oxygen octahedra. However one would not expect distortion to occur since the Tungsten can bond octahedrally and there is no evidence of any covalent bonding to the Sodium. Hence on these intuitive grounds it seems that Borsa's model¹²⁷ compares better with other systems. However it is possible that the non-stoichiometric nature of the system may cause distortion of the octahedra.

We shall now try to show that the Oxygen displacement model is capable of producing the Echo data. Since in Fig. 7.2 each of the Echo sites has a different nearest neighbour environment, we immediately have a mechanism to explain the distribution of quadrupolar coupling constants necessary to explain the absence of Echo structure. We assume that the central line of the Echo nuclei has a width of approximately $25/9$ A where from equation (2.50)

$$A = \frac{3}{16} \frac{v_Q^2}{v_L} \quad (7.5)$$

where v_Q is some sort of average qcc and v_L is the Larmor frequency. A is calculated from the Echo width at half maximum Δt by using equation (2.53)

$$\frac{25}{9} 2\pi A = \frac{8 \ln 2}{\Delta t} \quad (7.6)$$

For the $x = 0.35$ sample, using the experimental Echo width, this gives a value for the qcc of $\nu_Q = 0.92$ MHz.

We have estimated the qcc for a typical Echo site using a point charge model. As a typical nearest-neighbour Oxygen environment, four Oxygens were assumed to bend towards the Sodium, and the remaining eight away from it. The electric field gradient at the Sodium site produced by a charge of $2-$ on each of these Oxygens was calculated by a method given by Cohen and Reif⁶. The field gradient produced by an ion of charge Ze a distance r away can be written as

$$V_{ij} = r^{-5} (3x_i x_j - r^2 \delta_{ij}) \frac{Ze}{4\pi\epsilon_0} \quad (7.7)$$

The total field gradient, obtained by summing V_{ij} for all twelve Oxygens, was calculated by a computer, and was shown to be cylindrical. Hence V_{zz} is the only component required and it is tabulated in Fig. 7.3 against h , which is the fraction of the $W-O$ distance by which the Oxygens move from their ideal cubic positions. The qcc was also calculated from

$$\nu_Q = \frac{eQ V_{zz}}{2h} (1 + \gamma) \quad (7.8)$$

where γ was taken to be 4.5, and Q is 10^{-29} m^2 . If we neglect any screening of the field gradient by the conduction electrons, then our measured value of $\nu_Q = 0.92$ MHz implies that the Oxygen atoms are displaced by about $0.04 \times 1.9066 \text{ \AA}$. Screening by the conduction electrons will presumably not be as efficient for field gradients produced by the Oxygen ions as for those due to Sodium vacancies since there is no large conduction electron density between Oxygen and Sodium sites. If we assume a reduction of the field gradient by a factor of

5 for screening of the Oxygen (Bonera et al⁹⁴ obtained factors greater than 10 for screening of Sodium vacancies) then we can get an upper limit for Oxygen displacement of about $0.2 \times 1.9066 \text{ \AA}$. Hence we propose that the Oxygens are displaced by a distance between 0.04 and 0.2 times the W-O spacing. If this was generated purely by octahedral tilting, it corresponds to tilt angles between 2° and 11° which encompasses Borsa's values¹²⁷. We note that 11° tilts of the octahedra have been observed by x rays in H_xWO_3 ⁹¹. The lack of any x ray evidence of tilting in Na_xWO_3 may not be because the tilts are too small, but may be because they are accompanied by distortions of the octahedra which may smear out any structure in the x ray line.

To conclude our discussion on these particular models, we affirm that although Oxygen displacement almost certainly occurs, we cannot as yet present a definite structure for Na_xWO_3 incorporating it. What may be required is some high resolution x ray work or more exhaustive neutron diffraction. However if we assume that displacements do occur, we can explain in a general way most of the NMR data. This we shall proceed to do in the rest of this section.

The Echo width has a broad maximum around $x = 0.5$. This may either be caused by a minimum in the quadrupole coupling constant ν_Q , or by a minimum in the distribution of ν_Q values. We can think of no mechanism which would cause the latter, and indeed it would seem possible that around $x = 0.5$, there may be a maximum in the coupling constant ^{distribution} due to a maximum in the number of different surrounding Sodium configurations. There is also some evidence that instead there is a minimum in ν_Q . Firstly it has been shown in section 5.6 that there is a discontinuity in the thermal expansion¹¹⁶ and thermal conductivity¹¹⁷ coefficients which occurs at a temperature T_S , which is between 400 and 500K. We assume that a transition occurs at T_S from the phase involving Oxygen displacement to the high temperature pure cubic phase. This is

supported by Bonera et al⁹⁴ who find that above T_S the Echo signal disappears. The transition temperatures for the thermal data and the NMR data are very similar. A further indication of such a transition is provided by the thermal expansion coefficient¹¹⁶, which jumps from $12 \times 10^{-6} \text{ K}^{-1}$ to $5 \times 10^{-6} \text{ K}^{-1}$ on going into the high temperature phase, indicating that the high temperature phase may be harder to compress. There is no data on the compressibility of the pure cubic phase of Na_xWO_3 above the transition, but a similar cubic system, ReO_3 , has a compressibility of $5.3 \times 10^{-4} \text{ K Bar}^{-1}$ ¹⁵⁷ compared to that of the low temperature phase of Na_xWO_3 of $8.2 \times 10^{-4} \text{ K Bar}^{-1}$. Hence it seems that the cubic system may be more difficult to compress than the distorted system.

The transition temperature for the thermal expansion¹¹⁶ is shown in Fig. 5.10 and exhibits a broad minimum around $x = 0.5$. The thermal conductivity¹¹⁷ and NMR data⁹⁴ show the same x dependence on the high x side of the minimum, but unfortunately do not include samples on the low x side. The NMR data shows that as the temperature is increased, the Oxygen displacements decrease, until at T_S , the system becomes pure cubic. We propose that a minimum in T_S implies that a minimum occurs in the energy required to drive the system cubic, and this in turn implies a minimum in the Oxygen displacement. Hence we have a minimum Oxygen displacement around $x = 0.5$ which manifests itself in a minimum in the quadrupolar coupling constant ν_Q . This is in excellent agreement with our results on the x dependence of the Echo width. We also connect this with the experience that it seems to be easiest to grow single crystals of Na_xWO_3 with x values around 0.5. Oxygen displacements may make the structure less stable.

The reasons for the minimum in ν_Q are not immediately obvious. We propose that two competing mechanisms are present, one occurring over the whole range of x , while the other only becomes important at

high x where it dominates over the first. The first mechanism is the decrease in lattice constant as x decreases. If the O-W bond length remains constant then this will cause increased Oxygen displacement. Considering the $x = 0.35$ sample, we have an Echo width of 100 μs . With this same sample at 4 KBar, the Echo width is 85 μs . But we have shown that 4 KBar reduces the lattice constant by a similar amount to that obtained by reducing x by 0.05. The Echo width for the $x = 0.30$ sample is 83 μs and hence we can assume that the increase in ν_Q as x decreases on the low x side of the minimum is due to lattice contraction. Further evidence for this is supplied by Fig. 7.3. Taking $x = 0.35$, with a half lattice constant of 1.9066 \AA and a measured ν_Q of 0.92 MHz, we assume that screening reduces the calculated ν_Q in Fig. 7.3 by a factor of 3. Hence the Oxygen is displaced from its pure cubic site by $0.12 \times 1.9066 \text{\AA}$. This gives a W-O bond length of 1.9202 \AA . Considering now the $x = 0.30$ sample where the half lattice constant is 1.9045 \AA , the same W-O spacing as above gives an Oxygen displacement of $0.13 \times 1.9045 \text{\AA}$. This gives a calculated ν_Q of 2.99 MHz which reduces to about 1 MHz if screening is considered. This compares reasonably well with the measured value of 1.02 MHz for the $x = 0.30$ sample.

The second mechanism involves some sort of interaction between the Sodium and Oxygen atoms. Above the minimum in ν_Q the lattice contraction mechanism still holds since the pressure dependence of the Echo width is the same on both sides of the minimum. However another mechanism, possibly driven by the increase in x , must oppose this at high x . We speculate that some strong Sodium-Oxygen electrostatic interaction may be responsible for large displacements of the Oxygen atoms. This interaction would be smaller at low x due to the reduction in the number of Sodium atoms, and hence might give way to the lattice contraction mechanism below $x = 0.5$. We note that the

lattice contraction involves the W-0 distance remaining fixed, whereas this latter mechanism must involve stretching of this distance.

Finally we compare lattice compression with pressure to that obtained by reducing the temperature. Bonera et al⁹⁴ have shown that as the temperature is lowered, ν_Q increases. At low temperatures they find that

$$\frac{\partial \nu_Q}{\partial T} \approx 1.3 \times 10^{-3} \text{ MHz/K} \quad (7.9)$$

and this is independent of x for the three samples studied. But we have

$$\frac{\partial \nu_Q}{\partial T} = - \frac{\partial \nu_Q}{\partial a} \frac{\partial a}{\partial T} \quad (7.10)$$

where a is the lattice constant. $\partial a/\partial T$ is the coefficient of thermal expansion which has also been shown to be independent of x . Hence we obtain a value

$$\frac{\partial \nu_Q}{\partial a} \approx 28 \text{ MHz/\AA} \quad (7.11)$$

and this is independent of x . But we also have

$$\frac{\partial \nu_Q}{\partial P} = - \frac{\partial \nu_Q}{\partial a} \frac{\partial a}{\partial P} \quad (7.12)$$

We have found that $\partial \nu_Q/\partial P$ is relatively constant over most of the range of x studied, with a value of about 0.017 MHz/K Bar. Since we already have $\partial \nu_Q/\partial a$ independent of x then immediately it follows that $\partial a/\partial P$ is constant over most of the x range studied. Since $\partial a/\partial P$ can be obtained from the compressibility, then our assumption in section 6.1, that the compressibility remains constant over most of the x range, seems justified. Using the compressibility, we get

from the pressure results

$$\frac{\partial \nu_Q}{\partial a} = 60 \text{ MHz/\AA} \quad (7.13)$$

The difference between this value and that of equation (7.11) may be due to the fact that some of the differentials are measured at different temperatures. The Echo width does not change much with pressure for the $x = 0.22$ and 0.84 samples. The $x = 0.22$ sample is very close to the structural transition and hence the compressibility may be quite different from the rest of the range of x . However it is not clear why the 0.84 sample has a smaller pressure dependence.

7.2 Spin-Lattice Relaxation and the Knight Shift

For the purpose of discussion of the spin-lattice relaxation rates and the shift measurements, we shall divide the range of x values studied into three regions. The first is the high x region which consists of the samples with $x \geq 0.35$. The second region is the enhancement region and consists of samples with $x < 0.35$, for which enhancements are found in the relaxation rates. The final region consists of the $x = 0.22$ sample, which exhibits some anomalous behaviour and as already noted is close to the metal non-metal transition.

7.2.1 The High x Region

For $x \geq 0.35$ it can be seen from Fig. 6.7 and Fig. 5.14 that $T_1^{-1} \propto x^2$ for both the Sodium and Tungsten resonances. Also the Tungsten Knight shift is negative and is proportional to x in this region, and there are indications that the Sodium Knight shift may also follow this relationship down to $x = 0.57$. These results, taken with the specific heat and susceptibility data¹¹⁴, provide evidence that the conduction band in this region is derived from

Tungsten 5d orbitals with the density of states given by

$$N(E) = A e^{E/E'} \quad (7.14)$$

Hence in this region we propose a rigid conduction band which is filled by electrons as x increases.

The Korringa products for the Tungsten resonance¹²⁸ in this region can be seen from Fig. 6.15 to be relatively independent of x , and have values around $50 \times 10^{-6} \text{ s } ^\circ\text{K}$. If this product is calculated from equation (2.38), a value of $155 \times 10^{-6} \text{ s } ^\circ\text{K}$ is obtained, assuming purely s contact. However the dominant interaction must be core polarisation by Tungsten 5d states since the Knight shift is negative, and hence the calculated product above must be modified as in equation (2.39) to account for the degeneracy of the electronic wavefunctions. This can give products ranging from $310 \times 10^{-6} \text{ s } ^\circ\text{K}$ to $775 \times 10^{-6} \text{ s } ^\circ\text{K}$ depending on the particular admixture of Tungsten t_{2g} and e_g orbitals chosen for the conduction band. Fromhold and Narath¹²⁵ have proposed that the discrepancy between the measured and calculated values indicates a partial cancellation of the negative core polarisation shift by the positive term arising from the orbital interaction and also from some s character at the Fermi surface. They assume that the hyperfine fields due to s contact, core polarisation and orbital interactions are in the ratio of 10:1:1.5, which is a relationship reasonably well obeyed in a number of transition metals. Then by considering the estimated s contact field for Tungsten metal, they are able to evaluate the other two hyperfine fields, and eventually conclude that the amount of s character at the Fermi surface is about 6%.

For the Sodium resonance, we can calculate $K^2 T_1 T$ from equation (2.41)^{2.39} to be about $11 \times 10^{-6} \text{ s } ^\circ\text{K}$, assuming that the Fermi surface is composed of Tungsten t_{2g} orbitals which interact with the Sodium

nuclei solely by the core polarisation mechanism. For $x > 0.57$, the experimental values of Fig. 6.15 can be seen to be approximately double this value. This indicates that the competing mechanisms found in the Tungsten resonance are not present. This is to be expected since if the conduction band consists of Tungsten orbitals, there will be no contact field at the Sodium nucleus, and only a very small orbital field. The Sodium Korringa products for the $x = 0.40$ and $x = 0.35$ samples are much larger than the higher x samples. Although T_1^{-1} for these two samples lies on the x^2 line, the Knight shifts have become larger. Since no discrepancies are found in the susceptibility or Tungsten data, any electron-electron correlation is probably ruled out. We cannot as yet explain the reason for this increase in the Korringa product.

Finally we shall comment on the statement made in section 6.7 that the Echo T_1 is slightly shorter than that of the FID. Although for most of the samples, the two are within the experimental error, the fact that the Echo T_1 is consistently shorter than the FID leads us to believe that the effect is significant. Returning to the model of Oxygen distortion, it was stated that the Echo sites have a different nearest neighbour Oxygen configuration from the FID sites. Hence we propose that since the conduction band involves some Oxygen character, the Echo nuclei will experience a different hyperfine field from the FID nuclei. In our model in section 7.1, the FID nuclei have all the Oxygens bent away which may result in a smaller hyperfine field. If also the dipolar interaction between FID and Echo nuclei is not effective in producing a common spin temperature, due to the quadrupolar interaction making the Echo nuclei effectively "unlike" the FID nuclei, then we have a mechanism capable of producing a shorter Echo T_1 .

7.2.2 The Enhancement Region

The region $x < 0.35$ is characterised by an enhancement in the Sodium spin-lattice relaxation rate of the order of 40, accompanied by a slight increase in the Knight shift. The Tungsten resonance¹²⁸ displays a slight decrease in the spin-lattice relaxation rate, accompanied by a precipitous drop in the Knight shift. The net result is that the Korringa products for both resonances fall by an order of magnitude in going through this region.

The large enhancement in the Sodium relaxation rate accompanied by the small Tungsten enhancement leads one to suggest that the Sodium nuclei become coupled to a dynamic electric quadrupole field produced by the motion of the conduction electrons. The Tungsten nuclei do not experience this interaction since they have no quadrupole moment. However, as Weinberger has pointed out¹²⁸, the relaxation rate due to this mechanism is vanishingly small, since the Sodium nucleus has a large magnetic moment but a relatively small quadrupolar moment. Another mechanism which might be important is relaxation to paramagnetic centres, caused either by an increased impurity concentration or by partial electron localisation. However this type of relaxation is relatively temperature independent, whereas all the relaxation rates are directly proportional to temperature. Indeed this temperature dependence leads us to propose that the dominant relaxation process in both the high x region and enhancement region is via magnetic coupling to the conduction electrons. Hence it seems that the enhancement must be due to a change in the character of the electron wavefunctions and/or a change in the electron dynamics.

The first of these two mechanisms was put forward by Tunstall⁹⁵ in the form of an overlapping band approach. At high x , the Sodium 3s and 3p bands lie above the conduction band, but as x decreases, the corresponding reduction in the lattice constant may shift the relative

position of these bands downwards so as to produce some admixture of Sodium 3s or 3p into the states at the Fermi level. This would result in an increased hyperfine field at the Sodium nuclei, and hence an enhanced relaxation rate. Tunstall proposed that 6% Sodium 3s character would provide the requisite enhancement if it was combined with about 15% 3p character to keep the Knight shift negative.

There are three possible types of Sodium states which may mix into the conduction band i.e. 3s, 3p and 3d. We shall estimate the hyperfine field for each of these states and hence calculate the relaxation rates and Knight shifts. To do this we require the density of states per unit cell, which can be found from the specific heat data¹¹⁴ assuming that it is proportional to x

$$\Omega\rho(E_F) = 5.18 \times 10^{18} x \quad (7.15)$$

The magnetic spin susceptibility per unit cell $\Omega\chi_s$ can now be calculated from equation (2.21) to be

$$\Omega\chi_s = 1.12 \times 10^{-33} x \quad \text{MKS units} \quad (7.16)$$

Sodium 3s

Weinberger¹²⁸ has derived from atomic beam data that the contact hyperfine field at the Sodium nucleus due to a single 3s electron is 28 T. For 3s character, the contact interaction is dominant and hence the other mechanisms discussed in Chapter 2 may be neglected. If we assume that δ_s is the fraction of 3s character at the Fermi surface, then from equations (2.23) and (2.33)

$$\begin{aligned} K(s) &= 2.69 \times 10^{-3} x \delta_s \\ \frac{1}{T_1}(s) &= 8.12 x^2 \delta_s^2 \quad \text{at 4.2 K} \end{aligned} \quad (7.17)$$

Sodium 3p

Weinberger¹²⁸ has derived the core polarisation hyperfine field due to a single p electron by taking values of $|\psi_{cp}(0)|^2$ obtained from unrestricted Hartree-Fock calculations. These showed that polarisation of the 1s shell is opposite in sign to that of the 2s shell, and partly cancels it. The hyperfine field is -0.23 T and gives

$$\begin{aligned} K(p)_{cp} &= -2.21 \times 10^{-5} \times \delta_p \\ \frac{1}{T_1}(p)_{cp} &= 1.83 \times 10^{-4} \times \delta_p^2 \quad \text{at 4.2 K} \end{aligned} \quad (7.18)$$

The orbital hyperfine field has been calculated from atomic beam measurement of $\langle r^{-3} \rangle$ to be 2.2 T. The relaxation rate, when combined with the dipolar relaxation rate which is of the order of 3/10 that of orbital rate produces a relaxation rate

$$\frac{1}{T_1}(p)_{\text{orb+dip}} = 1.44 \times 10^{-2} \times \delta_p^2 \quad \text{at 4.2 K} \quad (7.19)$$

The dipolar interaction does not contribute to the Knight shift since the system is cubic, and the orbital interaction only contributes through the Van Vleck susceptibility which is difficult to determine. However since the Fermi level lies in the band tail, it is likely that this susceptibility is small enough for the orbital shift to be neglected.

Sodium 3d

Since no information on hyperfine fields could be found in the literature for a 3d electron, we have estimated them by comparison with other systems. Hence the following calculations can only be regarded as approximate. Taking the ratio of 10:1:1.5 for the s contact, core polarisation and orbital fields¹²⁵ we have 2.8 T for the core polarisation field and 4.2 T for the orbital. At high x, we

have assumed that both T_1 and K arise from core polarisation by the Tungsten 5d electron. If the conduction band is composed entirely of t_{2g} orbitals, the hyperfine field can be calculated to be 0.8 T. for a d orbital centred on a Sodium site, this may be larger since the electron will be closer to the Sodium nucleus. Hence it seems that 2.8 T may not be a bad estimate of the core polarisation hyperfine field. This gives

$$\begin{aligned} K(d)_{cp} &= 2.69 \times 10^{-4} \times \delta_d \\ \frac{1}{T_1}(d)_{cp} &= 8.12 \times 10^{-2} \times \delta_d^2 q \end{aligned} \quad (7.20)$$

where q is the degeneracy factor defined in chapter 2. The orbital hyperfine field can also be estimated from that already calculated for the p electron. Kopfermann shows that¹⁵⁸

$$\langle r^{-3} \rangle \propto \frac{1}{(\ell + \frac{1}{2})(\ell + 1)} \quad (7.21)$$

where ℓ is the orbital quantum number. Taking the p orbital field as 2.2 T this gives a d orbital field of about 0.9 T. Hence it would seem that the ratio given by Fromhold and Narath¹²⁵ is too large. If we take this field to be ≈ 1 T then

$$\frac{1}{T_1}(d)_{orb+dip} = 1.03 \times 10^{-2} \times \delta_d^2 p \quad (7.22)$$

where p is the degeneracy factor. Making the same assumptions as before, we shall neglect the orbital shift.

We shall now attempt to quantify what enhancements in the relaxation rate might be produced by the Warren²¹ mechanism of chapter 2. We have already shown that the conductivity data indicates that the region below $x = 0.35$ is characterised by diffusive type motion of the conduction electrons. In this region, the jump distance will be of the order of the lattice spacing a , and hence

equation (2.44) will reduce to

$$\eta = \frac{e^2 \rho}{3ha} \quad (7.23)$$

With the resistivity of the $x = 0.25$ sample as $8 \times 10^{-6} \Omega\text{m}$ and the lattice constant as 3.805 \AA , then enhancements of the order of two are predicted.

Having established these values, we shall now consider which of these mechanisms or mixture of these mechanisms best fits the available experimental data. Tunstall⁹⁵ and Weinberger¹²⁸ have both proposed that the enhancement of the relaxation rate is due to the Sodium 3s states, lying high above the conduction band at high x , being driven down as x decreases, so that the Fermi level acquires some 3s character. For the $x = 0.25$ sample, 9% Sodium 3s character can account for the measured enhanced relaxation rate. However 9% 3s character produces a Knight shift of +60 ppm, which does not agree with the measured value of -54 ppm. To counter this, Tunstall⁹⁵ proposed that the addition of about 15% 3p character might cancel the 3s shift and also provide an extra relaxation mechanism. Unfortunately from equation (7.18) we find that even 100% 3p character can only produce a shift of -10 ppm and hence it seems unlikely that cancellation could occur. Sodium 3d character is much more promising since the core polarisation hyperfine field is greater, but to cancel the +60 ppm of the 3s character we still require about 100% 3d character. In short, the conclusion must be reached that 3s character is not the dominant mechanism responsible for the relaxation rate enhancement, since if it were, no other mechanisms would be strong enough to cancel the resultant positive shift.

Weinberger¹²⁸ has also explored the possibility that 3p character might be responsible for the relaxation rate enhancement. However 100% 3p character can only produce a relaxation rate of $0.9 \times 10^{-3} \text{ s}^{-1}$

at 4.2 K compared to the measured value of $3.9 \times 10^{-3} \text{ s}^{-1}$. Weinberger disregards the Warren mechanism since he cannot find any evidence for enhancement in the Tungsten relaxation rates. By assuming a loss of about 20% Tungsten 5d character accompanied by a gain of 6% Tungsten 6s character, he can explain his Tungsten data. Unfortunately with such a small transfer to Sodium character, the Sodium enhancement can only be produced if this transfer is to 3s, and hence we are back to the problem with the Knight shift.

We propose the following model for the enhancement region which is based on the concept of large transfer of character to the Sodium, combined with a Warren mechanism. Briefly, we propose that the large transfer from the Tungsten 5d character is to Sodium 3d character. The larger hyperfine field than 3p enables us to explain the Sodium relaxation rate enhancements if a Warren mechanism is included. Moreover the increased core polarisation field at the Sodium nucleus will keep the Knight shift negative. If there is a large loss of Tungsten character, the Tungsten relaxation rate and Knight shift should drop. However the Warren mechanism may enhance the relaxation rate so that it exhibits only a small decrease compared to the precipitous drop in the Knight shift. We shall now consider this in more detail, and then consider the feasibility of such a model.

Suppose we start with the Tungsten resonance, and extrapolate the high x data down to $x = 0.25$ to obtain $T_1 = 15.8\text{s}$ and $K = -0.079\%$ compared to the measured values of $T_1 = 14\text{s}$ and $K = -0.046\%$. Assuming that the reduction in K is due to the transfer of a fraction x of the wavefunction character away from Tungsten 5d, then x may be estimated. The situation is complicated by the fact that the orbital centred on the Sodium site will produce a hyperfine field at the adjacent Tungsten site. By analogue with our calculations on the Sodium 3d hyperfine fields, we estimate that the core polarisation field due to

an electron on an adjacent site is approximately $\frac{1}{4}$ that due to an electron on that particular site. Hence

$$(1-x)(0.079) + \frac{1}{4}x(0.079) = 0.046$$

$$x = 0.56$$

Also an electron on the Sodium will produce about $1/16$ of the relaxation rate from that on the Tungsten site. Hence the relaxation rate for the Tungsten nuclei of the $x = 0.25$ sample at 4.2 K should be

$$(1-x)(0.063) + \frac{1}{16}x(0.063) = 0.03$$

$$\text{or } T_1 = 33\text{s}$$

But the measured T_1 is only 14s and hence we can postulate a Warren enhancement factor

$$\eta(\text{Tungsten}) = 2.4$$

Moving on to the Sodium resonance, we assume that the 56% transfer is to Sodium 3d character. If we take the degeneracy factors $q = 1/3$ and $p = 2/9$ corresponding to only t_{2g} orbitals at the Fermi surface, then the total relaxation rate at 4.2 K for the $x = 0.25$ sample should be

$$\frac{1}{T_1} = 1.03 \times 10^{-3} \text{ s}^{-1}$$

compared with the measured rate of $3.9 \times 10^{-3} \text{ s}^{-1}$. The difference may be explained by introducing a Warren mechanism with the enhancement factor

$$\eta(\text{Sodium}) = 3.8$$

The Sodium Knight shift is composed of two parts. The 56% 3d character produces a shift of -37 ppm while the remaining Tungsten 5d

character gives -8 ppm. This gives a total shift of -45 ppm for the $x = 0.25$ sample which is in relatively good agreement with the measured shift of -54 ppm.

Hence a transfer of about 56% of the Tungsten 5d to Sodium 3d character at the Fermi surface can explain the Tungsten Knight shift and the Tungsten and Sodium relaxation rates, provided some Warren enhancement is included. Although the enhancements required for the $x = 0.25$ sample are higher than those predicted from the conductivity data, in view of the approximate nature of the calculations, the agreement is reasonably good. There is a difficulty in explaining the Sodium Knight shift, since although this model predicts a small increase in the shift in the enhancement region, Fig. 6.14 shows that the increase starts at higher x values than those at which the relaxation rate enhancement starts. Also the two lowest x samples show a slight decrease again in the shift. The decrease at low x may be connected with the approach to the metal non-metal transition, but the increase at higher x is difficult to explain.

The main difficulty with this model must lie in whether there is any physical justification for assuming that Sodium 3d character occurs in preference to 3s or 3p. The assumption that 3s character may be minimal is surprising in view of the fact that in the isolated Sodium atom, the 3s level lies about 2 eV below the 3p level. However each Sodium atom in the bronze is surrounded by twelve Oxygens which form centres of negative charge. An electron on a Sodium site might then favour an orbital poking in the direction of the Tungstens such as a p or d orbital, rather than pay the energy required to overcome the repulsion which would occur between the Oxygen and the spherically symmetric s orbital. Indeed in the early work on the bronzes, before Tungsten 5d character at high x had been generally accepted and it was thought that the conduction band contained Sodium

character, this interaction was invoked to explain why the Fermi surface involved 3p character rather than 3s which could not explain the negative Knight shift⁹⁷. It is not obvious however whether this interaction would differentiate between 3p and 3d orbitals, nor can we propose any other mechanism which would cause 3d states to be lower in energy than 3p. In view of this, and also because our estimates of the 3d hyperfine fields may only be approximate, we can only tentatively suggest that our model is applicable to the enhancement regime. However it seems to be the only model capable of explaining all the NMR data in this region.

The pressure dependence of the relaxation rates should provide further information on the enhancement region. They show that at high x , T_1 is relatively independent of pressure up to 4 KBar, which is to be expected if a rigid band model is to hold in this region. In the enhancement region however, T_1 increases by up to about 30% with 4 KBar with the increase being roughly proportional to the slope of the T_1^{-1} versus x^2 graph. Tunstall⁹⁵ initially proposed that the enhancements were caused by a change in character at the Fermi surface due to a Sodium type band being swept down into the conduction band by lattice contraction. Hence the application of pressure should produce a shorter T_1 which is in direct contrast to experimental evidence. Instead we propose that the transfer to Sodium character at low x is due to a breakdown in screening. At high x , the Sodium ion left after it loses its electron to the Tungsten orbitals, forms a centre of positive charge which is screened by the conduction electrons. However the decrease in x reduces the conduction electron density and also reduces the effectiveness of the screening. Eventually the increased attractive potential of the Sodium ion experienced by the conduction electron may be large enough to cause that electron to spend a considerable time in the vicinity of the

Sodium ion, and hence the conduction band may acquire Sodium character. Pressure may then cause the electronic overlap integral between adjacent sites to increase, resulting in an increase in the conductivity. The screening of the Sodium ion will be improved, and the slight decrease in Sodium character will produce a slightly longer T_1 . Also the increase in the conductivity should decrease the Warren enhancement since the jump distance remains approximately constant. This should also give a slightly longer T_1 . If we assume that the gradient of the T_1^{-1} versus x^2 curve gives a measure of the change in character at the Fermi surface produced by screening, then any change in screening caused by pressure in the 0.22 sample will produce a much smaller change in T_1 than that caused by the same change in the $x = 0.25$ and 0.35 samples. Hence we have a mechanism which may explain the pressure dependence of T_1 .

Finally we shall comment on the fact that these are some theoretical doubts about the Warren mechanism. In the diffusive regime, the electron is assumed to increase its dwell time on a particular site. However standard solid state theory predicts that the dwell time only depends on the electronic transfer integral, which should not change dramatically upon entry into the diffusive region. However in our case we have proposed that the diffusive region is also characterized by a large change in character of the conduction electron wavefunctions at the Fermi surface. This may alter the transfer integral, and hence the Warren mechanism may apply.

7.2.3 The $x = 0.22$ Sample

As has been indicated previously, the $x = 0.22$ sample exhibits anomalies in many of its properties. In this section we shall collect together the experimental data and try to put forward some proposals for these anomalies in view of the proximity of the metal non-metal transition.

The transport data¹¹² shown in Fig. 5.6 indicate that for samples

below $x = 0.25$, the resistivity increases on reducing the temperature down to 77 K and then flattens off below this temperature. Above $x = 0.25$ the resistivity is more like that of a normal metal, decreasing with decreasing temperature. The number of Hall carriers^{86,110} for the $x = 0.22$ sample at 77 K and 4.2 K can be seen from Fig. 5.7 to be approximately half the number of carriers at room temperature, with the room temperature value lying on the line proportional to x . Both results have been taken to imply that partial localisation occurs at low temperatures with an activation energy such that at room temperature, all localisation has disappeared. Mott¹³⁹ has argued that such localisation need not be present, and has assumed that the low temperature data is depressed by the g factor of section 3.5, with the density of states being reduced by disorder. As the temperature is increased, he proposes that electrons in disordered states may be excited into states well away from the diffusive region, until at room temperature, very few electrons are in this region and g becomes of the order of unity.

As regards the NMR data on the $x = 0.22$ sample, Weinberger¹²⁸ has found that the Tungsten Knight shift is drastically reduced, and that some of the resonance line corresponds to a positive shift. Our own data for the Sodium relaxation rate for the $x = 0.22$ sample shows that at 50 MHz, the rate is about 30% lower than that measured by Tunstall⁹⁵ at 11 MHz. This field dependence cannot as yet be compared with the Tungsten resonance where measurement have only been made at one frequency. The Sodium T_1 for the $x = 0.22$ sample increases much faster on going from 4.2 K to 2.1 K than the increase predicted by $T_1 T = \text{constant}$. This increase is not quite so large when 4 K Bar pressure is applied to the sample. This anomalous temperature dependence was not in evidence in the Tungsten data. The Sodium linewidth may be showing signs of increasing for the $x = 0.22$ sample, but there is no change in width or shape on going from 4.2 K to 2.1 K. Another

slightly disturbing feature is that although the chemical composition is $x = 0.22$, the x ray composition is $x = 0.18$ which is contrasted with all the other samples where the two measurements agree reasonably well.

Finally we comment that there is no departure from the x dependence of the specific heat or magnetic susceptibility¹¹⁴ for this sample. Although the susceptibility could not be measured at low temperatures due possibly to paramagnetism from unreacted Sodium Tungstate, no temperature dependence was observed around room temperature. This has generally been taken to imply that the transition is not caused by the separation of two Hubbard bands. We shall support this view, and propose that Anderson localisation is the driving mechanism for the transition. There seems to be two main ways in which Anderson localisation can occur as x is reduced.

The first model involves the conduction band remaining more or less the same shape down to low x and having a region of localised states in the tail. As the Fermi level moves towards the tail, there is an increasing tendency towards localisation, and when it crosses the mobility edge between the localised and extended states, then the transition occurs. Considering the $x = 0.22$ sample, it is possible that statistical fluctuations in potential caused by random Sodium occupancy, could cause Anderson localisation in certain regions of the sample. Carriers in such regions could presumably be thermally activated into extended states, and hence the temperature dependence of the transport data might be explained. There is however a problem in that a single electron localised on a particular site would act as a paramagnetic impurity, and would tend to broaden the NMR line. Although there is some evidence that broadening does occur in the $x = 0.22$ sample's Sodium line, we have calculated that the measured linewidth implies that less than 1% of the electrons can be in

localised states. For this mechanism to fully explain the transport data, it requires that many more localised carriers exist at low temperatures, but this would dramatically broaden the resonance line. As an alternative, we could take Mott's suggestion¹³⁹ that no localisation occurs, but that the density of states is depressed by disorder at 4.2 K, while at 300 K many of the carriers are excited into states outside the diffusive regime. Suppose the Fermi level moves down the conduction band in a similar manner to the high x behaviour deduced from equation (5.3). Then the diffusive regime, which we have already stated to lie below $x = 0.35$, corresponds to an energy range of about 0.2 eV. This means that about 2000 K will be required to excite carriers out of the diffusive regime. Although the rigid band model of equation (5.2) almost certainly fails at low x , it does seem that rather large temperatures will be required for Mott's proposal. Also since the $x = 0.25$ sample does not exhibit any anomalous transport properties, it would appear that for this model to hold, the diffusive region must be much narrower than predicted by the NMR and conductivity data.

The second model involves an impurity band being formed below the conduction band, similar to a doped semiconductor situation. At low x , we have already proposed that a Sodium type band, possibly 3d, is swept down into the conduction band. If we extend this further, it is possible that a narrow impurity band derived from these Sodium orbitals may be formed at the bottom of the conduction band. The impurity band may merge into the conduction band and consist of an admixture of Sodium and Tungsten 5d states. Anderson localisation might then occur in the low density of states area between the two bands. The formation of such a band has previously been disregarded¹³⁹, since even at low x there is still appreciable overlap between wavefunctions, and the donor concentration is much higher than the comparable semiconductor case. However this has assumed the wavefunctions are

Tungsten 5d in character. If instead, the wavefunctions are Sodium 3d in character, the overlap may be much reduced, and hence a very narrow impurity band may be formed. If this is the case, the transport data may be explained along similar lines as we have explored before, and we also can make some progress on the field dependent relaxation rate of the $x = 0.22$ sample. There are two possibilities for this, both based on doped semiconductor ideas, where field dependent relaxation rates have also been observed¹⁴⁷.

Firstly, in Chapter 2, it was stated that the relaxation rate was proportional to the square of the density of states at the Fermi surface. More correctly, it is proportional to the product of the densities for up and down spins. An applied field B_0 can shift these densities by an amount $2\beta B_0$ such that their product is significantly different from the square of one such density. For laboratory fields, the shift in energy is about 1 meV, whereas the bronze bandwidths are three orders of magnitude larger. However if a narrow impurity band is formed, this effect may become significant.

Secondly, the B_0 field may produce shrinkage of the wavefunctions, causing a reduction in the density of states at the Fermi surface, or a tendency toward increasing localisation. This mechanism has been shown to be important in systems such as InSb¹⁵⁹, where the carriers have a low effective mass and there is a large dielectric constant. For typical bronze bandwidths, fields of around 10^4 T are required to produce any shrinkage, but once again, if an impurity band is formed, this effect may be important.

There are many more mechanisms which may be present in the $x = 0.22$ sample. The sample is very close to an electronic and structural transition, and the physical properties in such regions are complex. We consider that it would be extremely speculative to add to the comments we have made on the $x = 0.22$ sample, since only this sample shows any anomalies. A fine mesh of samples around the

transition is required, so that trends in the data may be observed, and it may be determined whether the anomalies arise from the proximity of the transition, or from some peculiarity of the one particular sample.

CHAPTER 8CONCLUSION

As has been mentioned in the introduction, there were two main areas in which this work was directed. The first involved the peculiar quadrupolar properties of Na_xWO_3 , and in this area our aims were to clear up some of the previous measurements, to study the effect of pressure, so as to separate the effects of reducing x from the corresponding change in lattice constant, and to establish a model of the structure. The second area involved the Sodium spin-lattice relaxation rates and Knight shifts, and here we aimed to again tidy up existing data, to obtain more accurate Knight shifts and hence to determine their x dependence, to study the effect of pressure on the enhancement region of the relaxation rates, and to obtain more data on the low x samples, with a view to understanding the metal non-metal transition. We shall take each of these areas in turn, and summarise the conclusions which we have drawn from this work.

The two main models which existed to explain the coexistence of cubic and non-cubic Sodium sites in the bronzes were the cluster model^{54,124}, in which Sodium nuclei were assumed to cluster into local $x = 1$ regions, and the Oxygen displacement model^{94,95}, in which the Oxygen atoms moved away from their ideal cubic positions midway along the cube edges. As we have mentioned in this work, there has been much criticism of the cluster model, and we have collected most of these comments together in the Discussion chapter. Briefly, the cluster model does not seem to account for the x dependence of the NMR relaxation rates and Knight shifts, the x dependence of the photoemission data¹⁰⁴ and the Kohn anomaly¹⁰⁶, and the existence of a narrow singlet peak in the x ray spectra. Moreover it does not really explain the NMR Echo widths if screening is considered,

nor can it explain the apparent loss of Echo signal at high temperatures⁹⁴. In addition, our pressure measurements on the Echo width suggest that the large field gradients present at the Echo sites do not arise from nearest neighbour Sodium vacancies, since the change in Echo width with pressure if such a mechanism is present, is much smaller than that which is actually measured. Hence in view of the available data, we conclude that the cluster model is not applicable to Na_xWO_3 .

Instead we propose that displacements of the Oxygens occur in the bronzes. To the two original models for this proposed by Tunstall⁹⁵ and Borsa¹²⁷ we have added a third, based on our own data. From his intensity data on the Sodium resonance, Tunstall obtained a value of three Echo nuclei to every one FID. Hence he incorporated the neutron data of Atoji and Rundle⁹² and proposed that the unit cell is octupled in volume with two of the eight Sodium sites vacant at high x . These two sites were assumed to have a cubic nearest neighbour Oxygen environment whereas the other six had a non-cubic Oxygen environment. If all the sites are populated randomly, then the ratio of the two types of sites may be explained. However the data is subject to uncertainty due to our new evidence that the pulsewidth required to maximise the Echo is different from that to maximise the FID. There is also the additional problem that the model predicts that the FID should disappear at high x , whereas our own data shows that this is not so. Borsa has measured the temperature dependence of the quadrupole coupling constant, and has shown that this can only be explained by similar tilts of the Oxygen octahedra along the C axis. However as we have pointed out, this structure is incapable of producing any FID nuclei, since all nuclei lie in non-cubic nearest neighbour Oxygen environments. Hence we propose an alternative model for the structure, which is based on our own data that there are about seven Echo nuclei to every one FID. This model assumes that the unit cell is octupled

in volume, with one of the Sodium sites having all the nearest neighbour Oxygens bent away from it. This produces the FID signal, whereas the other seven sites have non-cubic nearest neighbour Oxygen environments, and hence contribute to the Echo. We have calculated the field gradients produced by this non-cubic Oxygen environment at the Sodium site, and have shown that the measured Echo widths can be produced by a sensible Oxygen displacement. Moreover, if the W-O distance is assumed to remain constant, then the pressure dependence of the Echo width may be explained in terms of the pressure inducing increased Oxygen displacement. We have calculated the change in Echo width produced by 4 KBar pressure and have shown that the change is consistent with the increased field gradient produced by the change in Oxygen position. However our model suffers from the fact that from physical considerations, such as atomic size and type of bonding, we would not expect our type of Oxygen displacement to occur. The more regular model of Borsa¹²⁷ is more likely to occur. However we comment that the non-stoichiometric nature of the samples may make comparison with other systems unrealistic, and hence our model may apply. Hence we conclude that although there is still some doubt as to the exact type of Oxygen displacement, nevertheless Oxygen displacement does occur, and is responsible for the peculiar quadrupolar spectra of the bronzes. Having accepted this, the variation of Echo width with x is interesting.

The Echo width shows a broad maximum around $x = 0.5$. This we interpret as being due to a minimum in the quadrupolar coupling constant which in turn means that a minimum occurs in the Oxygen displacement. Support for this idea comes from other data. Firstly other NMR data⁹⁴ has indicated that a phase transition occurs from the distorted cubic phase to a cubic phase involving no Oxygen displacement at temperatures T_s which are between 400 K and 500 K. There is evidence from thermal conductivity¹¹⁷ and thermal expansion¹¹⁶

data that such a transition does occur at T_s , and that T_s is a minimum around $x = 0.5$. Hence we propose that this minimum in T_s implies that a minimum occurs in the energy required to drive the system cubic, which in turn implies that a minimum may occur in the Oxygen displacement around $x = 0.5$, which fits in with our own data on the Echo width.

The reasons for such a minimum in the Oxygen displacement are not immediately clear. We propose the existence of two competing mechanisms. On the low x side of the minimum the reduction in lattice constant with x is assumed to increase the displacements. On the high x side, the pressure measurements have indicated that this mechanism still holds, but is dominated by some opposing mechanism. It is proposed that this is caused by a strong Sodium-Oxygen attractive interaction which becomes important because of the increased Sodium concentration, and which increases the amount of Oxygen displacement.

We now turn to the second area of interest, which is the information derived from the spin-lattice relaxation rates and shift measurements. A high x region has been defined which includes samples with $x \geq 0.35$, where we have confirmed that the Sodium relaxation rate is proportional to x^2 . If this is taken with the similar dependence of the Tungsten relaxation rate¹²⁸, then we confirm Tunstall's proposal⁹⁵ that in this region, a rigid band model is applicable, with electrons filling up the conduction band so that the Fermi level moves upwards in this band as x increases. Moreover the density of states for this band is described by the exponential bandshape of equation (5.2).

The region $x < 0.35$, known as the enhancement region, is characterised by a drastic reduction in the Tungsten Knight shift accompanied by a slight decrease in the relaxation rate¹²⁸, whereas the Sodium Knight shift increases slightly and is accompanied by a large enhancement in the relaxation rate. This has led to speculation that there is some change in character from Tungsten to Sodium

orbitals at the Fermi surface. We have shown that a small amount of Sodium 3s character can explain the Sodium relaxation rate enhancement, but unfortunately causes a positive Knight shift. The addition of Sodium 3p character cannot cancel this positive shift, nor can it on its own produce sufficient enhancement of the Sodium relaxation rate. Instead we have proposed that a large transfer to Sodium 3d character occurs at the Fermi surface. We have estimated that the increased core polarisation hyperfine field of 3d over 3p orbitals can produce the measured enhancement in the Sodium relaxation rate, provided that a Warren mechanism holds²¹. The loss of Tungsten character at the Fermi surface causes a large decrease in the Tungsten Knight shift, while the Warren mechanism opposes this decrease in the relaxation rate resulting in only a small drop. Meanwhile, the appearance of Sodium 3d character gives a slight increase in the Sodium Knight shift, and acting with the Warren mechanism, it produces a larger increase in the relaxation rate. We have calculated that the NMR data can be explained by a transfer of about 56% of Tungsten 5d character to Sodium 3d character at the Fermi surface for the $x = 0.25$ sample. This is accompanied by Warren enhancement factors of 3.8 and 2.4 for the Sodium and Tungsten resonances respectively, and in view of the approximate nature of these calculations, these probably agree reasonably well with the value of about 2 expected from the conductivity data. The real objection to this model is that although there is some physical justification for assuming that 3p and 3d character will appear in preference to 3s, there seems to be no reason for assuming the existence of 3d character in preference to 3p. However a significant quantity of Sodium 3d character at the Fermi surface does seem to be the only mechanism capable of explaining fully all the NMR data.

The original assumption for the existence of Sodium character was based on the Sodium type band being swept down by lattice contraction⁹⁵. However we have shown that the relaxation rates decrease slightly with pressure in the enhancement region and hence it must be concluded that this mechanism does not occur. Instead we propose that the reduction in conduction electron density with the reduction in x causes a reduction in the screening of the Sodium ion by the conduction electrons, and that this could drive a Sodium type band downwards into the conduction band. Application of pressure to the system might cause increased wavefunction overlap and hence an increase in the effectiveness of the screening. The amount of Sodium character would then decrease, and the relaxation rate would decrease. Moreover, the increase in conductivity with pressure might decrease the Warren enhancement factor, again producing a slightly lower relaxation rate.

The final region as regards relaxation rates and shifts is the low x region very close to the metal non-metal transition. In particular we have found that the $x = 0.22$ sample exhibits anomalies in the field and temperature dependence of its relaxation rate, and there is evidence from other work of anomalies in the transport data¹¹². The proximity of this sample to the transition has led us to attempt to explain these anomalies in terms of possible driving mechanisms for the transition. Firstly we have assumed that the lack of any deviation from the x dependence in the specific heat and susceptibility data¹¹⁴ indicates that the Hubbard interaction is not important. Hence it would seem that Anderson localisation due to disorder introduced by the random Sodium occupancy is the driving force behind the transition. We have introduced two basic models for the conduction band at low x . The first assumes that the conduction band has a similar sort of shape to that found at high x , and that localisation is occurring in the band tail. Statistical fluctuations in potential due to the random

Sodium occupancy might cause localisation in certain regions in the sample. The carriers in these regions could however be thermally activated into extended states, which might explain the anomalous temperature dependences in the NMR and transport data. However any such localisation would presumably introduce paramagnetic centres into the samples which would drastically broaden the NMR line. The line however remains reasonably narrow. An alternative explanation¹³⁹ which avoids this problem, assumes that localisation does not occur, but that the disorder depresses the density of states at low temperature. As the temperature increases, carriers are excited out of the diffusive regime and hence the density of states increases. Although this may explain the temperature dependences, it seems that for this model to hold, the diffusive region must be much narrower than that predicted by transport and NMR data.

The second model assumes that an impurity band derived from Sodium orbitals is formed below the conduction band. This follows on from our assumption that a Sodium type band is swept down into the conduction band. If the overlap integral for the Sodium wavefunctions is small, then this impurity band may be narrow, and hence may either be separate from the conduction band or may merge into it. The anomalous temperature dependences may be explained as before by Anderson localisation, except that the localisation now occurs in an impurity band, or in the pseudogap between this band and the conduction band. This type of model also means that comparisons can be made with the doped semiconductors. In particular, the applied field may split the band into separate densities of states for up and down spins. If the band is narrow, this can lead to a reduction in the relaxation rate. There is also a possibility that the applied field shrinks the electron wavefunctions so as to reduce the density of states or to cause increased localisation¹⁵⁹. Both these mechanisms are attractive

in explaining the field dependence of the relaxation rates.

Both of these models however are rather speculative, in view of the fact that only the $x = 0.22$ sample exhibits any anomalous behaviour. Hence we have considered that it is unrealistic to proceed further into what may be a very complex situation, involving simultaneous electronic and structural transitions. We await more detailed work on a fine mesh of samples around the transition, so that it may be resolved whether the anomalies are due to the proximity of the transition, or instead to some peculiarity in the $x = 0.22$ sample.

CHAPTER 9APPENDIX9.1 Samples

The Na_xWO_3 samples used in this work were prepared at Cornell University USA and are tabulated in Fig. 9.1. They are the same samples as were used by Weinberger¹²⁸, and by Tunstall⁹⁵, except that for the latter study, the $x = 0.74$ and 0.84 samples had not been grown. For $x > 0.4$, large single crystals can be grown¹⁴¹ by electrolysis of a fused mixture of $\text{Na}_2\text{WO}_4 \cdot 2\text{H}_2\text{O}$ and WO_3 . For lower x , a diffusion dilution process was used^{111,86}, in which $x = 0.6$ crystal slices were packed in the right amount of WO_3 powder to achieve the desired x value. This mixture was heated to above 900°C for 10 days, during which time the Sodium diffused out of the slices into the powder. On quenching to room temperature, two sources of cubic samples were present; the diluted crystal slices, and the enriched host powder.

X-ray determination showed that all samples in Fig. 9.1 existed in the cubic phase with the x value derived from the x dependence of the lattice constant (equation 5.1) shown in column 4 of Fig. 9.1, in agreement with that derived from chemical analysis. Also the x ray linewidth indicates an inhomogeneity $\Delta x \approx \pm 0.01$. The Sodium concentration was also determined by atomic absorption spectroscopy at Cornell, and the results shown in column 3. In addition, flame emission spectroscopy showed Calcium present at 100 ppm, but no other impurity at levels greater than 10 ppm. Electron microprobe analysis on the $x = 0.35$ sample showed homogeneity within the 20% uncertainty of the technique. In addition, a sample was grown by electrolysis at St Andrews. X ray measurement gave $x = 0.68$, but no chemical analysis has been carried out on it.

Table 9-1

Samples Used in This Work

<u>Nominal x</u>	<u>Method of Production</u>	<u>Chemical Analysis x</u>	<u>X-ray x</u>
Na_xWO_3			
0.22	Electrolysis + Diffusion	0.22	0.18
0.25	Electrolysis + Diffusion	0.26	0.25
0.30	Electrolysis + Diffusion	0.31	0.30
0.35	Electrolysis + Diffusion	0.36	0.37
0.40	Electrolysis + Diffusion	0.40	0.42
0.57	Electrolysis	0.55	0.57
0.74	Electrolysis		0.74
0.84	Electrolysis		0.84

On arrival from Cornell, the samples were in the form of a powder dispersed in paraffin wax to ensure RF penetration due to skin depth problems. Since this was undesirable for pressure work, the wax was removed by washing in petrol, leaving the Na_xWO_3 powder. There was evidence however that a thin layer of wax still remained on the surface of each granule in the powder, thus ensuring electrical insulation of one granule from the next. Other workers⁹⁴ have not provided insulation such as wax, and have assumed that the thin Sodium-free layer, which has been shown to exist on the surface of the samples, will insulate the particles from each other. All samples, except $x = 0.25$ and 0.35 had previously been used in measurement of the Tungsten Knight Shift¹²⁸, and had been mixed with Tungsten metal as a reference. This metal could not be separated from the bronze, but it was thought that it would not effect any of the results, except for causing a diminution of the signal due to a poorer filling factor.

9.2 NMR Apparatus

9.2.1 50 MHz NMR Spectrometer

The NMR pulse spectrometer is shown schematically in Fig. 9.2, and is similar to those discussed elsewhere^{142,143}. The RF is provided by a free-running quartz crystal oscillator operating at 50 MHz, with a frequency stability of 1 part in 10^7 . This RF is gated by a Relcom co-axial switch which is controlled by a bank of Tektronix 160 series pulse generators, arranged so that in addition to single pulses, two pulses of different width, and comb sequences could also be produced. Since the Relcom switch requires +1.5 V to switch on and -1 V to switch off, the pulse from the Tektronix units was modified by a simple shaping circuit.

The RF pulses from the switch were amplified by three power amplifiers in series. The first, an ENI 300 P, operated in Class A

and produced 3 W into a 50 Ω load. The second and third were vacuum tube amplifiers, operating in Class C, and producing 50 W and 600 W into 50 Ω . The output impedance of the 50 W was matched to 50 Ω by a π circuit. A similar matching circuit was used on the 600 W output, except that it matched the tube impedance to several hundred ohms, a value more in keeping with the probe impedance.

The NMR signal was detected by a Polaron pre-amp and receiver system. Since the receiver employs phase sensitive detection, a reference signal is derived from the crystal. This reference is amplified, and can also be shifted in phase. The receiver output could be displayed on a storage oscilloscope, and could also be stored by a Datalabs DL905 Transient Recorder. The DL905 digitises the signal into 1000 points with a minimum total sweep time of 200 μ s. The output from the DL905 could be plotted on an X-Y recorder for a permanent record, or if signal averaging was required, the first 100 points in the DL905 store could be fed into a Datalabs DL101 Signal Averager which provided an averaging capability of up to 512 sweeps. Both the DL905 and DL101 could be interfaced to a Data Dynamics 1133 Paper Tape Punch and this will be described later in this chapter.

9.2.2 The NMR Probe

The NMR probe system (Fig. 9.3) is based on a design by Lowe and Tarr¹⁴⁴. On pulse, the receiver is protected from overload by the diode short to earth, which leaves the pulse at the top of the probe unaffected, since the $\lambda/4$ cable to this short causes it to appear as an infinite impedance. Off pulse, the transmitter is isolated from the probe by the series crossed diodes, since the low voltage NMR signal is not large enough to cause these diodes to conduct. Similarly the diode short does not conduct off pulse, and so the NMR signal can reach the pre-amp. The transmission lines from the sample coil to the transmitter and to the receiver are multiples of $\lambda/2$, in

order to minimise reflections due to mismatches. The exact lengths of cable required were determined by connecting one end of the cable to a Wayne-Kerr RF Bridge, leaving the other end open-circuit. As the line is trimmed shorter, a $\lambda/4$ line is determined as that length at which the line changes behaviour from an inductance to a capacitance, whereas for a $\lambda/2$ line, the change is from a capacitance to an inductance.

The solenoid sample coil consists of two turns of flat copper strip of width 3 mm, with overall dimensions of 11 mm diameter and 8 mm length. Since the magnetic field B_0 from the superconducting solenoid acts along the axis of the high pressure chamber, this sample coil must sit across the chamber. These coil dimensions maximise the sample volume for a 14 mm diameter chamber. Although the alternative saddle-shaped coils^{145,146} would provide a larger sample volume for this chamber geometry, they would also entail a reduction in signal to noise by a factor of about three. The coil was potted in Stycast to eliminate any spurious ringing after the pulse. The inductance of the coil alone was measured on the Wayne-Kerr Bridge to be 0.04 μH with a $Q \approx 150$ at 50 MHz. When the coil was placed in the cell with the transmission lines connected, the Q dropped to about 20 at room temperature. The coil was tuned outside the pressure cell by soldering capacitors between the end of the screwed rod and the cell body. Dipped silver mica capacitors were used because of their low capacitance variation with temperature. These capacitors are in the Helium bath and so an improvement in signal may be produced. The value of capacitance used was 130 pF.

The parallel impedance of a tuned circuit is given by

$$R = QLw \quad (9.1)$$

which for our coil is of the order of 250 Ω at room temperature, and probably higher at low temperatures. Hence the output π circuit of

the 600 W amplifier was designed to match the amplifier to several hundred ohms load. The mismatch between the transmitter and coil and the 50 Ω cable was neglected. The system could produce pulses of ≈ 1100 V pk/pk across the coil with rise and fall times of about 2 μ s. The B_1 field produced by such a pulse can be calculated from¹⁴⁷

$$B_1 = \left(\frac{\mu_0 L}{4V_c} \right)^{\frac{1}{2}} \frac{V}{\omega L} \quad (9.2)$$

where V_c is the coil volume, and V is the zero to peak voltage developed across the coil. For our case, 60 Gauss should be produced, but in practice, a $\pi/2$ pulsewidth of 2.5 μ s for protons shows that only about 25 Gauss is produced. This reduction may be caused by measuring $V \approx 550$ V externally to the pressure cell, whereas the actual voltage across the coil may be less than this due to the inductance of the electrical lead-through.

The receiver recovery after a pulse was ≈ 30 μ s. This could be improved by replacing the IN4004 diodes in the diode short by AAZ17 diodes, but since the latter blew frequently, and since good recovery times were not essential, the IN4004 diodes were used.

9.2.3 The Superconducting Magnet

The superconducting solenoid, supplied by Thor Cryogenics, is wound from single core Niobium-Titanium, with a maximum field of 5 T. The main field coils are supplemented by a set of Garrett coils to improve the axial homogeneity, and by two sets of Golay coils (0° and 90°) to improve the radial homogeneity. In addition, a set of Z_0 coils are provided to change the main field by ± 0.5 mT. The main field coil is driven by a Thor Series 6000 Power supply, which is connected to it in parallel with a superconducting switch. Passing current through a heater coil surrounding this switch drives the

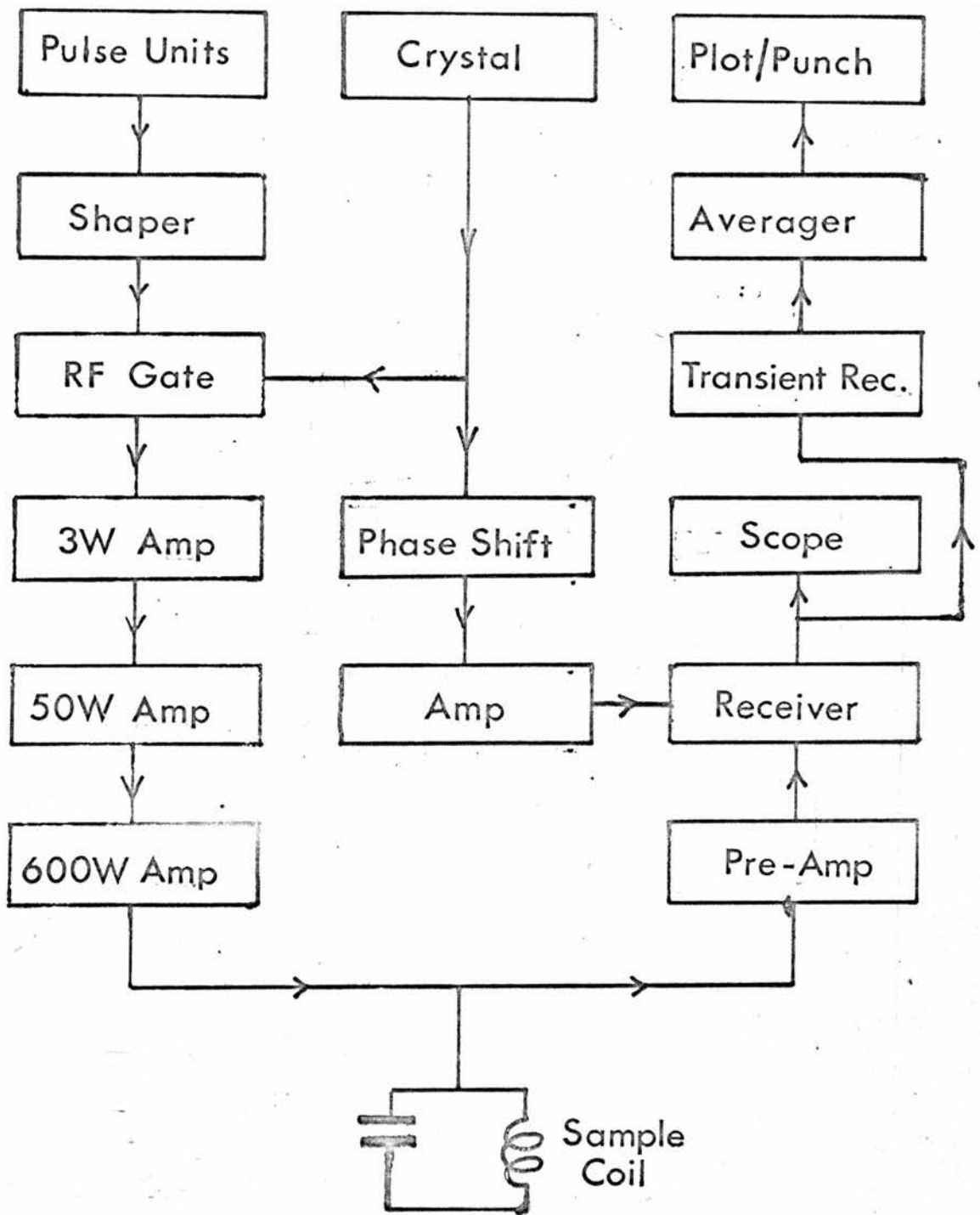


FIG 9.2 50MHz NMR Pulse Spectrometer

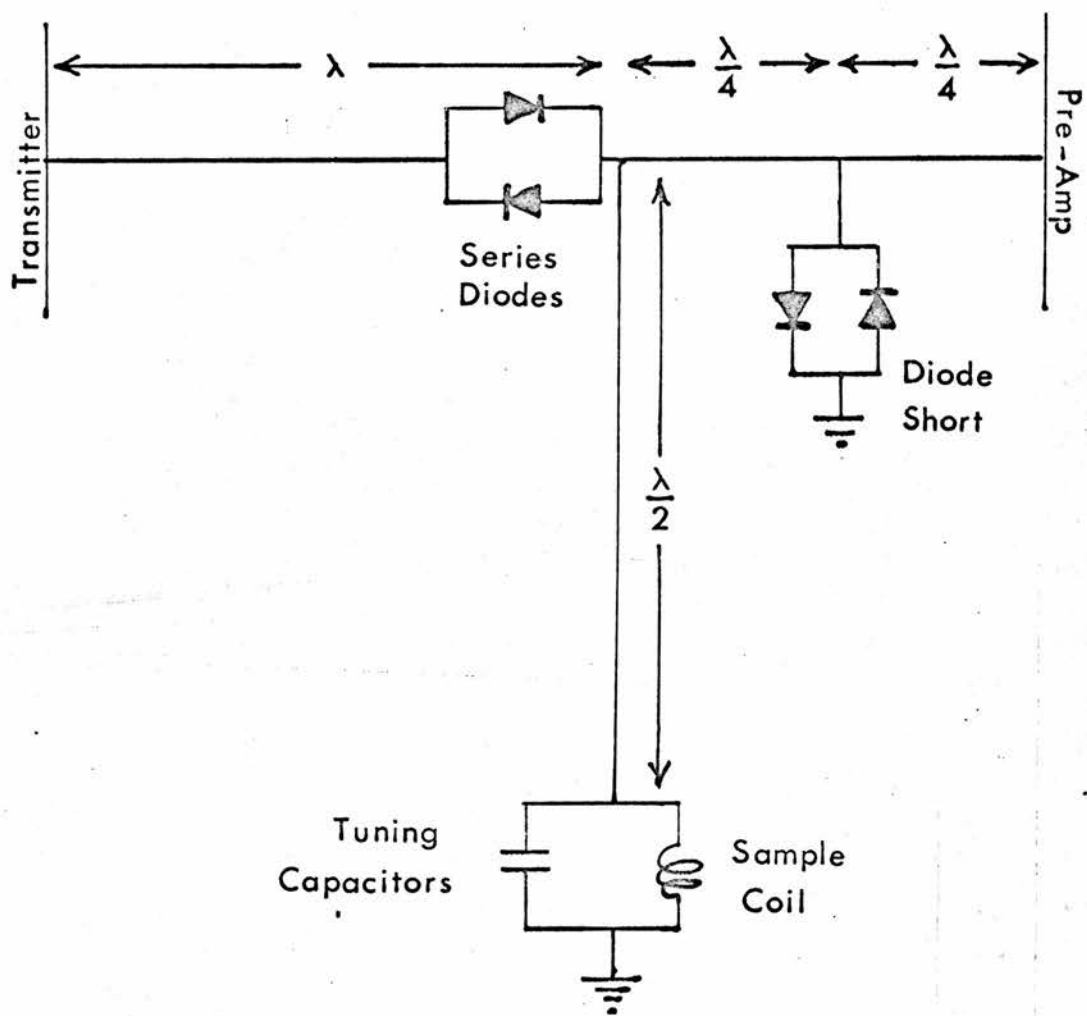


FIG 9-3 50MHz. NMR Probe

switch normal. The supply can then charge up the main field coil to the desired value (50 MHz for Na requires a 4.44 T field and a current of ≈ 34 A). The charging process takes about one hour, since the magnet may quench if a faster rate is used. When the desired field is reached, the heater is switched off, the switch becomes superconducting and the power supply may be returned to zero current, leaving the magnet in persistent mode. In this mode, the magnet is quoted to have a negligible decay rate, although continually moving the large metallic pressure cell in and out did cause a very small decay.

The homogeneity quoted by Thor over a sample 10 mm long and 10 mm diameter is better than 1 part in 10^5 with 10 A in the 0° Golays and 430 mA in the Garrett. Our own measurements with a room temperature insert and a 10 mm long, 14 mm diameter sample of aqueous NaCl gave a homogeneity of 120 μ T in 4.44 T with no current in the subsidiary coils, 100 μ T in 4.44 T with 400 mA in the Garrett, and 100 μ T in 4.44 T with 400 mA in the Garrett and 10 A in the 0° Golays. Given that the Thor homogeneity plots show a rapid decrease for samples larger than 10 mm diameter, our results probably agree with the Thor results. If we extrapolate the Thor plots to the samples used in all the Bronze measurements, (9 mm length by 8 mm diameter) then we should have a homogeneity of about 20 μ T in 4.44 T. Hence with the typical measured Bronze linewidth of ≈ 100 μ T, the inhomogeneity should provide only a small correction. Further evidence for this is provided by the fact that the Bronze linewidths seemed unaffected by the current in the subsidiary coils.

The Garrett coils were also used to shift the resonance. 400 mA causes a shift of about 3 mT in the same direction as the main field. These were used in preference to the Z_0 coils, since the 5 A in the latter produced a greater liquid Helium evaporation rate.

9.2.4 Cryogenics

The superconducting magnet is positioned at the bottom of a Thor Helium cryostat. The 25 l Helium chamber is superinsulated, and is surrounded by a 30 l liquid Nitrogen chamber. Before each run, the vacuum space of the cryostat was pumped for four days, reaching 10^{-5} torr, and then the system was precooled by filling both Nitrogen and Helium chambers with liquid Nitrogen. The Helium chamber was emptied twelve hours later by blowing out the liquid Nitrogen with dry Nitrogen gas, and then by successive pumping and backfilling with Helium gas. The cryostat could then be filled with liquid Helium by syphoning out of a storage dewar. About six litres of liquid are required to cool the magnet to 4.2 K before a liquid level is formed. This level is monitored by a Thor superconducting wire type level indicator. The liquid evaporated at about 0.5 l/hour, and hence one fill enables two days operation, although this time is much reduced if the cell is raised and lowered frequently. The Helium gas is collected into a return line to the Department's Cryogenic facility for reliquification.

Since starting a run was time consuming, the cryostat was kept cold for as long as possible. The longest run lasted more than 80 days. In the seven months in which the results were taken, 2115 litres of liquid Helium were used, along with about twice that amount of liquid Nitrogen.

All measurements on the Bronzes were taken at 4.2 K. In addition, some were taken at 2.1 K, this temperature being achieved by pumping on the Helium bath. The pumping valve was opened very slowly, taking about $1\frac{1}{2}$ hours to pump down. The temperature was measured by monitoring the saturated vapour pressure of the gas with a Mercury manometer. In cooling to 2.1 K with the magnet in persistent mode, the main field dropped by about 0.2 mT. In addition, about 40% of the liquid Helium is evaporated to reach 2.1 K.

9.3 Fourier Transform NMR

9.3.1 The Fourier Transform

As is well known^{148,149,150}, the free induction decay $S(t)$ in the time domain, and the lineshape $A(f)$ in the frequency or field domain are Fourier transforms of each other

$$A(f) = \int_{t=0}^{\infty} S(t) e^{-2\pi ift} dt \quad (9.3)$$

In practice, $S(t)$ is available in digital form and the computer uses digital operations, so we use the discrete Fourier transform

$$A_f = \sum_{t=0}^{N-1} S_t e^{-2\pi ift/N} \quad (9.4)$$

where A_f is the coefficient of the f 'th point in the transform, f is the frequency difference between the f 'th point and the spectrometer frequency, and N is the number of input data points. Since the exponential in equation (9.4) can be expanded into sines and cosines, there are two sets of coefficients, the sine transform coefficients and the cosine transform coefficients. If dt is the time interval between each of the N input points, then the total frequency scan F after transform is

$$F = \frac{1}{2dt} \quad (9.5)$$

and hence the field scan length B is

$$B = \frac{\pi}{\gamma dt} \quad (9.6)$$

In order to achieve a resolution of R Hz in the frequency domain, the time domain must be sampled for R^{-1} s. In practice this does not limit the usefulness of the technique since a large number of zeros may be artificially added to the input data after the point

where the FID has decayed to zero.

The signal S_t after an RF pulse at $t = 0$ may be written as

$$S_t = G_t [A \cos 2\pi(f-f_0)t + B \sin 2\pi(f-f_0)t] \quad (9.7)$$

It can be shown that the cosine transform of S_t will only produce the pure absorption spectrum if $B = 0$ and the pure dispersion if $A = 0$. Unless care is taken over phase, the output spectrum will be a mixture of absorption and dispersion signals. We have found that the best method of phase correction involves starting the transform at the first peak or dip in the FID beat pattern. This artificially sets $B = 0$ and corresponds physically to a shift in the time origin. This method suffers from the disadvantage that any short T_2 components in the FID may be lost, although this may be avoided by adjusting the phase of the receiver reference, or working reasonably far from resonance, so that the first peak or dip is close to the start of the FID.

This method fails however when two samples are in the coil simultaneously as in the case of the Bronze Knight shift measurements, since it is unlikely that a peak in one sample will coincide with a peak in the other. The power spectrum technique was used for this. The power spectrum $P(f)$ can be calculated from the cosine transform $C(f)$ and the sine transform $S(f)$ by

$$P(f) = [(C(f))^2 + (S(f))^2]^{\frac{1}{2}} \quad (9.8)$$

The advantage of this method is that $P(f)$ is independent of the phase of the input data. The disadvantage is that the power spectrum is much broader than the absorption spectrum, and so small shifts may not be resolved. Also information about lineshape is difficult to derive from the power spectrum. One such attempt at this was made using the Kramers-Kronig relation²

$$\chi'(w) = \frac{1}{\pi} P \int_{-\infty}^{\infty} \frac{\chi''(w') dw'}{w' - w} \quad (9.9)$$

where $\chi'(w)$ and $\chi''(w)$ are the dispersion and absorption spectra, and the symbol P stands for taking the principal part of the integral. Since we already have from equation (9.8) that

$$\chi'(w) = [(P(w))^2 - (\chi''(w))^2]^{\frac{1}{2}} \quad (9.10)$$

then we have two equations in the two unknowns $\chi'(w)$ and $\chi''(w)$. In principle these can be solved numerically, but the system of non-linear simultaneous equations involved in the solution was too large for the computer, and so this approach was abandoned.

9.3.2 Electronics

The detected signal from the receiver is digitised into 1024 words by the DL905 Transient recorder with each word containing 8 bits for full-scale input. The output from the DL905 memory could be plotted on an x-t recorder or punched on paper tape by a Data Dynamics DD1133 Tape Punch. Alternatively the DL905 output could be taken to a DL101 signal averager. The DL101 accepts the first 100 words out of the DL905 store and has a resolution of 6 bits for full-scale positive or negative inputs. Hence if the averager is used, the DL905 scan length must be about ten times the length of the FID. The triggering for the DL905 and DL901 comes from the pulse units. The output from the DL101 can also be plotted or punched. We shall briefly describe the DL101 and DL905 Punch interfaces.

A. DL101 - Punch Interface

This interface was supplied by Datalabs and consisted of an extra card in the rear of the DL101. This card routes the six data bits in the DL101 store to the appropriate punch pin, and also

provides control and marker signals to the punch. Each set of data on the punched tape corresponds to a dump of the 100 numbers in the DL101 store, and consists of a block of characters all with hole 8 punched. Hole 8 is discarded after the tape is read, but is necessary since the reader ignores blank tape. Punching in hole 8 was achieved by connecting the data channel to the +5V line. Each set of data consists of 30 lines with hole 8 only, then 1 line with holes 1 and 8 signifying that data is about to begin, the 100 data words, and finally 30 lines with hole 8 only. A typical tape is shown in Fig. 9.4a. In the data, hole 7 unpunched means that the data word is the binary equivalent of a positive number in the range 0 to +63. If hole 7 is punched then a "2's complement" form of a negative number in the range -1 to -64 is represented. By 2's complement we mean that the actual number is obtained by subtracting 64 from the number on the tape.

B. DL905 - Punch Interface

This interface was home-built and is shown schematically in Fig. 9.5. It routes the 8 data bits of each of the 1024 words in the DL905 store to the appropriate punch pin, and also provides the following control signals.

Digital Output Flag - When the Punch switch on the DL905 is depressed, Digital Output Flag makes a logical 0/1 transition which goes to the Punch as an Activate signal and enables punching. This signal makes a 1/0 transition when all 1024 channels are outputted, hence prohibiting further punching.

Data Ready - This makes a 0/1 transition when new data appears on the data lines. It goes to the punch as Source Control and causes that data word to be punched.

The control signals returned from the Punch are

Acceptor Operable - A 0/1 transition indicates that the Punch is ready to commence punching. This signal remains at 1 until Activate goes to 0.

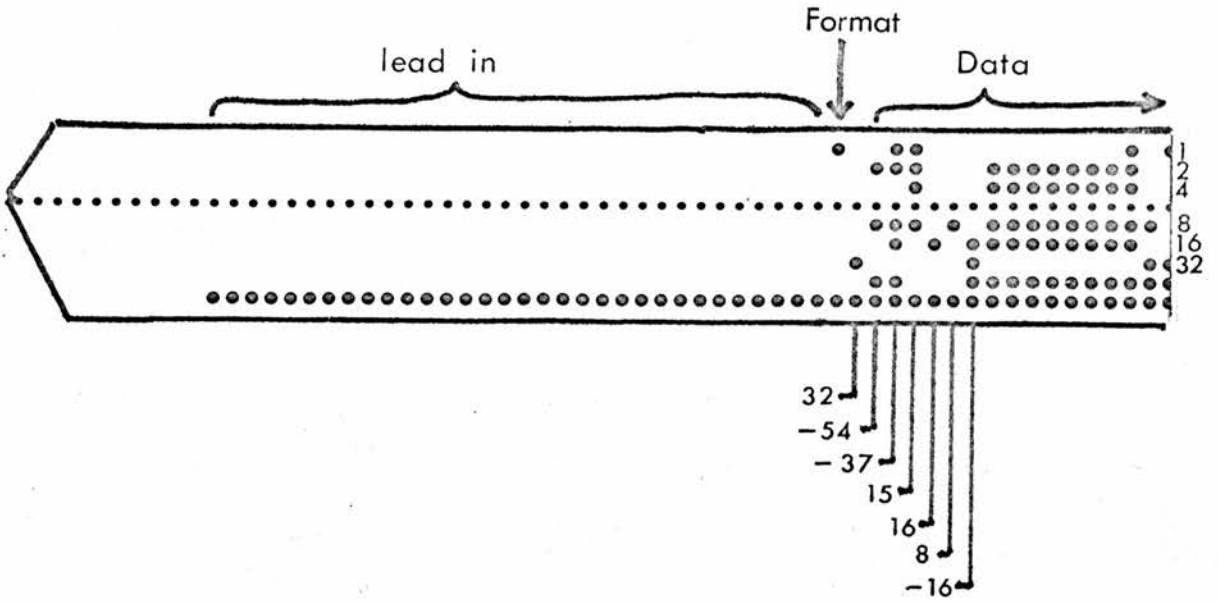
Acceptor Control - A 0/1 transition indicates that the punch has finished punching the previous data word and is ready for a new word. The transition is turned into a 100 ns pulse by the monostable, and is delayed by 2.5 μ s and goes to the DL905 as Word Request which puts the next word on the data lines.

The Punch Backspace channel is not used and so must be held to 0V as must the DL905 Digital Output Enable. This is achieved by links in the interface board and in the plug.

The Punching sequence may be described as follows:-

1. Depressing the DL905 Punch switch causes a 0/1 transition on Digital Output Flag which activates the Punch.
2. Acceptor Operable makes a 0/1 transition, remaining at 1 until Activate goes to 0, or a Punch fail mode is entered.
3. The 0/1 transition of Digital Output Flag in 1 puts the first data word on the data lines.
4. Data Ready makes a 0/1 transition causing that word to be punched, and setting Acceptor Control to 0.
5. Acceptor Control then makes a 0/1 transition which goes to the DL905 as a delayed pulse, causing Data Ready to make a 1/0 transition and putting the next word on the data lines.
6. Data Ready makes a 0/1 transition and we are back at 4.
7. When all 1024 words have been punched, Digital Output Flag goes to 0 and the Punch is de-activated.

DL101 OUTPUT



DL905 OUTPUT

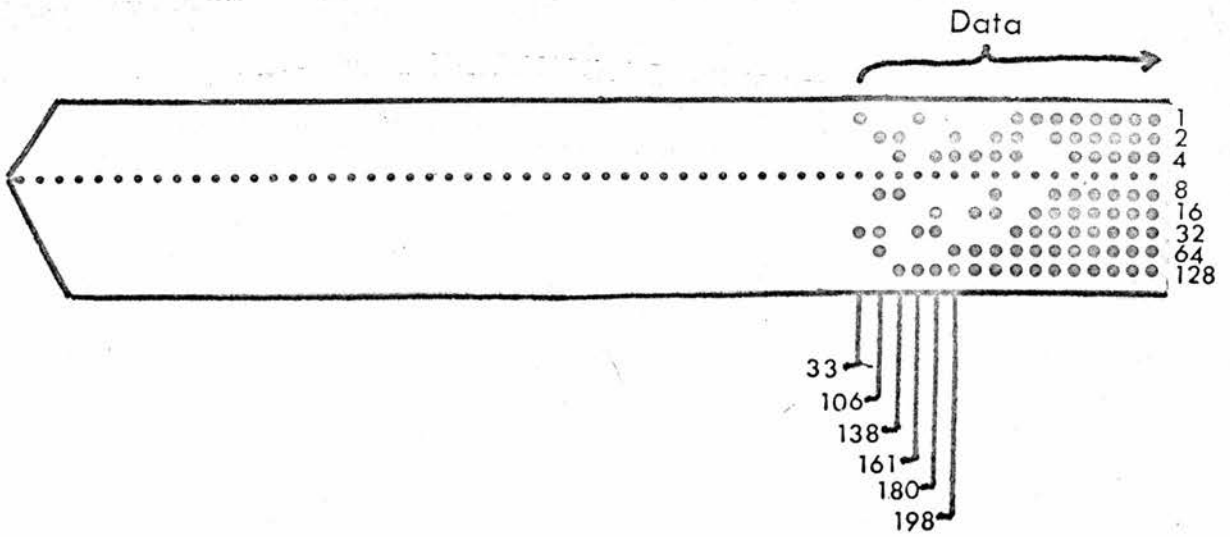


FIG 9.4 Paper Tapes

DL905 Plug J1

Punch

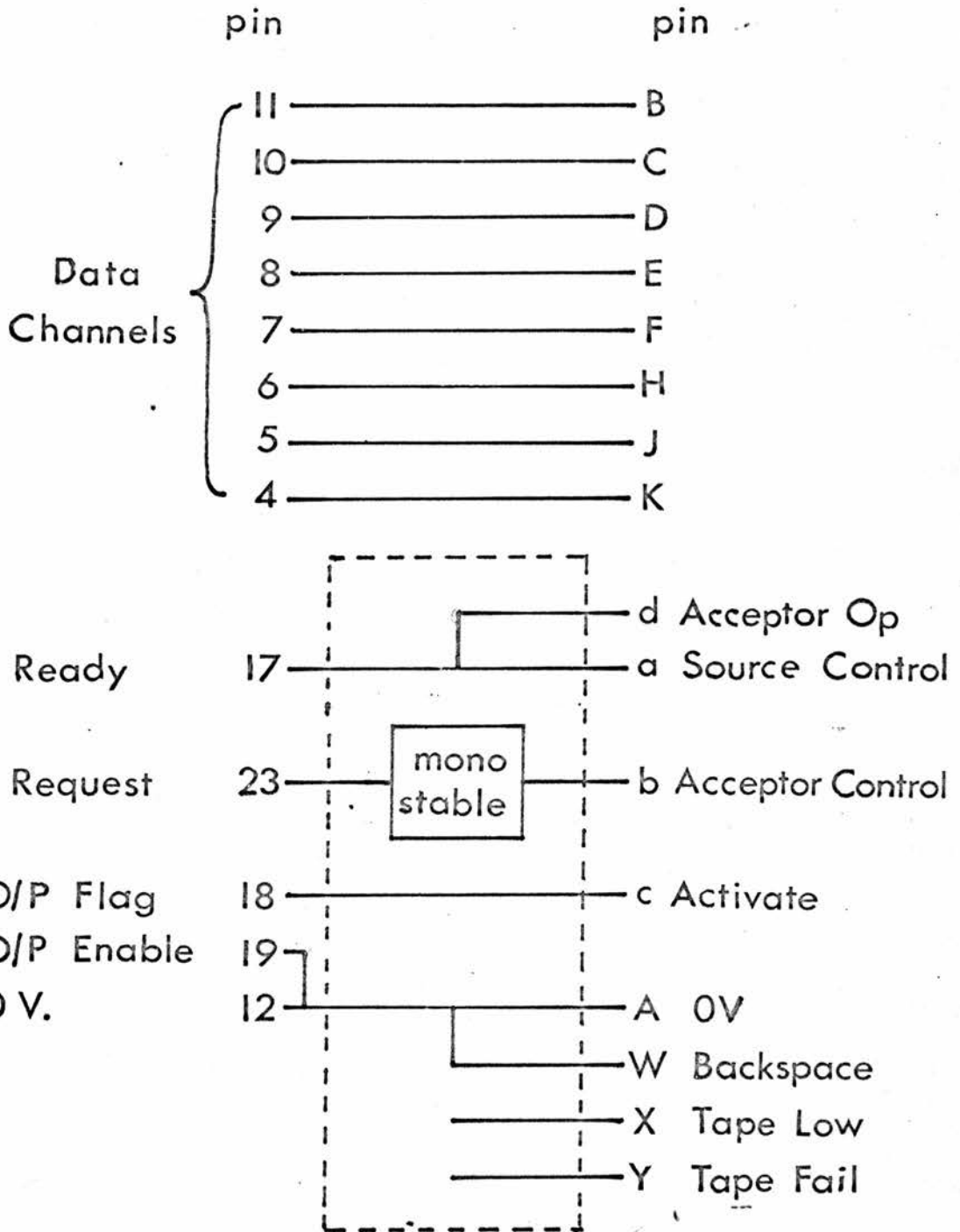


FIG 9-5 DL905 / Punch Interface

In practice, only 1023 points are punched presumably because the 0/1 transition of Acceptor Control on receipt of the Activate signal steps on Word Request before the Punch has time to punch the first word. Hence the first point may be lost, but this is not serious as the first few points are usually discarded in the phase correction. Also it was found that the interface did not work unless Data Ready and Acceptor Operable were connected together. It is not known why this is so, but it may speed up the Data Ready signal. Datalabs had to remove some filters from their own interface, whereas we did not need to do this.

Each set of data consists of 1023 words on the tape as shown in Fig. 9.4b. The data is in straight binary from 0 to +255, 0 corresponding to minus full-scale on the DL905 input, and 255 corresponding to plus full-scale. There are no introductory or marker holes as was the case with the DL101 interface. The case of completely blank tape occurs for full-scale negative input as can occur if the DL905 saturates. Since this will almost certainly be discarded by the computer program since it will occur at the start of the FID, any hole whatsoever must be punched in this area manually. This simply ensures that the computer tape reader recognises that data is present in this area, even though it will eventually be discarded.

9.4 Computer Requirements

The FID on the paper tapes is read into the University IBM 360/44 computer which performs the Fourier Transform. If the N data points were transformed by conventional means, then N^2 operations would be involved. Instead a Fast Fourier Transform package is used which involves pairing the input data at each step¹⁵¹, and represents a significant time saving since only $2N \log_2 N$ operations are required. This method requires that the number of input data points is a power of two.

The Fortran IV program is shown schematically in Fig. 9.6. The program varies slightly depending on whether the 100 numbers from the DL101 or the 1024 numbers from the DL905 are read in. Firstly five cards are inserted. DT = where DT is the time in μ s between each input data point, GAUSS = where GAUSS is the range in Gauss of the spectrum which is to be plotted, GAMMA = where GAMMA is the gyro-magnetic ratio of the nucleus studied, NO = where NO is the number of input data blocks to be read, and ND = where ND is the number of that data point at which the transform is to start.

The paper tapes are now read in by subroutines written by J. Henderson of the Computing Lab., and stored in array <A>, which is printed as Initial FID. Error messages are outputted in the event of tape failure which stops the program. In the case of the 1024 point tape, it is now necessary to find the zero level of the data. This is performed by summing that part of the data where the FID has decayed to zero, and dividing by the number of points summed. The result is then subtracted from all the 1024 points.

The next part of the program tells the transform where to start. It sets $A(ND) = A(1)$ and $A(ND+1), A(ND+2)$ into $A(2), A(3)$ etc, and hence all $A(x)$ with $x < ND$ are discarded. Zeros are now added after the FID to take the total number of data points up to 1024 for 100 initial points, and to 8192 for 1024 initial data points.

The next section performs the Fast Fourier Transform by calling subroutine RHARM. This subroutine was supplied by IBM with the computer as part of a Scientific Subroutine package. As output from RHARM, array <A> contains both sine and cosine coefficients; $A(1), A(3), A(5)$ --- being cosine coefficients and $A(2), A(4), A(6)$ --- being sine coefficients. These are separated, and the cosine coefficients are put in array and the sine coefficients in <C>. The power spectrum coefficients are calculated from and <C> and are stored in array <R>. The desired set of coefficients can now

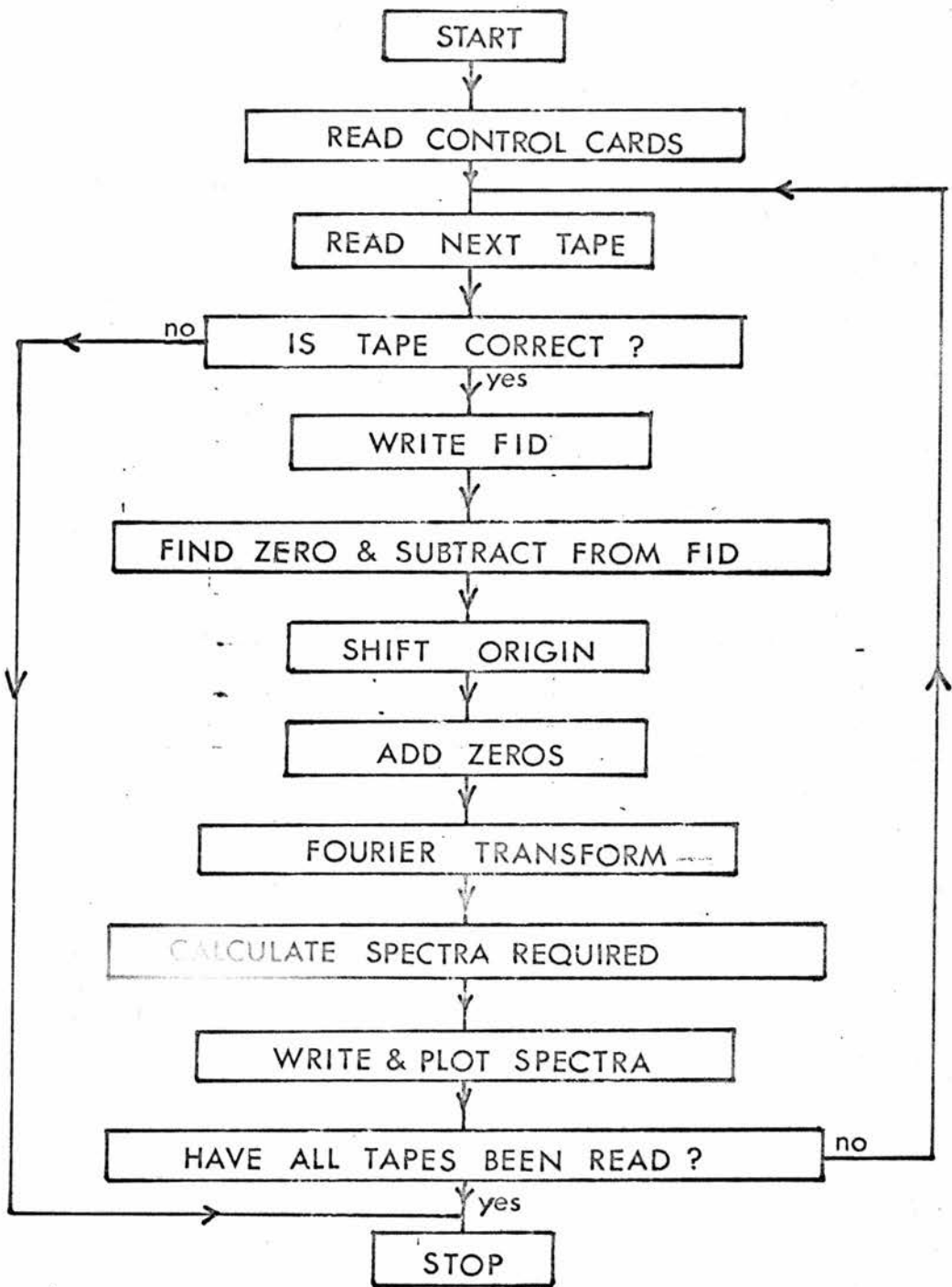


FIG 9.6 Flow diagram of Fourier Transform Computer Program

be printed and plotted on a graph plotter.

Depending on the scan length required for plotting, all the output points may not be required. GAUSS tells the computer what scan length is required. If the total scan length given by equation (9.6) is less than GAUSS, then GAUSS is reduced by fives until it is less than the total scan length. Also with the 1024 point input, the computer does not have enough storage space to perform both the main program and the plotting subroutines. This is overcome by writing the output data to a storage disk and then plotting the data on this disk by a separate program.

The method was tested by observing the Sodium resonance in aqueous NaCl solution, and then in a dispersion of Sodium metal in oil. The measured Knight Shift was

$$K = 0.109 \pm 0.005\%$$

which agrees well with the published value¹⁵² of

$$0.1085 \pm 0.0001\%$$

REFERENCES

1. ABRAGAM A., Principles of Nuclear Magnetism, OUP (1961).
2. SLICHTER C.P., Principles of magnetic resonance, Harper and Row (1963).
3. RUSHWORTH F.A. and TUNSTALL D.P., Nuclear Magnetic Resonance, Gordon and Breach (1973).
4. WINTER J., Magnetic Resonance in Metals, OUP (1971).
5. ANDREW E.R., Nuclear Magnetic Resonance, Cambridge (1953).
6. COHEN M.H. and REIF F., Sol. State Phys. 5 321 (1957).
7. STERNHEIMER R.M., Phys. Rev. 84 244 (1951).
8. KNIGHT W.D., Phys. Rev. 76 1259 (1949).
9. KNIGHT W.D., Sol. State Phys. 2 93 (1956).
10. CLOGSTON A.M., JACCARINO V. and YAFET Y., Phys. Rev. A 134 650 (1964).
11. CLOGSTON A.M. and JACCARINO V., Phys. Rev. 121 1357 (1961).
12. CLOGSTON A.M., GOSSARD A.C., JACCARINO V. and YAFET Y., Phys. Rev. Lett. 9 262 (1962).
13. YAFET Y. and JACCARINO V., Phys. Rev. 133 A1630 (1964).
14. OBATA Y., J. Phys. Soc. Japan 18 1020 (1963).
15. KORRINGA J., Physica 16 601 (1950).
16. PINES D., Sol. State Phys. 1 367 (1955).
17. MORIYA T., J. Phys. Soc. Japan 18 516 (1963).
18. NARATH A. and WEAVER H.T., Phys. Rev. 175 373 (1968).
19. MITCHELL A.H., J. Chem. Phys. 26 1714 (1957).
20. OBATA Y., J. Phys. Soc. Japan 19 2348 (1964).
21. WARREN W.W., Phys. Rev. B 3 3708 (1971).
22. RUDERMAN M.A. and KITTEL C., Phys. Rev. 96 99 (1953).
23. SOLOMON I., Phys. Rev. 110 61 (1958).
24. MOTT N.F., Metal Insulator Transitions, Taylor and Francis (1974).

25. MOTT N.F., Proc. Phys. Soc. A 62 416 (1949).
26. WILSON A.H., Proc. Roy. Soc. 133 458 (1931).
27. MOTT N.F., Phil. Mag. 6 287 (1961).
28. ALEXANDER M.N. and HOLCOMB D.F., Rev. Mod. Phys. 40 815 (1968).
29. HUBBARD J., Proc. Roy. Soc. A 277 237 (1964).
30. HUBBARD J., Proc. Roy. Soc. A 277 401 (1964).
31. HERRING C., Magnetism, 4 ed. Rado and Suhl, Academic Press (1966).
32. LUTTINGER J.M., Phys. Rev. 119 1153 (1960).
33. CYROT M., J. de Phys. 33 125 (1972).
34. CYROT M., Phil. Mag. 25 1031 (1972).
35. CARON L.G. and KEMENY G., Phys. Rev. B 4 150 (1971).
36. MOTT N.F. and DAVIS E.A., Electronic processes in non-crystalline Materials, OUP (1971).
37. BRINKMAN W.F. and RICE T.M., Phys. Rev. B 2 4302 (1970).
38. GOODENOUGH J.B., Phys. Rev. B 5 2764 (1972).
39. MOTT N.F., Phil. Mag. 20 1 (1969).
40. SASAKI W., IKEHATA S. and KOBAYASHI S., J. Phys. Soc. Japan 36 1377 (1974).
41. BROWN G.C. and HOLCOMB D.F., Phys. Rev. B 10 3394 (1974).
42. ANDERSON P.W., Phys. Rev. 109 1492 (1958).
43. EDWARDS J.J. and THOULESS D.J., J. Phys. C 5 807 (1972).
44. KIKUCHI M., J. Phys. Soc. Japan 33 304 (1972).
45. MOTT N.F., Electronic and Structural properties of amorphous semiconductors, ed. Le Comber and Mort, Academic Press (1973).
46. MOTT N.F., Phil. Mag. 13 989 (1966).
47. MOTT N.F., Phil. Mag. 22 7 (1970).
48. MOTT N.F., Phil. Mag. 26 1015 (1972).
49. MOTT N.F., Phil. Mag. 19 835 (1969).

50. FRIEDMAN L., J. Non Cryst. Sol. 6 329 (1971).
51. MILLER A. and ABRAHAMS E., Phys. Rev. 120 745 (1960).
52. COHEN M.H. and JORTNER J., Phys. Rev. Lett. 30 699 (1973).
53. ALLEN F.R. and ADKINS C.J., Phil. Mag. 26 1027 (1972).
54. WEBMAN I., JORTNER J. and COHEN M.H., Phys. Rev. B 13 713
(1976).
55. TUNSTALL D.P., Phys. Rev. B 14 4735 (1976).
56. BRIDGMAN P.W., The Physics of High Pressure, Bell, London
(1949).
57. BENEDEK G.B. and PURCELL E.M., J. Chem. Phys. 22 2003 (1954).
58. BENEDEK G.B. and KUSHIDA T., J. Phys. Chem. Sol. 5 241 (1958).
59. BENEDEK G.B., Magnetic Resonance at High Pressures, Wiley
(1963).
60. SWENSON C.A., Sol. State Phys. 11 41 (1960).
61. BRADLEY R.S., High Pressure Physics and Chemistry, Academic
Press (1963).
62. VAN ITTERBEEK A., Physics of High Pressures and the condensed
phase, North-Holland (1965).
63. DRICKAMER H.G. and FRANK C.W., Electronic Transitions and the
High pressure Physics of solids, Chapman and Hall (1973).
64. PITT G.D., Contemp. Phys. 18 137 (1977).
65. KUSHIDA T., BENEDEK G. and BLOEMBERGEN N., Phys. Rev. 104 1364
(1956).
66. ITSKEVITCH E.S., Cryogenics 4 365 (1964).
67. DUGDALE J.S. and HULBERT J.A., Can. J. Phys. 35 720 (1957).
68. LAZAREW B. and KAN L.S., J. Phys. (USSR) 8 193 (1944).
69. LITSTER J.D. and BENEDEK G., J. Appl. Phys. 34 688 (1963).
70. HINRICHS C.H. and SWENSON C.A., Phys. Rev. 123 1106 (1961).
71. DUGDALE J.S., Nuovo Cim. Suppl. 9 27 (1958).
72. SCHIRBER J.E., Cryogenics 10 418 (1970).

73. SCHIRBER J.E. and SWENSON C.A., Phys. Rev. 123 1115 (1961).
74. SCHIRBER J.E. and SWENSON C.A., Phys. Rev. 127 72 (1962).
75. SCHIRBER J.E., Phys. Rev. 140 A2065 (1965).
76. O'SULLIVAN W.J. and SCHIRBER J.E., Phys. Rev. 151 484 (1966).
77. GAIDUKOV Y.P. and ITSKEVITCH E.S., Sov. Phys. JETP 18 51 (1964).
78. DMITRENKO I.M., VERKIN B.I. and LAZAREV B.G., Sov. Phys. JETP 8
229 (1959).
79. REICH H.A., Phys. Rev. 129 630 (1963).
80. See for example "Harwood Products manual" Harwood inc., Walpole,
Mass., USA.
81. MICHELS A. and LENSSEN M., J. Sci. Instr. 11 345 (1934).
82. High Pressure Technology Association "High Pressure Safety Code"
(1974), Chairman J. LEES, STL Harlow.
83. DOWNS J.L. and PAYNE R.T., Rev. Sci. Instr. 40 1278 (1969).
84. MILLS R.L. and GRILLY E.R., Phys. Rev. 99 480 (1955).
85. RIBNICK A.S., POST B. and BANKS E., Adv. in Chem. 39 246 (1962).
86. LIGHTSEY P.A., PhD Thesis, Cornell USA (1972).
87. STRAUMANIS M.E., J. Am. Chem. Soc. 71 679 (1949).
88. MEGAW H., Crystal Structures: A working approach, W.B. Saunders,
London (1973).
89. GLAZER A.M., Acta Cryst. A 31 756 (1975).
90. LYTTLE F.W., J. Appl. Phys. 35 2212 (1964).
91. WISEMAN P.J. and DICKENS P.G., J. Sol. State Chem. 6 374 (1973).
92. ATOJI M. and RUNDLE R.E., J. Chem. Phys. 32 627 (1960).
93. INGOLD J.H. and DeVRIES R.C., Acta Met. 6 736 (1958).
94. BONERA G., BORSA F., CRIPPA M.L. and RIGAMONTI A., Phys. Rev. B
4 52 (1971).
95. TUNSTALL D.P., Phys. Rev. B 11 2821 (1975).
96. KELLER J.M., J. Chem. Phys. 33 232 (1960).
97. MACKINTOSH A.R., J. Chem. Phys. 38 1991 (1963).

98. SIENKO M.J., J. Am. Chem. Soc. 81 5556 (1959).
99. GOODENOUGH J.B., J. Appl. Phys. Supp. 37 1415 (1966).
100. FUCHS R., J. Chem. Phys. 42 3781 (1965).
101. MATTHEISS L.F., Phys. Rev. B 2 3918 (1970).
102. MATTHEISS L.F., Phys. Rev. B 6 4718 (1972).
103. KOPP L., HARMON B.N. and LIU S.H., Sol. State Comm. 22 677 (1977).
104. CAMPAGNA M., WERTHEIM G.K., SHANKS H.R., ZUMSTEG F. and BANKS E., Phys. Rev. Lett. 34 738 (1975).
105. WOLFRAM T., Phys. Rev. Lett. 29 1383 (1972).
106. KAMATAKAHARI W.A., HARMON B.N., TAYLOR I.G., KOPP L., SHANKS H.R. and RATH J., Phys. Rev. Lett. 36 1393 (1976).
107. BROWN B.W. and BANKS E., Phys. Rev. 84 609 (1951).
108. GARDNER W.R. and DANIELSON G.C., Phys. Rev. 93 46 (1954).
109. ELLERBECK L.D., SHANKS H.R., SIDLES P.H. and DANIELSON G.C., J. Chem. Phys. 35 298 (1961).
110. MUHLESTEIN L.D. and DANIELSON G.C., Phys. Rev. 158 825 (1967).
111. McNEILL W. and CONROY L.E., J. Chem. Phys. 36 87 (1962).
112. LIGHTSEY P.A., LILIENTELD D.A. and HOLCOMB D.F., Phys. Rev. B 14 4730 (1976).
113. VEST R.W., GRIFFEL M. and SMITH J.F., J. Chem. Phys. 28 293 (1958).
114. ZUMSTEG F.C., Phys. Rev. B 14 1406 (1976).
115. GREINER J.D., SHANKS H.R. and WALLACE D.C., J. Chem. Phys. 36 772 (1962).
116. ROSEN C., POST B. and BANKS E., Acta Cryst. 9 477 (1956).
117. SHANKS H.R. and REDIN R.D., J. Phys. Chem. Sol. 27 75 (1965).
118. WHITEMAN A.E., MARTIN J.J. and SHANKS H.R., J. Phys. Chem. Sol. 32 2223 (1971).
119. BROWN B.W. and BANKS E., J. Am. Chem. Soc. 76 963 (1954).

120. CONSADORI F. and STELLA A., Lett. Nuovo Cim. 3 600 (1970).
121. CAMAGNI P., MANARA A., CAMPAGNOLI G. and GUSTINETTI A., Phys. Rev. B 15 4623 (1977).
122. JONES W.H., GARBATY E.A. and BARNES R.G., J. Chem. Phys. 36 494 (1962).
123. NARATH A. and WALLACE D.C., Phys. Rev. 127 724 (1962).
124. FROMHOLD A.T. and NARATH A., Phys. Rev. 136 A 487 (1964).
125. FROMHOLD A.T. and NARATH A., Phys. Rev. 152 585 (1966).
126. WOLF F., KLINE D. and STORY H.S., J. Chem. Phys. 53 3538 (1970).
127. BORSA F., Proc. Int. School of Physics, Enrico Fermi course LIX (North Holland) 137 (1976).
128. WEINBERGER B.R., PhD Thesis, Cornell USA (1977).
129. SUNDFORS R.K. and HOLCOMB D.F., Phys. Rev. 136 810 (1964).
130. MOLLET H.F. and GERSTEIN B.C., J. Chem. Phys. 60 1440 (1974).
131. CRANDALL R.S. and FAUGHNAN B.W., Phys. Rev. Lett. 39 232 (1977).
132. DICKENS P.G. and HURDITCH R.J., Chemistry of extended defects in non-metallic solids p.555 North-Holland (1970).
133. NISHIMURA K., Sol. State Comm. 20 523 (1976).
134. DEB S.K., Phil. Mag. 27 801 (1973).
135. HERSH H.N., KRAMER W.E. and MAGEE J.H., Appl. Phys. Lett. 27 646 (1975).
136. FEINLEIB J., SCOULER W.J. and FERRETTI A., Phys. Rev. 165 765 (1968).
137. NARATH A. and BARHAM D.C., Phys. Rev. 176 479 (1968).
138. ANGELINI G., BONERA G. and RIGAMONTI A., Proc. 17th Ampere Cong. p.346 North-Holland (1973).
139. MOTT N.F., Phil. Mag. 35 111 (1977).
140. DOUMERC J., PhD Thesis, Bordeaux (1974).
141. SHANKS H.R., J. Cryst. Growth 13/14 433 (1972).
142. CLARK W.G., Rev. Sci. Instr. 35 316 (1964).

143. BROWN D., PhD Thesis, St Andrews (1970).
144. LOWE I.J. and TARR C.E., J. Phys. E 1 320 (1968).
145. HOULT D.I. and RICHARDS R.E., Proc. Roy. Soc. A 344 311 (1975).
146. HOULT D.I. and RICHARDS R.E., J. Mag. Res. 24 71 (1976).
147. DESHMUKH V.G.I., PhD Thesis, St Andrews (1977).
148. FARRAR T.C. and BECKER E.D., Pulse and Fourier Transform NMR,
Academic Press (1971).
149. ERNST R.R. and ANDERSON W.A., Rev. Sci. Instr. 37 93 (1966).
150. GILLIES D.G. and SHAW D., Ann. Rep. on NMR Spect. 5A 560 (1972).
151. COOLEY J.W. and TUKEY J.W., Math. Comput. 19 297 (1965).
152. RYTER C., Phys. Lett. 4 69 (1963).
153. GERSTEIN B.C., KLEIN A.H. and SHANKS H.R., J. Phys. Chem. Sol.
25 177 (1964).
154. CRANDALL R.S. and FAUGHNAN B.W., Phys. Rev. B 16 1750 (1977).
155. WHITTINGHAM PhD Thesis, University of Oxford (1974).
156. SMITH J.F., Phys. Rev. 95 1369 (1954).
157. SCHIRBER J.E., Phys. Rev. B 5 752 (1972).
158. KOPFERMANN H., Nuclear Moments - English version prepared by
E.E. Schneider, Academic Press (1958).
159. YAFET Y., KEYES R.W. and ADAMS E.N., J. Phys. Chem. Sol. 1 137
(1956).